UNIVERSITY OF CALIFORNIA, SAN DIEGO

Precision measurements of cosmic microwave background polarization to study cosmic inflation and large scale structure

A dissertation submitted in partial satisfaction of the
requirements for the degree
Doctor of Philosophy

in

Physics

by

Darcy Riley Barron

Committee in charge:

Professor Brian Keating, Chair
Professor Adam Burgasser
Professor Hans Paar
Professor Gabriel Rebeiz
Professor Mark Thiemens

2015

The dissertation of Darcy Riley Barron is approved, and it is acceptable in quality and form for publication on microfilm and electronically:

_____

_____

_____

_____

_____
Chair

University of California, San Diego

2015

EPIGRAPH

"There is a theory which states that if ever anyone discovers exactly what the Universe is for and why it is here, it will instantly disappear and be replaced by something even more bizarre and inexplicable. There is another theory which states that this has already happened."

—Douglas Adams

TABLE OF CONTENTS

LIST OF FIGURES

LIST OF TABLES

ACKNOWLEDGEMENTS

Thanks to my advisor Brian Keating, for providing me with so many great opportunities, and for all the guidance (and funding!) throughout the different stages of my degree.

My graduate career got started off right when I met some great people on visiting weekend who would become my classmates and friends. Thanks to Agnieszka, Alex, Jacob, Mike, Evan, Matt, Nathan, Jordan, and many others for making my time at UCSD so enjoyable, and full of tea times, BASH's, movie nights, climbing, biking, and assorted adventures.

The POLARBEAR project, described in Chapter 3, is the product of a large and growing collaboration of people. Thanks to Kam Arnold for all the hard work managing everyone in this collaboration over the past few years, including me. Thanks to our Chilean crew, Nolberto and Jose, who try their best to keep everything running smoothly.

OFFICIAL ACKNOWLEDGEMENTS

Section 2.4 is a reprint of material as it appears in: D. Barron, M. Atlas, B. Keating, R. Quillin, N. Stebor, B. Wilson, Performance of a 4 Kelvin pulse-tube cooled cryostat with dc SQUID amplifiers for bolometric detector testing, published in the 17th International Cryocooler Conference Proceedings, 2012. The dissertation author was the primary author of this paper.

Section 3.2 is a reprint of material as it appears in: D. Barron, P. Ade, A. Anthony, K. Arnold, D. Boettger, J. Borrill, S. Chapman, Y. Chinone, M. Dobbs, J. Edwards, J. Errard, G. Fabbian, D. Flanigan, G. Fuller, A. Ghribi, W. Grainger, N. Halverson, M. Hasegawa, K. Hattori, M. Hazumi, W. Holzapfel, J. Howard, P. Hyland, G. Jaehnig, A. Jaffe, B. Keating, Z. Kermish, R. Keskitalo, T. Kisner, A. T. Lee, M. Le Jeune, E. Linder, M. Lungu, F. Matsuda, T. Matsumura, X. Meng, N. J. Miller, H. Morii, S. Moyerman, M. Meyers, H. Nishino, H. Paar, J. Peloton, E. Quealy, G. Rebeiz, C. L. Reichart, P. L. Richards, C. Ross, A. Shimizu, C. Shimmin, M. Shimon, M. Sholl, P. Siritanasak, H. Spieler, N. Stebor, B. Steinbach, R. Stompor, A. Suzuki, T. Tomaru, C. Tucker, A. Yadav, O. Zahn, The

POLARBEAR Cosmic Microwave Background Polarization Experiment, published in J. Low Temp. Phys. Vol. 176, 5-6, pp 726-732, 2014. The dissertation author was the primary author of this paper.

Figure 3.8 and Figure 3.9 are reprints of material as it appears in: The POLARBEAR Collaboration: P. A. R. Ade, Y. Akiba, A. E. Anthony, K. Arnold, M. Atlas, D. Barron, D. Boettger, J. Borrill, S. Chapman, Y. Chinone, M. Dobbs, T. Elleflot, J. Errard, G. Fabbian, C. Feng, D. Flanigan, A. Gilbert, W. Grainger, N. W. Halverson, M. Hasegawa, K. Hattori, M. Hazumi, W. L. Holzapfel, Y. Hori, J. Howard, P. Hyland, Y. Inoue, G. C. Jaehnig, A. H. Jaffe, B. Keating, Z. Kermish, R. Keskitalo, T. Kisner, M. Le Jeune, A. T. Lee, E. M. Leitch, E. Linder, M. Lungu, F. Matsuda, T. Matsumura, X. Meng, N. J. Miller, H. Morii, S. Moyerman, M. J. Myers, M. Navaroli, H. Nishino, H. Paar, J. Peloton, D. Poletti, E. Quealy, G. Rebeiz, C. L. Reichardt, P. L. Richards, C. Ross, I. Schanning, D. E. Schenck, B. D. Sherwin, A. Shimizu, C. Shimmin, M. Shimon, P. Siritanasak, G. Smecher, H. Spieler, N. Stebor, B. Steinbach, R. Stompor, A. Suzuki, S. Takakura, T. Tomaru, B. Wilson, A. Yadav, and O. Zahn, A Measurement of the Cosmic Microwave Background B-mode Polarization Power Spectrum at Sub-degree Scales with POLARBEAR, published in ApJ, 794, 171 , 2014. The dissertation author made essential contributions to many aspects of this work.

Section 3.4 is an expanded reprint of the material as it appears in: D. Barron, P. A. R. Ade, Y. Akiba, C. Aleman, K. Arnold, M. Atlas, A. Bender, J. Borrill, S. Chapman, Y. Chinone, A. Cukierman, M. Dobbs, T. Elleflot, J. Errard, G. Fabbian, G. Feng, A. Gilbert, N. W. Halverson, M. Hasegawa, K. Hattori, M. Hazumi, W. L. Holzapfel, Y. Hori, Y. Inoue, G. C. Jaehnig, N. Katayama, B. Keating, Z. Kermish, R. Keskitalo, T. Kisner, M. Le Jeune, A. T. Lee, F. Matsuda, T. Matsumura, H. Morii, M. J. Myers, M. Navroli, H. Nishino, T. Okamura, J. Peloton, G. Rebeiz, C. L. Reichardt, P. L. Richards, C. Ross, M. Sholl, P. Siritanasak, G. Smecher, N. Stebor, B. Steinbach, R. Stompor, A. Suzuki, J. Suzuki, S. Takada, T. Takakura, T. Tomaru, B. Wilson, H. Yamaguchi, O. Zahn, Development and characterization of the readout system for POLARBEAR-2, published in the Proceedings of SPIE 9153: Millimeter, Submillimeter, and Far-Infrared Detectors and

Instrumentation for Astronomy VII, 915335, 2014. The dissertation author was the primary author of this paper.

Figure 4.1 was provided by Yuji Chinone.

VITA

2008	B. S. in Physics with Honors, University of Illinois, Urbana-Champaign
2010	M. S. in Physics, University of California, San Diego
2015	Ph. D. in Physics, University of California, San Diego

PUBLICATIONS

The POLARBEAR Collaboration: P.A.R. Ade, Y. Akiba, A.E. Anthony, K. Arnold, M. Atlas, D. Barron, D. Boettger, J. Borrill, S. Chapman, Y. Chinone, M. Dobbs, T. Elleflot, J. Errard, G. Fabbian, C. Feng, D. Flanigan, A. Gilbert, W. Grainger, N.W. Halverson, M. Hasegawa, K. Hattori, M. Hazumi, W.L. Holzapfel, Y. Hori, J. Howard, P. Hyland, Y. Inoue, G.C. Jaehnig, A.H. Jaffe, B. Keating, Z. Kermish, R. Keskitalo, T. Kisner, M. Le Jeune, A.T. Lee, E.M. Leitch, E. Linder, M. Lungu, F. Matsuda, T. Matsumura, X. Meng, N.J. Miller, H. Morii, S. Moyerman, M.J. Myers, M. Navaroli, H. Nishino, H. Paar, J. Peloton, D. Poletti, E. Quealy, G. Rebeiz, C.L. Reichardt, P.L. Richards, C. Ross, I. Schanning, D.E. Schenck, B. Sherwin, A. Shimizu, C. Shimmin, M. Shimon, P. Siritanasak, G. Smecher, H. Spieler, N. Stebor, B. Steinbach, R. Stompor, A. Suzuki, S. Takakura, T. Tomaru, B. Wilson, A. Yadav, O. Zahn. A Measurement of the Cosmic Microwave Background B-mode Polarization Power Spectrum at Sub-degree Scales with POLARBEAR. ApJ, 794, 171, 2014. doi:10.1088/0004-637X/794/2/171

The POLARBEAR Collaboration: P.A.R. Ade, Y. Akiba, A.E. Anthony, K. Arnold, M. Atlas, D. Barron, D. Boettger, J. Borrill, S. Chapman, Y. Chinone, M. Dobbs, T. Elleflot, J. Errard, G. Fabbian, C. Feng, D. Flanigan, A. Gilbert, W. Grainger, N.W. Halverson, M. Hasegawa, K. Hattori, M. Hazumi, W.L. Holzapfel, Y. Hori, J. Howard, P. Hyland, Y. Inoue, G.C. Jaehnig, A.H. Jaffe, B. Keating, Z. Kermish, R. Keskitalo, T. Kisner, M. Le Jeune, A.T. Lee, E.M. Leitch, E. Linder, M. Lungu, F. Matsuda, T. Matsumura, X. Meng, N.J. Miller, H. Morii, S. Moyerman, M.J. Myers, M. Navaroli, H. Nishino, H. Paar, J. Peloton, D. Poletti, E. Quealy, G. Rebeiz, C.L. Reichardt, P.L. Richards, C. Ross, I. Schanning, D.E. Schenck, B. Sherwin, A. Shimizu, C. Shimmin, M. Shimon, P. Siritanasak, G. Smecher, H. Spieler, N. Stebor, B. Steinbach, R. Stompor, A. Suzuki, S. Takakura, T. Tomaru, B. Wilson, A. Yadav, O. Zahn. Measurement of the Cosmic Microwave Background Polarization Lensing Power Spectrum with the POLARBEAR Experiment. Phys. Rev. Lett. 113, 021301, 2014. doi:10.1103/PhysRevLett.113.021301

The POLARBEAR Collaboration: P.A.R. Ade, Y. Akiba, A.E. Anthony, K. Arnold, M. Atlas, D. Barron, D. Boettger, J. Borrill, S. Chapman, Y. Chinone, M. Dobbs,

T. Elleflot, J. Errard, G. Fabbian, C. Feng, D. Flanigan, A. Gilbert, W. Grainger, N.W. Halverson, M. Hasegawa, K. Hattori, M. Hazumi, W.L. Holzapfel, Y. Hori, J. Howard, P. Hyland, Y. Inoue, G.C. Jaehnig, A.H. Jaffe, B. Keating, Z. Kermish, R. Keskitalo, T. Kisner, M. Le Jeune, A.T. Lee, E.M. Leitch, E. Linder, M. Lungu, F. Matsuda, T. Matsumura, X. Meng, N.J. Miller, H. Morii, S. Moyerman, M.J. Myers, M. Navaroli, H. Nishino, H. Paar, J. Peloton, D. Poletti, E. Quealy, G. Rebeiz, C.L. Reichardt, P.L. Richards, C. Ross, I. Schanning, D.E. Schenck, B. Sherwin, A. Shimizu, C. Shimmin, M. Shimon, P. Siritanasak, G. Smecher, H. Spieler, N. Stebor, B. Steinbach, R. Stompor, A. Suzuki, S. Takakura, T. Tomaru, B. Wilson, A. Yadav, O. Zahn. Evidence for Gravitational Lensing of the Cosmic Microwave Background Polarization from Cross-Correlation with the Cosmic Infrared Background. Phys. Rev. Lett. 112, 131302, 2014. doi:10.1103/PhysRevLett.112.131302

D. Barron, P. A. R. Ade, Y. Akiba, C. Aleman, K. Arnold, M. Atlas, A. Bender, J. Borrill, S. Chapman, Y. Chinone, A. Cukierman, M. Dobbs, T. Elleflot, J. Errard, G. Fabbian, G. Feng, A. Gilbert, N. W. Halverson, M. Hasegawa, K. Hattori, M. Hazumi, W. L. Holzapfel, Y. Hori, Y. Inoue, G. C. Jaehnig, N. Katayama, B. Keating, Z. Kermish, R. Keskitalo, T. Kisner, M. Le Jeune, A. T. Lee, F. Matsuda, T. Matsumura, H. Morii, M. J. Myers, M. Navroli, H. Nishino, T. Okamura, J. Peloton, G. Rebeiz, C. L. Reichardt, P. L. Richards, C. Ross, M. Sholl, P. Siritanasak, G. Smecher, N. Stebor, B. Steinbach, R. Stompor, A. Suzuki, J. Suzuki, S. Takada, T. Takakura, T. Tomaru, B. Wilson, H. Yamaguchi, O. Zahn, Development and characterization of the readout system for POLARBEAR-2. Proc. SPIE 9153, Millimeter, Submillimeter, and Far-Infrared Detectors and Instrumentation for Astronomy VII, 915335, 2014. doi:10.1117/12.2055611

K. Arnold, N. Stebor, P. A. R. Ade, Y. Akiba, A. E. Anthony, M. Atlas, D. Barron, A. Bender, D. Boettger, J. Borrill, S. Chapman, Y. Chinone, A. Cukierman, M. Dobbs, T. Elleflot, J. Errard, G. Fabbian, C. Feng, A. Gilbert, N. Goeckner-Wald, N. W. Halverson, M. Hasegawa, K. Hattori, M. Hazumi, W. L. Holzapfel, Y. Hori, Y. Inoue, G. C. Jaehnig, A. H. Jaffe, N. Katayama, B. Keating, Z. Kermish, R. Keskitalo, T. Kisner, M. Le Jeune, A. T. Lee, E. M. Leitch, E. Linder, F. Matsuda, T. Matsumura, X. Meng, N. J. Miller, H. Morii, M. J. Myers, M. Navaroli, H. Nishino, T. Okamura, H. Paar, J. Peloton, D. Poletti, C. Raum, G. Rebeiz, C. L. Reichardt, P. L. Richards, C. Ross, K. M. Rotermund, D. E. Schenck, B. D. Sherwin, I. Shirley, M. Sholl, P. Siritanasak, G. Smecher, B. Steinbach, R. Stompor, A. Suzuki, J. Suzuki, S. Takada, S. Takakura, T. Tomaru, B. Wilson, A. Yadav, O. Zahn. The Simons Array: expanding POLARBEAR to three multi-chroic telescopes. Proc. SPIE 9153, Millimeter, Submillimeter, and Far-Infrared Detectors and Instrumentation for Astronomy VII, 91531F, 2014. doi: 10.1117/12.2057332

K. Hattori, Y. Akiba, K. Arnold, D. Barron, A. Bender, M. A. Dobbs, T. de Haan, N. Harrington, M. Hasegawa, M. Hazumi, W. L. Holzapfel, Y. Hori, B.

Keating, A. T. Lee, J. Montgomery, H. Morii, M. Myers, K. Rotermund, I. Shirley, G. Smecher, N. Stebor, A. Suzuki, T. Tomaru. Optimization of cold resonant filters for frequency domain multiplexed readout of POLARBEAR-2. Proc. SPIE 9153, Millimeter, Submillimeter, and Far-Infrared Detectors and Instrumentation for Astronomy VII, 91531B (August 19, 2014). doi:10.1117/12.2057045

Y. Inoue, N. Stebor, P. A. R. Ade, Y. Akiba, K. Arnold, A. E. Anthony, M. Atlas, D. Barron, A. Bender, D. Boettger, J. Borrilll, S. Chapman, Y. Chinone, A. Cukierman, M. Dobbs, T. Elleflot, J. Errard, G. Fabbian, C. Feng, A. Gilbert, N. W. Halverson, M. Hasegawa, K. Hattori, M. Hazumi, W. L. Holzapfel, Y. Hori, G. C. Jaehnig, A. H. Jaffe, N. Katayama, B. Keating, Z. Kermish, Reijo Keskitalo, T. Kisner, M. Le Jeune, A. T. Lee, E. M. Leitch, E. Linder, F. Matsuda, T. Matsumura, X. Meng, H. Morii, M. J. Myers, M. Navaroli, H. Nishino, T. Okamura, H. Paar, J. Peloton, D. Poletti, G. Rebeiz, C. L. Reichardt, P. L. Richards, C. Ross, D. E. Schenck, B. D. Sherwin, P. Siritanasak, G. Smecher, M. Sholl, B. Steinbach, R. Stompor, A. Suzuki, J. Suzuki, S. Takada, S. Takakura, T. Tomaru, B. Wilson, A. Yadav, H. Yamaguchi, O. Zahn. Thermal and optical characterization for POLARBEAR-2 optical system. Proc. SPIE 9153, Millimeter, Submillimeter, and Far-Infrared Detectors and Instrumentation for Astronomy VII, 91533A (August 19, 2014). doi:10.1117/12.2055572

D. Barron, P. Ade, A. Anthony, K. Arnold, D. Boettger, J. Borrill, S. Chapman, Y. Chinone, M. Dobbs, J. Edwards, J. Errard, G. Fabbian, D. Flanigan, G. Fuller, A. Ghribi, W. Grainger, N. Halverson, M. Hasegawa, K. Hattori, M. Hazumi, W. Holzapfel, J. Howard, P. Hyland, G. Jaehnig, A. Jaffe, B. Keating, Z. Kermish, R. Keskitalo, T. Kisner, A. T. Lee, M. Le Jeune, E. Linder, M. Lungu, F. Matsuda, T. Matsumura, X. Meng, N. J. Miller, H. Morii, S. Moyerman, M. Meyers, H. Nishino, H. Paar, J. Peloton, E. Quealy, G. Rebeiz, C. L. Reichart, P. L. Richards, C. Ross, A. Shimizu, C. Shimmin, M. Shimon, M. Sholl, P. Siritanasak, H. Spieler, N. Stebor, B. Steinbach, R. Stompor, A. Suzuki, T. Tomaru, C. Tucker, A. Yadav, O. Zahn. The POLARBEAR Cosmic Microwave Background Polarization Experiment. J. Low Temp. Phys. Vol. 176, 5-6, pp 726-732, 2014. doi:10.1007/s10909-013-1065-5

A. Suzuki, P. Ade, Y. Akiba, C. Aleman, K. Arnold, M. Atlas, D. Barron, J. Borrill, S. Chapman, Y. Chinone, A. Cukierman, M. Dobbs, T. Elleflot, J. Errard, G. Fabbian, G. Feng, A. Gilbert, W. Grainger, N. Halverson, M. Hasegawa, K. Hattori, M. Hazumi, W. Holzapfel, Y. Hori, Y. Inoue, G. Jaehnig, N. Katayama, B. Keating, Z. Kermish, R. Keskitalo, T. Kisner, A. Lee, F. Matsuda, T. Matsumura, H. Morii, S. Moyerman, M. Myers, M. Navaroli, H. Nishino, T. Okamura, C. Reichart, P. Richards, C. Ross, K. Rotermund, M. Sholl, P. Siritanasak, G. Smecher, N. Stebor, R. Stompor, J. Suzuki, S. Takada, S. Takakura, T. Tomaru, B. Wilson, H. Yamaguchi, O. Zahn. The POLARBEAR-2 experiment. J. Low Temperature Physics, 2014. doi:10.1007/s10909-014-1112-x

H. Nishino, P. Ade, Y. Akiba, A. Anthony, K. Arnold, D. Barron, D. Boettger, J. Borrill, S. Chapmann, Y. Chinone, M. A. Dobbs, J. Errard, G. Fabbian, C. Feng, D. Flanigan, G. Fuller, A. Ghribi, W. Grainger, N. Halverson, M. Hasegawa, K. Hattori, M. Hazumi, W. L. Holzapfel, J. Howard, P. Hyland, Y. Inoue, A. Jaffe, G. Jaehnig, Y. Kaneko, N. Katayama, B. Keating, Z. Kermish, N. Kimura, T. Kisner, A. T. Lee, M. Le Jeune, E. Linder, M. Lungu, F. Matsuda, T. Matsumura, N. J. Miller, H. Morii, S. Moyerman, M. J. Myers, R. O'Brient, T. Okamura, H. Paar, J. Peloton, E. Quealy, C. L. Reichardt, P. L. Richards, C. Ross, A. Shimizu, M. Shimon, C. Shimmin, M. Sholl, P. Siritanasak, H. Spieler, N. Stebor, B. Steinbach, R. Stompor, A. Suzuki, J. Suzuki, K. Tanaka, T. Tomaru, C. Tucker, A. Yadav, O. Zahn. POLARBEAR CMB Polarization experiment. Proceedings of the 12th Asia Pacific Physics Conference, 2014. doi:10.7566/JPSCP.1.013107

T. Matsumura, P. Ade, Y. Akiba, C. Aleman, K. Arnold, M. Atlas, D. Barron, J. Borrill, S. Chapman, Y. Chinone, A. Cukierman, M. Dobbs, T. Elleflot, J. Errard, G. Fabbian, G. Feng, A. Gilbert, W. Grainger, N. Halverson, M. Hasegawa, K. Hattori, M. Hazumi, W. Holzapfel, Y. Hori, Y. Inoue, G. Jaehnig, N. Katayama, B. Keating, Z. Kermish, R. Keskitalo, T. Kisner, A. Lee, F. Matsuda, H. Morii, S. Moyerman, M. Myers, M. Navaroli, H. Nishino, T. Okamura, C. Reichart, P. Richards, C. Ross, K. Rotermund, M. Sholl, P. Siritanasak, G. Smecher, N. Stebor, R. Stompor, J. Suzuki, A. Suzuki, S. Takada, S. Takakura, T. Tomaru, B. Wilson, H. Yamaguchi, O. Zahn. Cosmic microwave background B-mode polarization experiment POLARBEAR-2. Proceedings of the 12th Asia Pacific Physics Conference, 2014. doi:10.7566/JPSCP.1.013108

K. Hattori, K. Arnold, D. Barron, M. Dobbs, T. de Haan, N. Harrington, M. Hasegawa, M. Hazumi, W.L. Holzapfel, B. Keating, A.T. Lee, H. Morii, M.J. Myers, G. Smecher, A. Suzuki, T. Tomaru. Adaption of frequency-domain readout for transition edge sensor bolometers for the POLARBEAR-2 cosmic microwave background experiment. Nuclear Instruments and Methods in Physics Research Section A: Accelerators, Spectrometers, Detectors and Associated Equipment, 2013. doi:10.1016/j.nima.2013.07.052

K. Arnold, P.A.R. Ade, A.E. Anthony, D. Barron, D. Boettger, J. Borill, S. Chapman, Y. Chinone, M.A. Dobbs, J. Errard, G. Fabbian, D. Flanigan, G. Fuller, A. Ghribi, W. Granger, N. Halverson, M. Hasegawa, K. Hattori, W.L. Holzapfel, J. Howard, P. Hyland, A. Jaffe, B. Keating, Z. Kermish, T. Kisner, M. Le Jeune, A.T. Lee, E. Linder, M. Lungu, F. Matsuda, T. Matsumura, N.J. Miller, X. Meng, H. Morii, S. Moyerman, M.J. Myers, H. Nishino, H. Paar, E. Quealy, P.L. Richards, C. Reichardt, C. Ross, A. Shimizu, C. Shimmin, M. Shimon, M. Sholl, P. Siritanasak, H. Spieler, N. Stebor, B. Steinbach, R. Stompor, A. Suzuki, T. Tomaru, C. Tucker, and O. Zahn. The bolometric focal plane array of the POLARBEAR CMB experiment. Proceedings of the Society of Photo-optical Instrumentation Engineers (SPIE), 8452 (49), 2012. doi:10.1117/12.927057

Z. Kermish, P.A.R. Ade, K. Arnold, A.E. Anthony, D. Barron, D. Boettger, J. Borill, S. Chapman, Y. Chinone, M.A. Dobbs, J. Errard, G. Fabbian, D. Flanigan, G. Fuller, A. Ghribi, W. Granger, N. Halverson, M. Hasegawa, K. Hattori, W.L. Holzapfel, J. Howard, P. Hyland, A. Jaffe, B. Keating, T. Kisner, M. Le Jeune, A.T. Lee, E. Linder, M. Lungu, F. Matsuda, T. Matsumura, N.J. Miller, X. Meng, H. Morii, S. Moyerman, M.J. Myers, H. Nishino, H. Paar, E. Quealy, P.L. Richards, C. Reichardt, C. Ross, A. Shimizu, C. Shimmin, M. Shimon, M. Sholl, P. Siritanasak, H. Spieler, N. Stebor, B. Steinbach, R. Stompor, A. Suzuki, T. Tomaru, C. Tucker, and O. Zahn. The POLARBEAR experiment. Proceedings of the Society of Photo-optical Instrumentation Engineers (SPIE), 8452 (48), 2012. doi:10.1117/12.926354

T. Tomaru, M. Hasumi, A.T. Lee, P.A.R. Ade, K. Arnold, D. Barron, J. Borrill, S. Chapman, Y. Chinone, M.A. Dobbs, J. Errard, G. Fabbian, A. Ghribi. W. Grainger, N. Halverson, M. Hasegawa, K. Hattori, W.L. Holzapfel, Y. Iuoue, S. Ishii, Y. Kaneko, B. Keating, Z. Kermish, N. Kimura, T. Kisner, W. Kranz, F. Matsuda, T. Matsumura, H. Morii, M.J. Myers, H. Nishino, T. Okamura, E. Quealy, C.L. Reichards, P.L.Richards, D. Rosen, C. Ross, A. Shimizu, M. Sholl, P. Siritanasak, P. Smith, N. Stebor, R. Stompor, A. Suzuki, J. Suzuki, S. Takada, K. Tanaka and O. Zahn. The POLARBEAR-2 experiment. Proceedings of the Society of Photo-optical Instrumentation Engineers (SPIE), 8452 (53), 2012. doi:10.1117/12.926158

T. Matsumura, P.A.R. Ade, K. Arnold, D. Barron, J. Borrill, S. Chapman, Y. Chinone, M.A. Dobbs, J. Errard, G. Fabbian, A. Ghribi. W. Grainger, N. Halverson, M. Hasegawa, M. Hasumi, K. Hattori, W.L. Holzapfel, Y. Iuoue, S. Ishii, Y. Kaneko, B. Keating, Z. Kermish, N. Kimura, T. Kisner, W. Kranz, A.T. Lee, F. Matsuda, T. Matsumura, H. Morii, M.J. Myers, H. Nishino, T. Okamura, E. Quealy, C.L. Reichards, P.L. Richards, D. Rosen, C. Ross, A. Shimizu, M. Sholl, P. Siritanasak, P. Smith, N. Stebor, R. Stompor, A. Suzuki, J. Suzuki, S. Takada, K. Tanaka and O. Zahn. et al. POLARBEAR-2 optical and polarimeter designs. Proceedings of the Society of Photo-optical Instrumentation Engineers (SPIE), 8452 (124), 2012. doi:10.1117/12.926770

D. Barron, M. Atlas, B. Keating, R. Quillin, N. Stebor, B. Wilson. Performance of a 4 Kelvin pulse-tube cooled cryostat with dc SQUID amplifiers for bolometric detector testing. 17th International Cryocooler Conference Proceedings, 2012. arxiv:1301.0860

T. Matsumura, P. Ade, D. Barkats, D. Barron, J. Battle, E. M. Bierman, J. Bock, H. C. Chiang, B. Crill, C. D. Dowell, L. Duband, E. F. Hivon, W. L. Holzapfel, V. V. Hristov, W. C. Jones, B. Keating, J. M. Kovac, C. Kuo, A. E. Lange, E. M. Leitch, P. Mason, H. T. Nguyen, N. Ponthieu, C. Pryke, S. Richter, G. M. Rocha, Y. D. Takahashi, K. W. Yoon. Absolute polarization angle calibration using polarized diffuse Galactic emission observed by BICEP. Proc. SPIE 7741,

Millimeter, Submillimeter, and Far-Infrared Detectors and Instrumentation for Astronomy V, 77412O (July 15, 2010). doi:10.1117/12.856855

E. M. Bierman, T. Matsumura, C. D. Dowell, B. G. Keating, P. Ade, D. Barkats, D. Barron, J. O. Battle, J. J. Bock, H. C. Chiang, T. L. Culverhouse, L. Duband, E. F. Hivon, W. L. Holzapfel, V. V. Hristov, J. P. Kaufman, J. M. Kovac, C. L Kuo, A. E. Lange, E. M. Leitch, P. V. Mason, N. J. Miller, H. T. Nguyen, C. Pryke, S. Richter, G. M. Rocha, C. Sheehy, Y. D. Takahashi, K. W. Yoon. A Millimeter-Wave Galactic Plane Survey with the BICEP Polarimeter. ApJ 741, 81, 2011. doi:10.1088/0004-637X/741/2/81

R. L. Ward, R. Adhikari, B. Abbot, R. Abbot, D. Barron, R. Bork, T. Fricke, V. Frolov, J. Heefner, A. Ivanov, O. Miyakawa, K. McKenzie, B. Slagmolen, M. Smith, R. Taylor, S. Vass, S. Waldman, A. Weinstein. dc Readout experiment at the Caltech 40m prototype interferometer. Class. Quantum Grav. 25, 114030, 2008. doi:10.1088/0264-9381/25/11/114030

ABSTRACT OF THE DISSERTATION

Precision measurements of cosmic microwave background polarization to study cosmic inflation and large scale structure

by

Darcy Riley Barron

Doctor of Philosophy in Physics

University of California, San Diego, 2015

Professor Brian Keating, Chair

Measurements of cosmic microwave background (CMB) are a powerful tool to study and understand our universe. Detailed characterizations of the temperature of the CMB played a key role in the development of the current standard cosmological model, ΛCDM. Although this model, along with the standard model of particle physics, describes much of the observed large-scale structure of the universe and its evolution, there are still gaps in our understanding. The next step for answering many of these outstanding questions in cosmology and particle physics lies in the characterization of the CMB B-mode polarization pattern. This faint signal is expected to be imprinted at the formation of the CMB by inflationary gravitational waves in the early universe. Detection of this primordial B-mode

signal would not only be the first direct evidence for inflation, but would also constrain inflationary models and determine the energy scale of inflation. Gravitational lensing of CMB E-mode polarization by intervening matter also produces a secondary B-mode polarization signal at smaller angular scales. This signal traces large scale structure in the universe, with information about the distribution and composition of matter.

This dissertation describes research in instrumentation, observations, and data analysis for measurements of the CMB B-mode signal, including work on three generations of experiments in this rapidly evolving field. Analysis of the galactic plane and CMB multi-frequency data from the BICEP1 CMB polarization telescope helped further our understanding of polarized CMB foregrounds by studying polarized galactic emission and the structure of the galactic magnetic field. The deployment and first season of observations with the POLARBEAR-1 instrument, a CMB polarization telescope, are described. This instrument reached a milestone in sensitivity with our measurement of a non-zero B-mode polarization power spectrum. Finally, this thesis discusses the design and development of the POLARBEAR-2 instrument, a new receiver with expanded capabilities and sensitivity, scheduled to deploy alongside POLARBEAR-1 in 2016.

Chapter 1

Introduction

An investigation of noise in a sensitive radio antenna for communications turned into a discovery that greatly expanded our understanding of the universe and its origins. The uniform excess signal seen by Penzias and Wilson was the cosmic microwave background (CMB), the relic radiation left over from the Big Bang [1]. From this initial discovery to the present, measurements of the CMB have continued to help refine our models of the universe. This chapter gives an overview of the CMB, its role in modern cosmology, and current measurement techniques and challenges. Section 1.1 gives an overview of the current standard cosmological model ΛCDM. Section 1.2 discusses the features of the CMB and standard mathematical methods to describe it. Section 1.3 gives a brief history of measurement techniques. Section 1.4 discusses foregrounds, which are potential sources of contamination for CMB measurements.

1.1 ΛCDM Cosmology

The standard model of big bang cosmology is our current best explanation for observations of our universe made over the past century, based on the framework of general relativity and the standard model of particle physics. The key observations that created the foundation for big bang cosmology are the expansion of the universe [2], the existence of the cosmic microwave background [3], and the relative abundance of light elements [4]. These observations support a model where

the universe began with a hot big bang at some finite point in the past. Further support for the model came from the accelerating expansion of the universe [5], the large-scale structure of galaxies [6], and the anisotropies of the cosmic microwave background [7]. These observations taken together appear to form a consistent model of the evolution and composition of our universe. ΛCDM is the name for the specific cosmological model that describes a universe that started with the big bang, includes a cosmological constant, Λ, associated with dark energy, and has a composition that includes cold dark matter, CDM.

The existence of the CMB and its remarkable smoothness, together with the known expansion of the universe, point to a past where the universe was hot, dense, and uniform. The current radiation temperature of the CMB, $T_0 = 2.725 \pm 0.001 K$[8], was reached after the universe expanded and cooled over billions of years. For an expanding universe with a scale factor $a(t)$, the expected relation with temperature is simply $T(t) \propto 1/a(t)$. The uniformity of the CMB today presents a problem known as the "horizon problem", since extrapolating back to the CMB's formation results in patches of the sky far outside of causal contact being at thermal equilibrium.

Cosmic microwave background anisotropy measurements provided one of the key parameters of ΛCDM: the flatness of the universe at large scales. This flatness is determined by comparing the energy density of the universe to the critical density necessary for zero curvature, which is parameterized by the dimensionless density parameter $\Omega(t) \equiv \varepsilon(t)/\varepsilon_c(t)$, where ε is the energy density, and ε_c is the critical density for a given Hubble parameter $H(t)$, given in Equation 1.1 [9]:

$$\varepsilon_c(t) \equiv \frac{3c^2}{8\pi G} H(t)^2 \, . \tag{1.1}$$

The result that the density of the universe today, Ω_0, is the critical density, Ω_c, to within less than one percent[10] is a somewhat surprising result. This has several important implications for cosmology. The density parameter $\Omega(t)$ can be related to the curvature κ, radius of curvature R_0, expansion rate $H(t)$, and scale factor $a(t)$ through the Friedmann equation, giving the expression in Equation 1.2

[9]:

$$1 - \Omega(t) = -\frac{\kappa c^2}{R_0^2 H(t)^2 a(t)^2} \ . \tag{1.2}$$

Since the right hand side of Equation 1.2 cannot change sign, the value of $1 - \Omega(t)$ also cannot change sign at any time, and if $1 - \Omega(t) = 0$, it is always zero and the curvature κ remains constant. Since the universe is known to be expanding, with the scale factor $a(t)$ greatly increasing, Equation 1.2 also shows that any small deviations from $\Omega = 1$ would be amplified with time, driving the density parameter away from its previous value. This implies a special value of $\Omega(t = 0) = 1$ with extreme precision, to produce the current value of $\Omega_0 = 1$. This is known as the "flatness problem."

The proposed solution to both the "flatness problem" and the "horizon problem" is an extremely rapid period of inflation in the first moments of the universe [11]. This inflationary period results in a miniscule volume being rapidly expanded, where quantum fluctuations are suddenly macroscopic structures, and all inhomogeneities are completely smoothed away. This also presents a solution to the problem of structure formation, with the quantum fluctuations providing the seeds of varying density to trigger gravitational collapses that eventually became large-scale structures. While inflation seems to solve some extremely important problems with ΛCDM cosmology, the evidence is still circumstantial. Direct evidence of inflation is being sought out through measurements of the CMB, as described in Section 1.2.3.

Following this initial period of inflation, the evolution of the universe according to big bang cosmology can be traced out according to the Λ CDM model. As the universe evolved, it transitioned into a hot plasma, and then eventually cooled enough that atoms could form. This point is known as recombination, when free electrons were absorbed to form hydrogen atoms, and the universe became transparent to radiation. This first free streaming light after the big bang is the cosmic microwave background. The underdensities and overdensities visible in the CMB anisotropies collapsed and cooled, forming large-scale structures. The universe continued to cool and form the first galaxies and stars, and at some point,

radiation from stars and supernovae was able to completely reionize the universe in an era known as reionization. The galaxies and stars continued to coalesce and evolve to form the universe we see today.

Observations of the temperature and polarization anisotropies in the cosmic microwave background, previously with the WMAP satellite [7] and most recently with the Planck satellite [10], can be used to determine many of the cosmological parameters of the ΛCDM model. The simple ΛCDM model can be fit to current observations using only six independent parameters. These parameters are the age of the universe, t_0, the density of baryons, $\Omega_b h^2$, the density of matter, $\Omega_m h^2$, the amplitude of the density fluctuations, Δ_R^2, their scale dependence, n_s, and the reionization optical depth, τ, where h is the reduced Hubble constant $H_0 = h/100$ (km/s)/Mpc [12].

1.2 The Cosmic Microwave Background

While the light from the CMB was formed billions of years ago, it was created in a period of the universe's evolution when the universe was still relatively homogeneous and isotropic, and it can mostly be described with straightforward physics. This period is known as recombination, when ionization fraction of baryons in the universe dropped below 0.5, as free electrons were absorbed into hydrogen nuclei to form atoms. Photons decoupled from matter and were able to freely stream without scattering off electrons, and so the universe became transparent. The CMB photons come from this surface of last scattering, the last point when the photons scattered off an electron before reaching observers today. The universe before recombination is very well approximated by an hot, ionized hydrogen plasma, with matter and radiation in thermal equilibrium. There were small amounts of other elements created in big bang nucleosynthesis that can be safely neglected for these calculations.

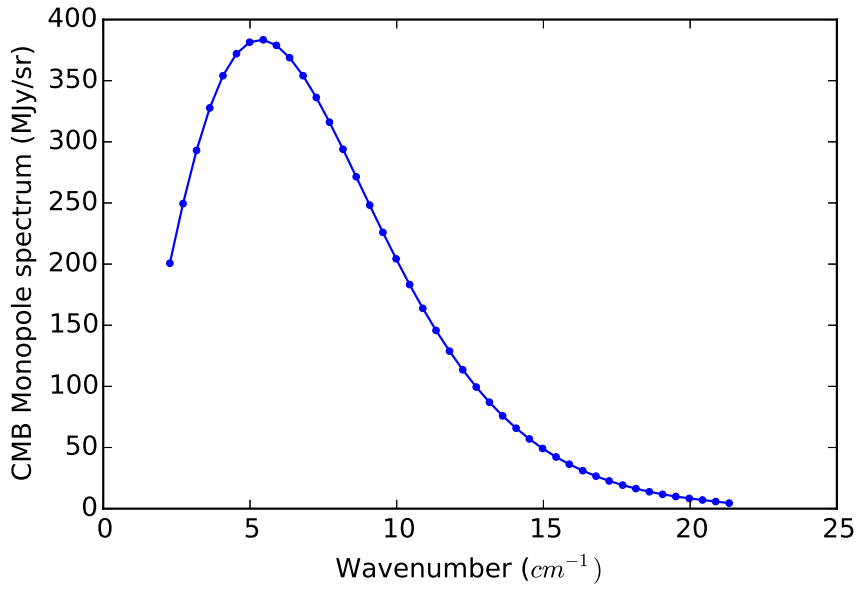

Figure 1.1: **CMB temperature spectrum measured by FIRAS on COBE** — Measured intensity of the CMB monopole from COBE on FIRAS is plotted along with the theoretical curve for a black body in thermal equilibrium at 2.725 K. The error bars on the data points are much smaller than the width of the curve and are not visible in this plot. Data from [8].

1.2.1 Monopole Temperature

The temperature of the CMB today is $T_{CMB} = 2.725 \pm 0.001K$, which can be determined from its spectral radiance at a given frequency using Planck's law, given in Equation 1.3, which describes the radiation emitted by a black body in thermal equilibrium:

$$B_\nu(T) = \frac{2h\nu^3}{c^2} \frac{1}{e^{h\nu/k_B T} - 1} \, . \tag{1.3}$$

All measurements of the CMB to date, including the detailed spectral measurements by FIRAS on COBE [8], show that the spectrum of the CMB follows the Planck spectrum to very high precision, as shown in Figure 1.1.

The CMB temperature measured across the sky is also extremely uniform, to within better than one part in 10^4. These observations imply that the entire observable universe was in thermal equilibrium when the CMB was formed, which

is surprising. The exact mechanism that the universe came to be in this state is not yet completely understood, although inflation is the proposed extension to ΛCDM that explains this. Regardless, starting with the state of the universe immediately before recombination, as a hot plasma of hydrogen in thermal equilibrium, the physics of the formation of the CMB can be understood. The temperature at which recombination must have happened can be determined using the Saha equation, which gives the ionization fraction for a given temperature. The Saha equation for hydrogen is given in Equation 1.4, where T is the temperature, n_H is the number density of neutral hydrogen, n_p is the number density of protons (ionized hydrogen), n_e is the number density of free electrons, m_e is the mass of the electron, and Q is the binding energy, $Q = (m_p + m_e - m_h)c^2 = 13.6$ eV [9]:

$$\frac{n_H}{n_p n_e} = (\frac{m_e kT}{2\pi\hbar^2})^{-3/2} e^{Q/k_B T} \ . \tag{1.4}$$

This can be rearranged in terms of the ionization fraction $X \equiv \frac{n_p}{n_p+n_H} = n_e/n_{baryon}$, and from charge neutrality $n_e = n_p$. The relative number density of baryons and photons is known from Ω_{baryon} and Ω_γ, and combining this with the expected black body spectrum of photons, the Saha equation can be solved for the temperature where $X = 1/2$, giving a temperature of $T_{recombination} \sim 3700K$ [9]. Using the expected $T(t) \propto a(t)^{-1}$, this can be related to the redshift, defined in Equation 1.5, where λ_e is the wavelength of emitted light and λ_o is the observed wavelength, due to the expansion of the universe:

$$z \equiv \frac{\lambda_0 - \lambda_e}{\lambda_e} \ . \tag{1.5}$$

The expected relationship between temperature of the universe and redshift z is given in Equation 1.6. This results in the CMB being emitted at a redshift $z \sim 1100$:

$$T = T_0(1 + z). \tag{1.6}$$

1.2.2 CMB Anisotropies

Beyond the monopole signature of the CMB, there are small temperature fluctuations, or anisotropies. There are two sources of anisotropy: primary anisotropies, generated at the same time as the CMB was formed, and secondary anisotropies, imprinted on the CMB after it was formed. These anisotropies are typically characterized by their angular power spectrum. Since they are small deviations from an average temperature, a temperature fluctuation ΔT in a direction on the sky $\hat{n}$ is defined, $\Theta(\hat{n}) = \Delta T/T$. Since the signal is across the celestial sphere, the multipole decomposition, given in Equation 1.7, is in terms of the spherical harmonics $Y_{\ell m}$, and is integrated over solid angle Ω:

$$\Theta_{\ell m} = \int \Theta(\hat{n}) Y^*_{\ell m}(\hat{n}) d\Omega \ . \tag{1.7}$$

For Gaussian fluctuations, they can be completely characterized by their angular power spectrum C_ℓ, defined in Equation 1.8:

$$\langle \Theta^*_{\ell m} \Theta_{\ell' m'} \rangle = \delta_{\ell \ell'} \delta_{m m'} C_\ell \ . \tag{1.8}$$

This is typically determined in terms of the power per logarithmic interval in wavenumber, defined in Equation 1.9:

$$\Delta^2_T \equiv \frac{\ell(\ell+1)}{2\pi} C_\ell T^2 \ . \tag{1.9}$$

The accuracy that the power spectrum can be determined is known as cosmic variance, which is due to the limitation that there are only $2\ell + 1$ modes to measure the power in a given multipole. This cosmic variance error is given in Equation 1.10 [13]:

$$\Delta C_\ell = \sqrt{\frac{2}{2\ell+1}} C_\ell \ . \tag{1.10}$$

The CMB is also polarized, and its polarization is most commonly described in terms of polarization patterns called E-modes and B-modes. While the polarization of light is typically described by the Stokes parameters, I, Q, U, and V, these parameters are dependent on the choice of coordinate system. E-mode and

B-mode describe patterns that do not depend on the choice of coordinate system, and have important relationships to the ways that polarization is generated in the CMB. E-mode polarization is the curl-free component of the polarization field, while B-mode polarization is the divergence-free component of the polarization field. These can be described with an angular power spectrum in the same way as the temperature field, C_ℓ^{EE} and C_ℓ^{BB}, respectively.

The temperature anisotropies seen in the CMB come from inhomogeneities in the density of the Universe at recombination. The ionized hydrogen plasma was a photon-baryon fluid, with photons coupled to electrons via Thomson scattering, and can be described by fluid mechanics. The compressions and rarefactions of the fluid with initial under and over densities are known as acoustic oscillations, and their effect on the temperature power spectrum has now been well measured [7, 10]. These acoustic oscillations are a scalar perturbation, described as a change in the density of the photon-baryon fluid. These density perturbations also partially polarize the CMB, but the mechanism can only produce E-mode polarization. The effect of these acoustic oscillations is seen in the angular power spectra C_ℓ^{TT} and C_ℓ^{EE} as shown in Figure 1.2, where the acoustic peaks are related to the number of compressions and rarefactions undergone by the fluid before recombination, with the peaks in E-mode polarization 180 degrees out of phase with the temperature peaks.

1.2.3 Inflation

As discussed in Section 1.1, inflation is a proposed extension to the ΛCDM model to explain the "horizon problem" and "flatness problem" indicated by the properties of the CMB. Direct evidence for inflation, if it occurred, is also expected to come from measurements of the CMB. The rapid expansion of the universe during inflation would create a background of gravitational waves. These gravitational waves would create tensor perturbations, which are transverse-traceless perturbations to the spacetime metric, with a quadrupolar stretching of spacetime. Tensor perturbations are expected to uniquely create B-mode polarization at large angular scales. Tensor perturbations also create temperature anisotropies, as shown

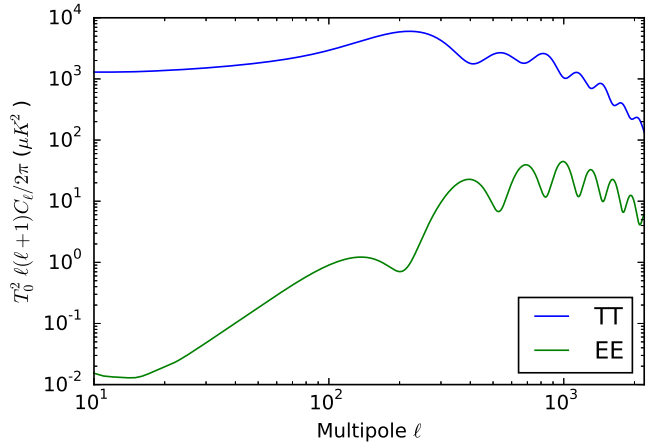

Figure 1.2: **Theoretical polarization power spectrum of primary CMB anisotropies from scalar perturbations** — The theoretical polarization power spectrum of primary CMB anisotropies sourced by scalar perturbations is shown for temperature, C_ℓ^{TT} and E-mode polarization, C_ℓ^{EE}. Power spectra calculated using the CAMB package [14].

in Figure 1.3. The strength of tensor perturbations is proportional to the energy scale of inflation, and is typically parameterized by the relative strength of tensor to scalar perturbations, r. Detailed measurements of the temperature power spectrum, as well as recent upper limits on the B-mode power spectrum at low-ℓ, have ruled out values of $r > 0.11$ The B-mode polarization power is known to be well below the measured C_ℓ^{TT} and C_ℓ^{EE} power spectra, as shown in Figure 1.4, with C_ℓ^{BB} shown for a value of r near the upper limit, $r = 0.1$.

1.2.4 Gravitational Lensing

The CMB can also be perturbed and anisotropies created between the time it is formed and its observation, known as secondary anisotropies. While these secondary anisotropies distort the primary CMB, recombination and the formation of the CMB is so well understood that we can reasonably recover both the original signal and understand the effects that caused these secondary anisotropies. Here the discussion is limited to the only secondary anisotropy expected to create B-mode polarization, which is gravitational lensing. Gravitational lensing of the CMB occurs when the CMB photons are deflected by gravitationally bound struc-

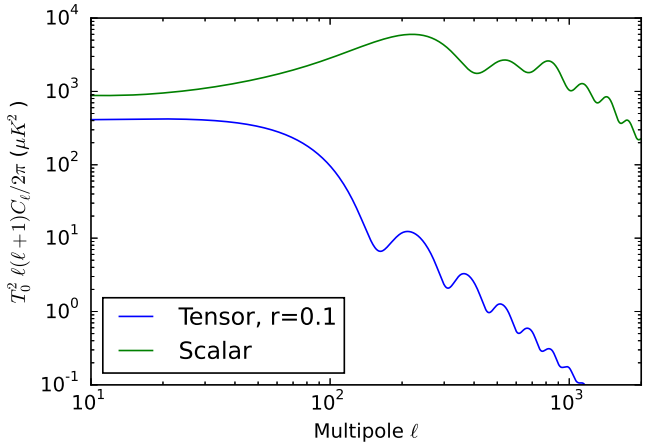

Figure 1.3: **Theoretical polarization power spectrum of primary CMB temperature anisotropies** — The theoretical angular power spectrum of primary CMB anisotropies from scalar and tensor perturbations are shown for temperature, C_ℓ^{TT}. Power spectra calculated using the CAMB package [14].

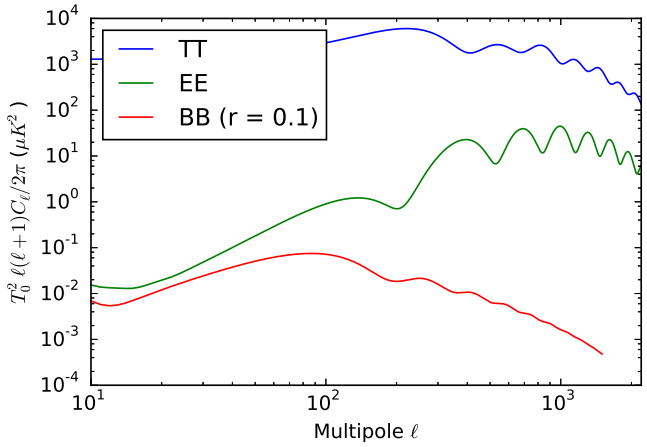

Figure 1.4: **Theoretical polarization power spectrum of primary CMB anisotropies** — The theoretical angular power spectrum of primary CMB anisotropies from scalar and tensor perturbations are shown for temperature, C_ℓ^{TT}, E-mode polarization, C_ℓ^{EE}, and B-mode polarization, C_ℓ^{BB}, for a tensor-to-scalar $r = 0.1$. Power spectra calculated using the CAMB package [14].

tures in the later universe. This bending of light preserves the original brightness of the signal, but it does affect both the temperature and polarization fields of the CMB. The lensing of the temperature field of the CMB has been characterized by Planck [15]. Gravitational lensing has a much more noticeable effect on the polarization of the CMB, since it perturbs the polarization field and mixes the E-mode and B-mode polarization patterns of the CMB. The gravitational lensing of E-mode polarization creates B-mode power at small angular scales where there is no other expected source of B-mode power, as shown in Figure 1.5. Measurements of the E-modes and B-modes and the correlations between them can be be used to re-create the gravitational potential field, and create a map of the integrated matter distribution between the CMB and now.

The matter distribution across the sky can be described as an angular power spectrum as well, and the height and shape of this curve will provide new constraints on cosmological parameters. The height of the matter power spectrum is sensitive to the sum of the neutrino masses, since the energy density of neutrinos in the universe affects structure formation in a well-predicted way. Neutrinos were relativistic in the early universe, with their high kinetic energy discouraging structure formation at small scales, but contributing to the overall amount of matter in the universe. The known composition of the universe and the existence of structure places loose upper limits on the sum of the masses of the known neutrino species, $\Sigma m_\nu < 50$ eV. Limits from recent cosmological data, including CMB lensing, are similar to the constraints placed by laboratory measurements, $\Sigma m_\nu < 0.23$ eV [10]. The next-generation of high-precision measurements of the CMB B-mode polarization, including POLARBEAR-2 and the Simons Array, are expected to greatly improve on these constraints, potentially distinguishing between the two possible neutrino mass hierarchies [16].

1.3 CMB Measurement Techniques

The first measurement of the CMB by Penzias and Wilson was made at radio frequencies [1], far from the peak of the spectral intensity at 160.2 GHz [8].

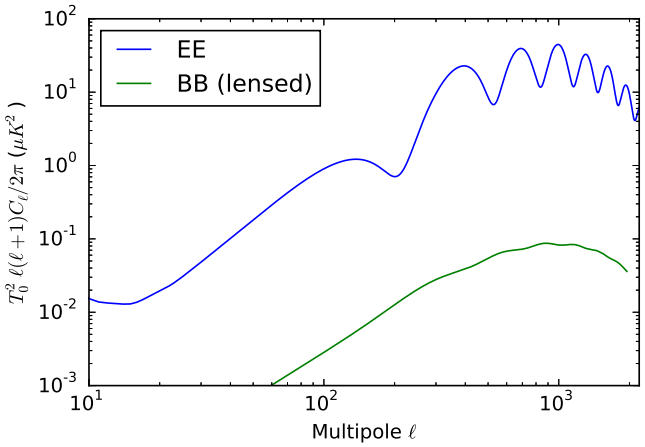

Figure 1.5: **Gravitational lensing of E-mode polarization** — The E-mode polarization power spectrum from primary anisotropies is shown, which is gravitational lensed to form B-mode polarization. The angular power spectrum of the resulting B-mode polarization, C_ℓ^{BB}, is also plotted. Power spectra calculated using the CAMB package [14].

The atmosphere is transparent across a large window in the radio portion of the electromagnetic spectrum, from approximately 30 MHz to 3 GHz. At higher microwave frequencies, there are strong absorption features from atmospheric gasses including water molecules and oxygen molecules, and the atmosphere is mostly opaque. Near the spectral peak of the CMB, there are several atmospheric windows between these absorption features, shown in Figure 1.6. Observing from a high elevation further reduces the amount of atmospheric absorption within these windows. Dry weather with low amounts of precipitable water vapor (PWV) in the atmosphere is also important for high transmission, as can be seen in Figure 1.6 showing the atmospheric transmission for two different values of PWV. The two best known locations on Earth for microwave observations are the South Pole and the Chajnantor Plateau of the Atacama desert. Both sites are at high elevations and have a long observing season with dry, stable weather. The Chajnantor Plateau, the location of the POLARBEAR site, is easily accessible year-round, but has much less research support infrastructure than the South Pole. One important advantage of the Chajnantor Plateau is that its mid-latitude site results in an observable sky area $f_{sky} > 0.8$, while telescopes at the South Pole are limited

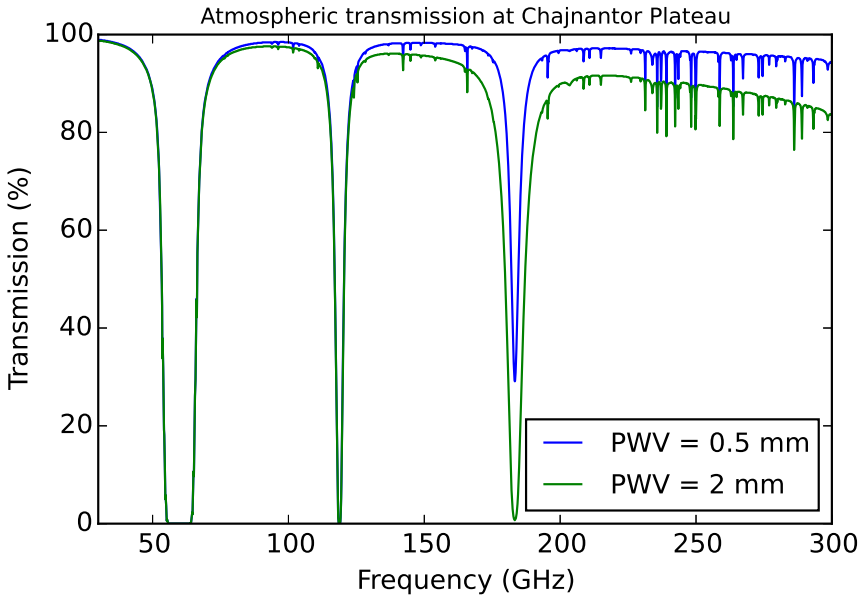

Figure 1.6: **Atmospheric transmission at microwave frequencies** — The atmospheric transmission at zenith is shown for the Chajnantor Plateau, at an elevation of 5100 meters, for a precipitable water vapor (PWV) of 0.5 mm and 2 mm. Historically, PWV < 0.5 mm is achieved for 25% of the observing season, and PWV < 2 mm is achieved for 75% of the observing season. Data calculated using the ATM package [17].

to about $f_{sky} = 0.2$.

Another option for observing at microwave frequencies is balloon-borne telescopes, which can stay aloft for observations for as many as 30 days above Antarctica. While this is a much shorter integration time than a ground-based experiment, the reduction in optical loading from the atmosphere can greatly increase the detector sensitivity. Multiple flights can build up integration time and observed f_{sky}, although recovering the instrument after a flight is never guaranteed.

Satellite-based CMB instruments have provided impressive measurements, most recently with the third-generation CMB satellite Planck [10]. The lack of optical loading from the atmosphere increases detector sensitivity, but the number of detectors is typically much more limited than what would be deployed on a ground-based instrument. The key advantage of space-based observations is that observations can be made at any microwave frequency band, as opposed to on

the ground where frequency bands must be carefully designed within atmospheric windows. With the recent rapid progress in CMB instrument sensitivity and understanding of systematic effects, ground-based instruments have the advantage of being infinitely more accessible for characterization and upgrades compared to a satellite instrument, which must be launched with relatively mature but possibly outdated technology.

The instantaneous sensitivity of an instrument is typically described by its NET_{CMB} (described in Section 2.6), which is the change in CMB temperature that can be measured with a signal-to-noise of 1 with one second of integration. For well-designed TES bolometers at microwave frequencies, the detector sensitivity is limited by the incident photon background loading, including optical loading from the instrument itself, the atmosphere, and the CMB. For a given instrument (with a set photon background), the only way to further increase sensitivity is to increase the detector count. The technology development that has enabled instruments to scale up from ~ 1 detector in the first generation of CMB polarization experiments, to ~ 1000 detectors in the current generation, and $\sim 10,000$ detectors in the next generation, is partly described in Chapter 2. The optical system of the instrument also affects instantaneous sensitivity, since NET_{CMB} is proportional to the optical efficiency η and the bandwidth $\Delta\nu$. The bandwidth for a ground-based instrument must typically be carefully placed within the atmospheric windows. Increasing the bandwidth is another important increase in sensitivity for the next generation of CMB instruments like POLARBEAR-2, described in Chapter 3.4.

For an instrument making observations with a given instantaneous sensitivity, typically given by NET_{CMB}, it produces maps of the CMB that have a resolution, which is set by the telescope optics (e.g. the primary mirror size), a sky area, f_{sky}, set by the observation strategy, and a map depth, typically given in $\mu K_{CMB} - arcminute$, set by the total integration time. The resolution sets the maximum multipole of the angular power spectrum to which the instrument is sensitive. The sky area, f_{sky}, for a single patch of sky determines lowest multipole at which the angular power spectrum can be calculated. The number of sky patches observed sets the number of modes measured and decreases the statistical

error, up to the cosmic variance limit given in Equation 1.10. The map depth determines the final sensitivity of the experiment to CMB fluctuations, and since it is proportional to integration time, it is directly proportional to the observation efficiency of an experiment. There can be many necessary gaps in observing, including time spent recycling the cryogenics, downtime from bad observing weather, and downtime from maintenance. There is also an efficiency within the time that the instrument is nominally observing the CMB, since each set of CMB scans may need to be accompanied by gaps from telescope turnarounds, detector tuning, detector calibration, and other short gaps. Improving the overall observing efficiency of an instrument can also make important gains in the final lifetime sensitivity. The instrument sensitivity can also be affected by systematic effects due to miscalibration, optical effects in the beam, electrical crosstalk, among other potential sources. The ultimate sensitivity of an instrument could be limited by these systematic effects, which would mean that additional integration time would not result in a more sensitive measurement.

1.4 Foreground Contamination in CMB Measurements

Since the CMB is the most distant light in the universe, there are many potential intervening foregrounds that can interfere with measurements, including extragalactic sources, our galaxy, and the Earth's atmosphere. Fortunately, the CMB is relative bright and well understood source, and with the right measurements, the effect of foreground contamination can be characterized and removed. This section discusses several types of foregrounds and their important features and impact on CMB measurements.

1.4.1 Extragalactic sources

Extragalactic point sources, like dusty galaxies and quasars, have extremely localized contributions to intensity, and those sources with a known location can be

masked and removed. There is still some unresolved background of extragalactic sources in CMB measurements, contributing a small level of excess signal. The polarized intensity of this unresolved background is expected to be small, so the effect of point sources on large-scale CMB polarization measurements is minimal. Point sources have the most effect on CMB temperature measurements at small angular scales and low frequencies.

1.4.2 Galactic foregrounds

Our galaxy is also relatively bright at microwave frequencies, as can be seen from the visible galactic plane in the all-sky WMAP or Planck maps. Observations away from the galactic plane are still looking out through the disk of our galaxy. For CMB polarization measurements, the relevant galactic foregrounds are those with a potential polarized component, from synchrotron emission and dust emission. The polarization fraction and direction from these emission mechanisms are influenced by the local magnetic field.

Synchrotron radiation is created by the acceleration of cosmic ray electrons within the galactic magnetic field. Synchrotron emission decreases with frequency following a power law $T \propto \nu^{-\beta_{synch}}$, where $\beta_{synch} \sim 3$, but varies across the sky and with frequency. The spectral index β_{synch} is related to the slope of the energy spectrum of the cosmic ray electrons which create the synchrotron radiation.

Dust thermal emission can be partially polarized when long dust grains align along magnetic field lines. The emission depends on the dust composition, grain size and temperature, with emission increasing with frequency following a power law $T \propto T_0 \nu^{\beta_{dust}}$, with $\beta_{dust} \sim 2$, where T_0, β_{dust}, and the polarization fraction vary across the sky [18].

The galaxy has an overall magnetic field structure that has been traced out through starlight polarization [19], and more recently with dust polarization measurements with Planck [20]. Starlight becomes polarized when these aspherical dust grains preferentially absorb light polarized along their long axis, and so the resulting polarization angle is orthogonal to that of thermal dust emission. These measurements can be used to model the large-scale structure and degree of disorder

in the galactic magnetic field. These models can be used to predict the expected polarization fraction of emission far from the galactic plane, which decreases for a more disordered local magnetic field [21].

Foreground removal is based on measuring the spectral information to determine the contribution from synchrotron emission, dust emission, and CMB emission which follows the Planck spectrum given in Equation 1.3. With the opposing frequency dependence of these two dominant foregrounds, there is some frequency around 100 GHz where contribution from each component is equal, and the total foreground level is expected to be at a minimum [22]. Measuring the CMB at its spectral peak would mean having to contend with higher foreground contamination for a small boost in CMB signal, so CMB instrument spectral bands are designed around this foreground spectral information. Foreground removal requires measuring or knowing the spectral signature of the foregrounds, and more complexity and variation in β_{dust} and $\beta_{synchrotron}$ requires more spectral bands to fully characterize the foreground spectra.

For temperature measurements, the CMB temperature anisotropies are brighter than the galactic foregrounds across $\sim 85\%$ of the sky [23] for 40 - 100 GHz [18]. For polarization the spectral indices of both components across the sky are not as well known, and the fraction of the sky where polarized foregrounds dominate even at the frequency where their contribution is minimal is not yet known. An estimate of the polarized foreground contributions at 90 GHz, based on the WMAP observations, is shown in Figure 1.7. Polarized synchrotron emission was fairly well characterized across the sky with WMAP [23], but WMAP did not measure at high enough frequencies to place strong constraints on the dust signal. Most ground-based CMB polarization experiments have focused on observing the "cleanest" patches of the sky, labeled in Figure 1.7 with $f_{sky} = 0.03$, where polarized foregrounds were expected to be small, based on their measured intensity and models of the polarization fraction. Planck has made initial measurements of polarized dust emission across the sky, and is beginning to characterize the dust and overall foreground emission in terms of its contribution to CMB B-mode polarization measurements [20], as shown in Figure 1.8. While the expected "cleanest"

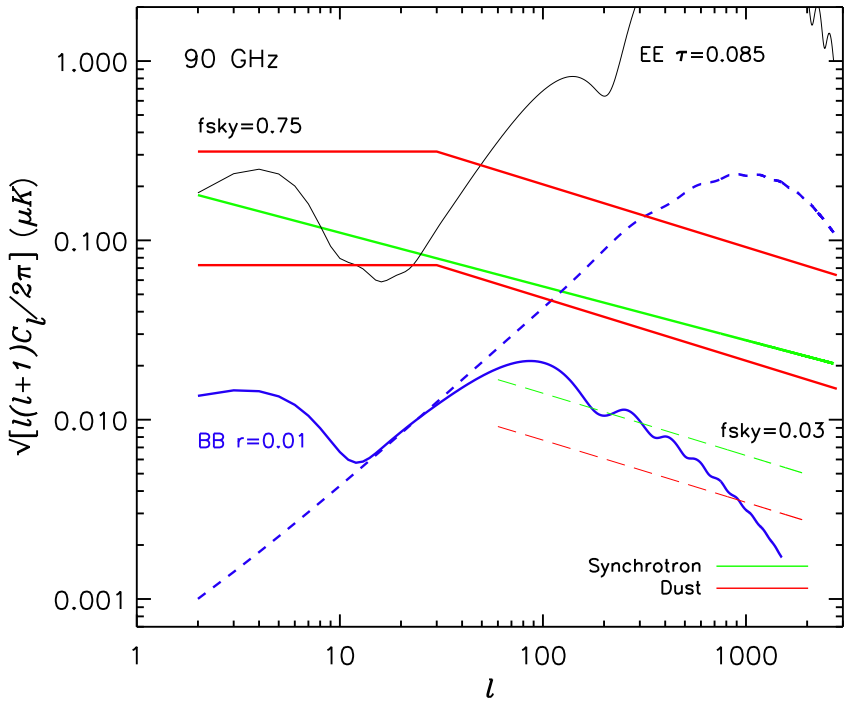

Figure 1.7: **Predicted polarized foreground amplitudes at 90 GHz** — The predicted polarized foreground amplitudes for synchrotron and dust at 90 GHz are shown, both for the majority of the sky, $f_{sky} = 0.75$ (solid lines), and the cleanest patches of the sky, $f_{sky} = 0.03$. The expected B-mode signal from lensing and from inflationary gravitational waves with $r = 0.01$ are also plotted. (Figure from Dunkley et. al 2009 [22]).

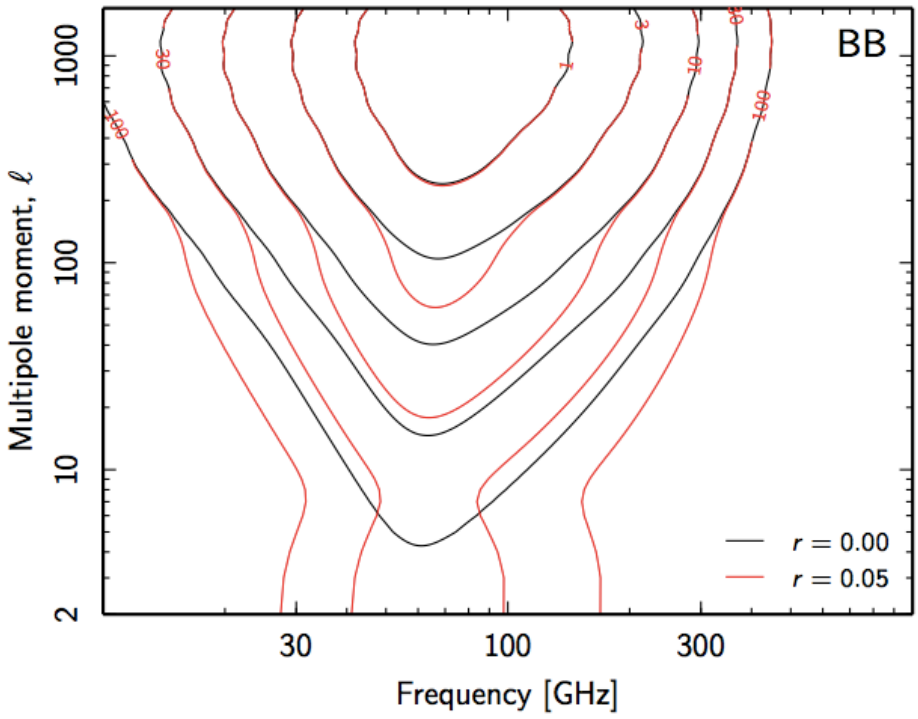

Figure 1.8: **Predicted B-mode amplitude of polarized foregrounds from Planck** — The relative amplitude of total polarized foregrounds and the CMB B-mode polarization for $f_{sky} = 0.73$ is shown as a function of multipole moment and frequency, $f(\ell, \nu) = [C_\ell^{fg}(\nu)/C_\ell^{CMB}]^{1/2}$. (Figure from Planck Collaboration: Planck 2015 results X [24]).

patches of the sky had low dust intensity, the polarization fraction actually can increase as intensity decreases, causing higher level of contamination for a CMB polarization experiment. This is thought to be due to a greater degree of alignment in the magnetic field along the line of sight for regions of lower optical depth.

1.4.3 Atmospheric contamination

For a ground-based experiment, the atmosphere also creates a foreground for measurement of the CMB. Thermal emission from the atmosphere creates an expected additional optical loading on the detectors, which has the effect of reducing their sensitivity. The atmosphere is also not a static foreground, as wind and water vapor vary the atmospheric signal on the focal plane on timescales of $\sim$

seconds, and can be seen in detector timestreams. This presents as low-frequency noise, which can be mitigated by scanning quickly across the sky to "freeze" out the atmospheric fluctuations, with a scan speed of $\sim$ degrees per second. The remaining atmospheric signals can be removed by subtracting a polynomial from the detector timestream of the scan. This can be done in a way that has a small impact on the underlying signal. Faster signal modulation can further reduce the atmospheric low-frequency noise, which can be done with a polarization modulator like a spinning half-wave plate. The atmosphere is not expected to be significantly polarized, if at all, and so other than its effect on the sensitivity of the instrument, it is not expected to present additional signals in CMB measurements. There is the possibility of small levels of circular polarization from the Zeeman splitting of oxygen lines in the Earth's magnetic field [18], and the alignment of ice grains in the upper atmosphere [25].

Chapter 2

Instrument Design

2.1 Introduction

The field of millimeter-wave instrumentation has made rapid progress over the past few decades, with significant advances enabling an instrument sensitivity that is only limited by the number of detectors. This chapter gives an overview of the instrument design and hardware, including supporting cryogenics and readout electronics, that are used for the focal plane in the POLARBEAR-1 and POLARBEAR-2 experiments, as well as several other contemporary CMB polarization experiments. In Section 2.2, we discuss superconducting transition edge sensor (TES) bolometers, the sensors that are commonly used for sensitive measurements of microwave radiation. In Section 2.3, we discuss superconducting quantum interference devices (SQUIDs), which are used as transimpedance amplifiers to measure the change in current across the TES sensor. In Section 2.4, we describe a lab system designed and built for testing of TES detectors and SQUIDs, including the cryogenics and cryocoolers used to cool these devices. In Section 2.5, we describe the multiplexing system that enables the readout of large numbers of cryogenic detectors. The POLARBEAR-1 and POLARBEAR-2 instruments are described in Chapter 3, and the next generation of CMB polarization instrumentation and beyond are discussed in Chapter 4.

2.2 Transition edge sensor bolometers

A bolometer measures the intensity of incident radiation by measuring the heat deposited by the absorption of radiative power. A cartoon of a bolometer is shown in Figure 2.1.

The bolometer consists of an absorber (shown in grey), which has a temperature T and a heat capacity C, and a thermal reservoir (shown in light blue) with a temperature T_{bath}, connected by a weak thermal link (shown in blue) with a conductance G. Power P incident on the absorber is dissipated through the weak thermal link to the thermal reservoir, with a time constant $\tau = C/G$. The power of the incident electromagnetic radiation, P_{opt}, can be determined by measuring this change in temperature ΔT, and changes in incident power can be measured if they are slower than the time constant τ. For a detector that requires an electrical bias (discussed below), there is also an electrical power contribution, P_{bias}, from power dissipated on a resistor R, so that $\Delta T = (P_{opt} + P_{bias})/G$. For millimeter wavelength electromagnetic radiation, bolometers are the most sensitive type of detector. The bolometer temperature T is measured using a transition edge sensor (TES), which uses the steep drop in resistance as a material goes through the superconducting transition to create an extremely sensitive thermometer. An example of this is shown in Figure 2.2, for a sample of titanium.

The width of the transition can be broadened by the applied current from the measurement, inhomogeneities in the transition temperature of the sample, and magnetic fields, but even for a perfect sample and measurement, there is still a finite width to this transition [26]. The slope of this transition $\frac{dR}{dT}$ is always positive, as the resistance is always decreasing as temperature decreases. This is parameterized by α, as shown in Equation 2.1:

$$\alpha = \frac{\delta log R}{\delta log T} = \frac{T}{R}\frac{\delta R}{\delta T} \, . \tag{2.1}$$

The transition depth is commonly parameterized by the fractional resistance $R_{frac} = R/R_{normal}$. Applying a constant voltage bias across the TES creates negative electrothermal feedback: incident P_{opt} increases the temperature T, which causes R to increase, which in turn decreases the electrical power $P_{bias} = \frac{V^2}{R}$.

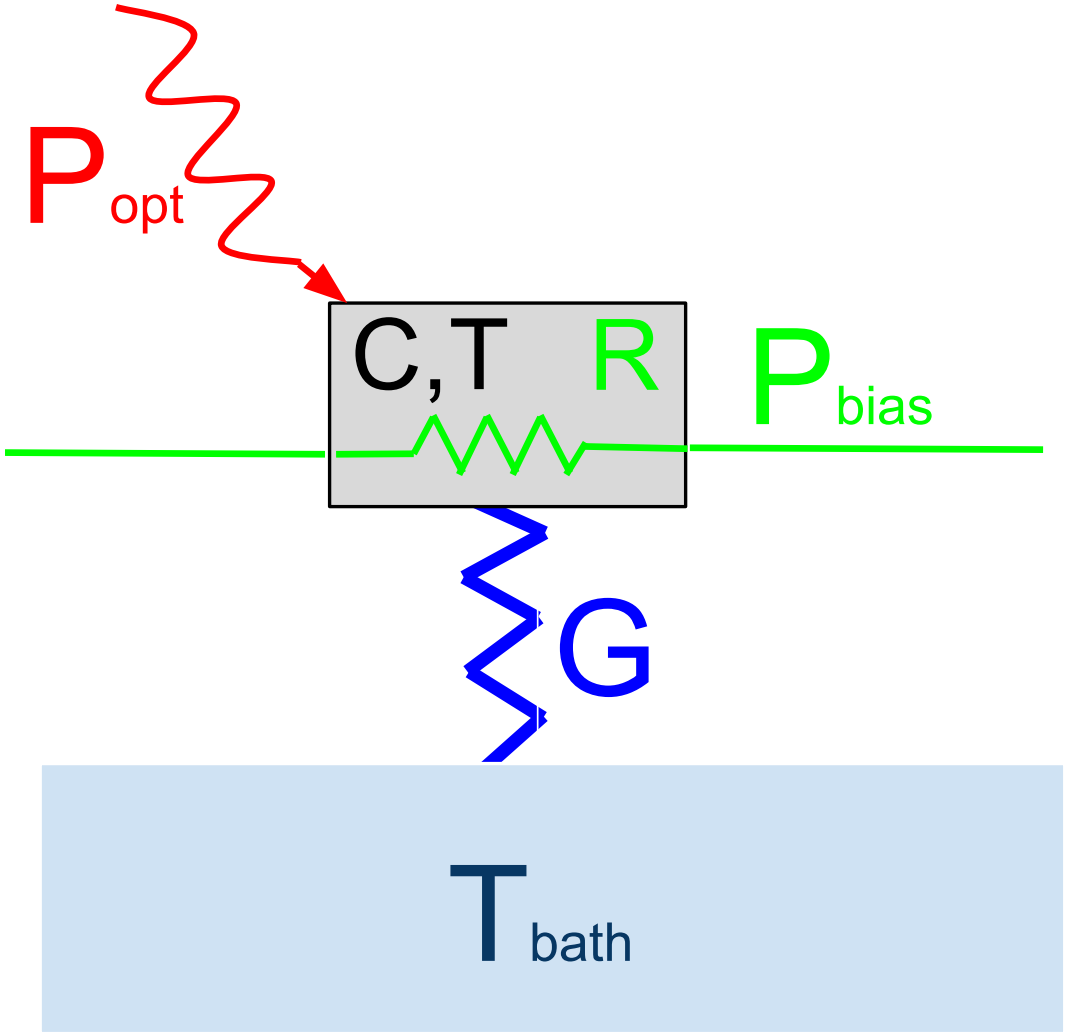

Figure 2.1: **Cartoon of a bolometer** — A bolometer is shown consisting of an absorber (grey), thermal link (blue), and thermal reservoir (light blue).

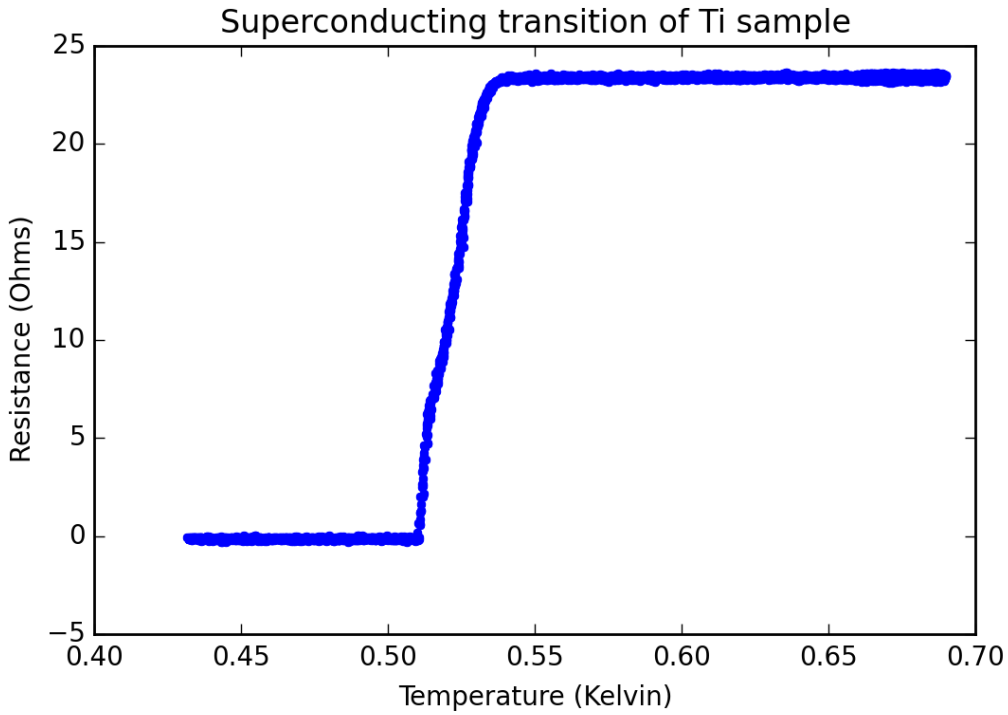

Figure 2.2: **Superconducting transition of titanium sample** — Plot of temperature vs. resistance for a thin film sample of titanium. The expected transition temperature is 0.39 K, but contamination in the fabrication process can alter the transition temperature.

In this way, the negative electrothermal feedback works to keep the total power $P_{total} = P_{opt} + P_{bias}$ incident on the bolometer island constant. This can also be demonstrated by dropping the electrical power P_{bias} on the bolometer. Figure 2.3 shows this for a dark bolometer (no incident optical power), starting in the normal state (constant resistance). As the voltage bias is decreased, the electrical power drops until the point where the TES enters the superconducting transition and the resistance also begins to drop. This point is the upward turn in the top plot showing applied voltage bias vs. measured current (IV curve). The applied voltage V and measured current I can be converted to a resistance R using $R = V/I$, and power P with $P = IV$, and these quantities are plotted in the bottom half of Figure 2.3. This shows the power P becoming constant at the downward turn in the plot, due to electrothermal feedback from the TES entering the superconducting transition.

With energy conserved, the power on the bolometer island must be equal to the power dissipated to the thermal reservoir. With a time-varying optical signal $\delta P e^{i\omega t}$, this is written out for a voltage-biased TES bolometer in the superconducting transition with negative electrothermal feedback in Equation 2.2, where $\bar{G}$ is the average thermal conductance between the bolometer and the thermal reservoir [27]:

$$\delta P e^{i\omega t} + P_{opt} + \frac{V^2}{R} - \frac{V^2}{R^2}\frac{dR}{dT}\delta T e^{i\omega t} = \bar{G}(T - T_{bath}) + (G + i\omega C)\delta T e^{i\omega t} \ . \quad (2.2)$$

The time-varying terms can be isolated, and simplified using the definition of α from Equation 2.1, to define a effective complex thermal conductance G_{eff}, which Equation 2.3 shows is increased by electrothermal feedback:

$$G_{eff} = \Big(\frac{P_{bias}\alpha}{T} + G + i\omega C\Big)\delta T e^{i\omega t} \ . \quad (2.3)$$

The time constant of the bolometer τ is decreased by electrothermal feedback, which we define relative to $\tau_0 = C/G$ in Equation 2.4:

$$\tau = \frac{\tau_0}{P_{bias}\alpha/GT + 1} \ . \quad (2.4)$$

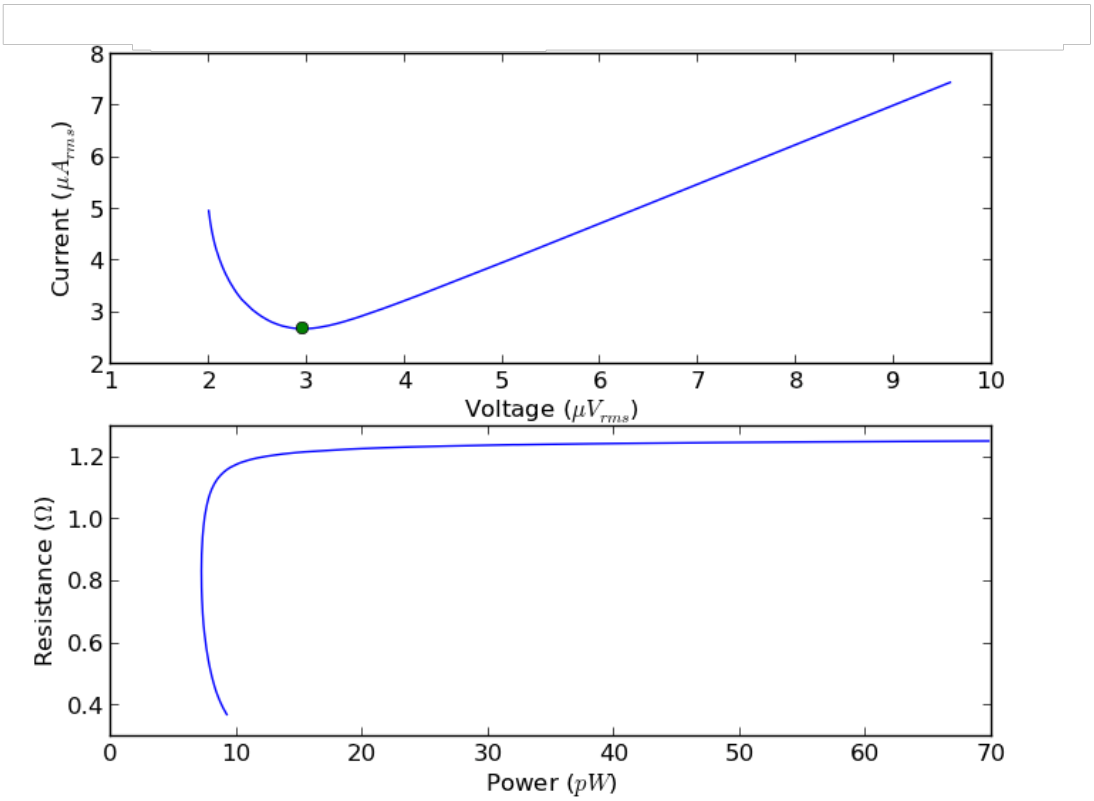

Figure 2.3: **IV and RP curve for bolometer** — The top curve shows the applied voltage bias vs. measured current for a dark TES bolometer being dropped into the superconducting transition. The bottom curve shows the derived quantities of resistance and power, showing that the power is kept constant in the superconducting transition by electrothermal feedback.

The frequency-dependent loop gain $\mathcal{L}(\omega)$ of the electrothermal feedback is defined as the ratio of the change in electrical power to the change in total TES power, shown in Equation 2.5, where $\mathcal{L} = P_{bias}\alpha/GT$ is the loop gain of the system:

$$\mathcal{L}(\omega) = \frac{-\delta P_{bias}}{\delta P_{total}} = \frac{P_{bias}\alpha}{GT(1+i\omega\tau_0)} = \frac{\mathcal{L}}{1+i\omega\tau_0} \ . \tag{2.5}$$

The equation for the time constant of the bolometer τ can be re-written in terms of the loop gain $\mathcal{L}$, simplifying to Equation 2.6:

$$\tau = \frac{\tau_0}{\mathcal{L}+1} \ . \tag{2.6}$$

The time constant τ can be determined by measuring the bolometer response across a range of frequencies, and fitting to a simple single-pole model, as demonstrated in Figure 2.4 and Figure 2.5. These measurements can be used to determine the achieved loop gain using Equation 2.6.

For a voltage-biased TES sensor, the voltage biased V_{bias} is controlled and the current I is measured in order to determine the incident optical power. The change in current δI induced by a change in optical power δP_{opt} is the responsivity, S_i [28]:

$$S_i = \frac{\delta I}{\delta P_{opt}} = \frac{-1}{V_{bias}} \frac{\mathcal{L}}{\mathcal{L}+1} \frac{1}{1+i\omega\tau} \ . \tag{2.7}$$

For a large loop gain $\mathcal{L} >> 1$, at frequencies ω that are small compared to the time constant τ, this simplifies to $S_i = -1/V_{bias}$. Since the detectors are operated with a constant voltage bias V_{bias} at high loop gain ($\mathcal{L}$ 10), the responsivity S_i is typically very stable and the TES response to optical power is linear. Lowering V_{bias} results in lowering R_{frac}, bringing the TES deeper into the transition, which increases the loop gain, and also increases the responsivity S_i. However, stable operation can be compromised by operating at a lower V_{bias}.

2.2.1 Bolometer saturation power

Returning to energy conservation on the bolometer island as shown in Equation 2.2, the steady-state conservation of energy on the bolometer island is de-

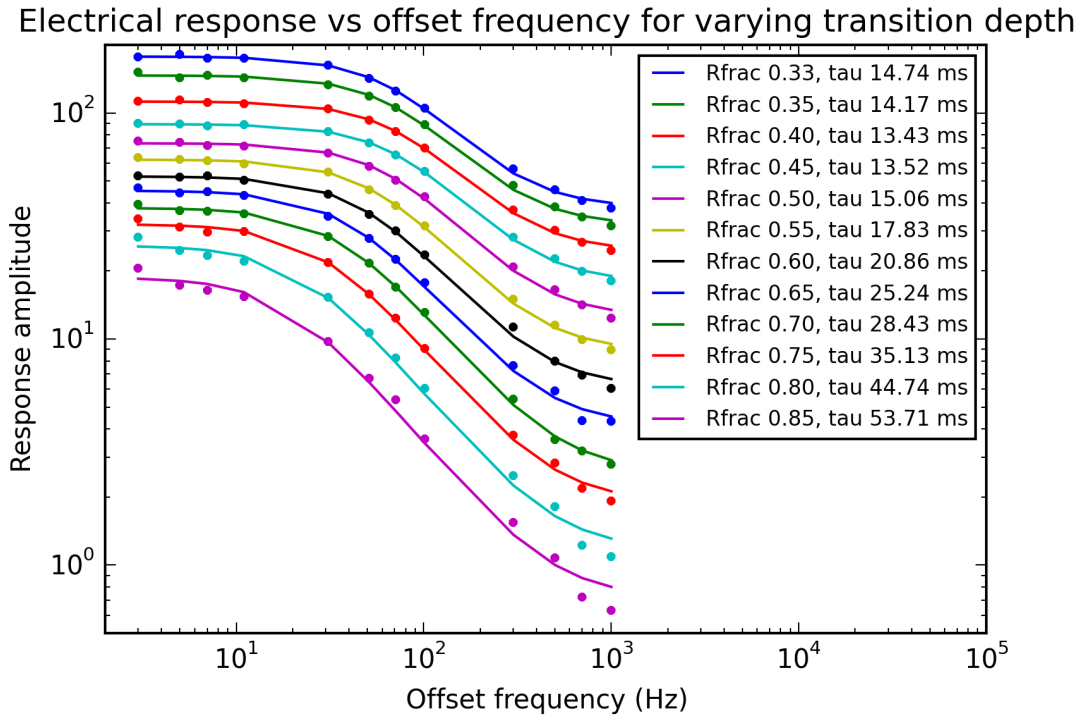

Figure 2.4: **Bolometer response to electrical tickle** — The response of a bolometer to a small electrical stimulus, at an offset frequency relative to the bias frequency, showing the response dropping off at high frequencies. The different curves are for different values of R_{frac} which results in a different loop gain for electrothermal feedback.

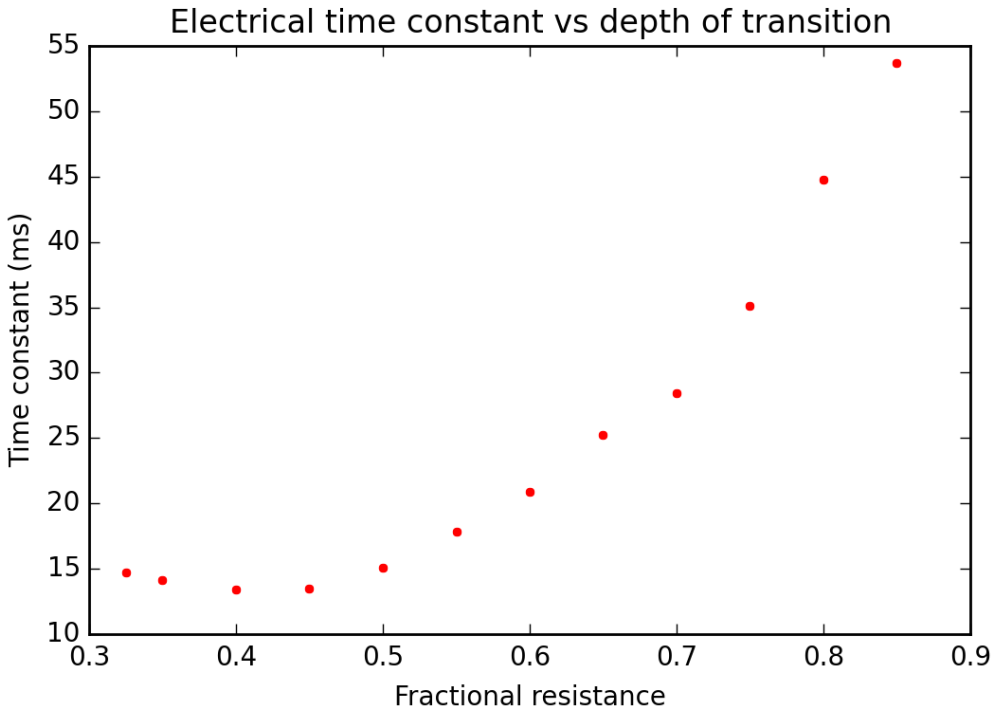

Figure 2.5: **Bolometer electrical time constant** — The electrical time constant of a bolometer measured for different transition depths R_{frac}, showing the decrease in time constant as R_{frac} decreases and the loop gain increases, as given in Equation 2.6.

scribed by the terms that are constant in time, in Equation 2.8:

$$P_{opt} + \frac{V^2}{R} = \bar{G}(T - T_{bath}) \ . \tag{2.8}$$

The total power deposited on the bolometer island equals the power conducted to the bath through the weak thermal link, which we can define as $P_{bath}(T) = \bar{G}(T - T_{bath})$. Equation 2.8 has an important qualifier: the temperature of the bolometer T must remain within the superconducting transition temperature T_c. If the applied power is too high, then the TES is driven out of its superconducting transition and into the normal metal state. This power can be measured using a dark bolometer ($P_{opt} = 0$) with applied electrical power P_{bias} as shown in Figure 2.3. The turnaround point of the IV curve is the point where P_{bias} becomes high enough to drive the TES into the normal state.

We can also define P_{bath} in terms of the properties of the thermal link. The temperature-dependent thermal conductivity is $\kappa(T) = \kappa_0 T^n$, and its relevant geometry is its cross-sectional area A and the length L. For the bolometers used in POLARBEAR, which are deposited on low-stress silicon nitride, the thermal conductivity of the thermal link is dominated by phonon conduction, where $n = 3$. This is related to the conductance by $G(T) = \frac{A}{L}\kappa(T)$. The power through this link from a bolometer at T_c to the thermal reservoir at T_{bath} is determined by Equation 2.9 [29]:

$$P_{bath} = \int_{T_{bath}}^{T_c} \frac{A}{L}\kappa(T)dT = \frac{A}{L}\frac{\kappa_0}{n+1}(T^{n+1} - T_{bath}^{n+1}) = \frac{A\kappa_0}{4L}(T_c^4 - T_{bath}^4) \ . \tag{2.9}$$

The saturation power is defined here as the maximum amount of optical power that can be incident on a voltage-biased TES bolometer with electrothermal feedback maintaining the bolometer's sensitivity and linearity. This saturation power P_{sat} is given in Equation 2.10 [26]:

$$P_{sat} = (1 - R_{frac})P_{bath}(T_c) \ . \tag{2.10}$$

Optical power greater than P_{sat} will cause the TES to heat up out of the superconducting transition and lose all responsivity. Increasing the values for the

conductance G and P_{bath} to increase P_{sat} comes with a noise penalty from thermal carrier noise, discussed below in Section 2.2.2, so the bolometer properties must be well-matched to the expected optical loading conditions during observations. For ground-based CMB observations, optical loading comes not only from the CMB signal, but also atmospheric loading (including weather variations) and loading from the instrument. Operating deeper in the transition (lowering R_{frac}) does increase P_{sat} without this noise penalty, but the lowest stable operating point is determined by many factors.

2.2.2 Bolometer noise sources

Detector noise is quantified in terms of the noise equivalent power (NEP), which is the incident power required to achieve a signal to noise ratio of one, in a 1 Hz bandwidth. This is related to the variance in power σ_p as defined in Equation 2.11:

$$\sigma_p^2 = \int |NEP|^2 df \ . \tag{2.11}$$

In this section we only discuss the dominant noise sources intrinsic to the bolometer, which are the thermal carrier noise, NEP_G, and the Johnson-Nyquist noise arising from the bolometer's resistance, $NEP_{Johnson}$. In Section 2.6, we go through all expected noise contributions for an integrated instrument observing the CMB, like POLARBEAR-1 and POLARBEAR-2.

The thermal carrier noise NEP_G comes from the energy fluctuations that are fundamental to any macroscopic system. For the bolometer specifically, energy fluctuations in the thermal carriers across the thermal link result in power fluctuations.

These fluctuations depend on the conductivity of the thermal link. The temperature dependence of the conductivity of the thermal link is parameterized by γ, given in Equation 2.12, where the temperature dependence of the thermal conductivity κ is given by $\kappa(T) = \kappa_0 T^n$:

$$\gamma = \frac{\int_{T_{bath}}^{T_c} (\frac{T\kappa(T)}{T_c\kappa(T_c)})^2 dT}{\int_{T_{bath}}^{T_c} \frac{\kappa(T)}{\kappa(T_c)} dT} = \frac{n+1}{2n+3} \frac{1-(T_b/T_c)^{2n+3}}{1-(T_b/T_c)^{n+1}} \ . \tag{2.12}$$

The thermal carrier noise, given in Equation 2.13, depends on the thermal conductance $G \equiv dP/dT$, the operating temperature and transition temperature T_c, the thermal reservoir temperature T_{bath}, and the temperature dependence of the conductivity of the link, parameterized by γ [30]:

$$NEP_G = \sqrt{\gamma 4 k_B T_{bath}^2 G} \ . \tag{2.13}$$

This can be re-written in terms of P_{bath} and T_{bath} to show that it scales with these quantities, as shown in Equation 2.14 [29]:

$$NEP_G = \sqrt{4 k_B P_{bath} T_{bath}} \sqrt{\frac{(n+1)^2}{2n+3} \frac{((T_c/T_b)^{2n+3}-1}{((T_c/T_b)^{n+1}-1)^2}} \ . \tag{2.14}$$

The second half of this equation can be optimized over the parameters n, and T_c/T_b, which for the POLARBEAR bolometers with $n = 3$, $T_c/T_b = 1.7$, results in a numerical value that is approximately 2.

Another unavoidable noise source for bolometers is the Johnson-Nyquist noise from the bolometer resistance R. This can be written as a current noise contribution $NEI_{Johnson} = \sqrt{4 k_B T_c / R}$, where we assume the bolometer resistance R has no significant resistance in series with it. With electrothermal feedback, this is reduced by the loop gain, as shown in Equation 2.15:

$$NEI_{Johnson} = \frac{1}{\mathcal{L}} \sqrt{\frac{4 k_B T_c}{R}} \ . \tag{2.15}$$

Converting this to a noise equivalent power, using the responsivity S_i from Equation 2.7, and also using the relation $P_{bias} = V_{bias}^2/R$, we get an expression for the contribution from Johnson-Nyquist noise, $NEP_{Johnson}$, shown in Equation 2.16:

$$NEP_{Johnson} = \frac{\mathcal{L}+1}{\mathcal{L}^2} \sqrt{4 k_B T_c P_{bias}} \ . \tag{2.16}$$

2.3 Superconducting Quantum Interference Devices (SQUIDs)

Reading out TES detectors requires measuring small changes in current, with a low noise amplifier with an input impedance that is small compared to the TES resistance ($R_{TES} \sim 1$ Ohm). Superconducting Quantum Interference Devices (SQUIDs) are well-suited for this task. SQUIDs are extremely sensitive magnetometers that consist of a superconducting loop with one or more Josephson junctions in parallel. A Josephson junction is two superconductors separated by an insulator, which superconducting Cooper pairs of electrons can tunnel through. The amount of flux within a superconducting loop is quantized in units of the flux quantum $\Phi_o = h/2e$, where h is Planck's constant and e is the electron charge. These two effects cause a superconducting loop with Josephson junctions to develop a current that is extremely sensitive to changes in the magnetic flux through the loop [31]. The TES current is coupled to a SQUID through an inductor, with all leads made of superconducting material, so the input impedance is small compared to the TES resistance (and can be further suppressed by negative feedback as described in Section 2.3.2).

SQUIDs with one Josephson junction are known as rf SQUIDs, which are less sensitive but relatively simple to manufacture. SQUIDs with two Josephson junctions in the loop are called dc SQUIDs. SQUIDs can be made of high-T_c materials, for superconducting operation cooled only by liquid nitrogen. SQUIDs made of low-T_c materials, which are superconducting at 4.2 K, require more complex cryogenics but are much more sensitive. In this discussion, "SQUID" is referring to low-T_c dc SQUIDs, the most sensitive type of SQUID, which are typically used for TES sensor readout for astronomical applications.

2.3.1 SQUID Properties

A simplified schematic of a dc SQUID set up to measure current is shown in Figure 2.6. The SQUID superconducting loop is shown as a circle, with the two Josephson junctions shown as X's. The SQUID can have a voltage or current

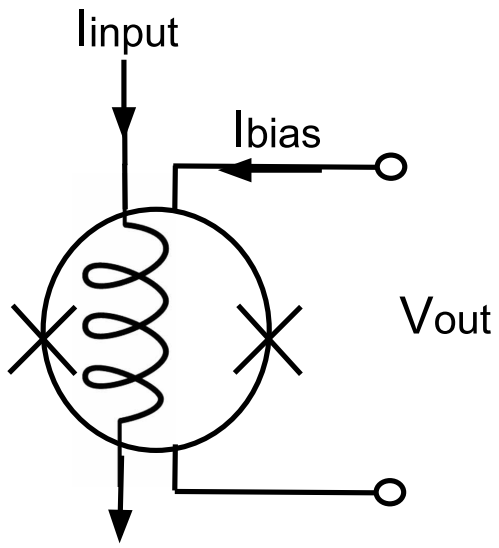

Figure 2.6: **Schematic of dc SQUID as transimpedance amplifier** — Schematic showing the configuration of a dc SQUID as a transimpedance amplifier, measuring the input current I_{input} and producing V_{out}.

applied directly to it, and the SQUID also has an input coil which lies inside of the superconducting loop, which is shown as an inductor symbol. Each Josephson junction has a resistance R_J, and a critical current I_c, which is the maximum supercurrent which can flow through the junction. As current I_{input} passes through the inductor, it generates a magnetic flux Φ_a inside of the loop, which is related to the magnitude of the current through the mutual inductance, M_{input}, as shown in Equation 2.17:

$$\Phi_a = M_{input} I_{input} \ . \tag{2.17}$$

The mutual inductance M_{input} is a design parameter that can be chosen based on the expected magnitude of current that will be measured. This relation can also be quantified as the current I_{Φ_0} which provides a quantum of flux, as shown in Equation 2.18:

$$I_{\Phi_0} = \Phi_0 / M_{input} \ . \tag{2.18}$$

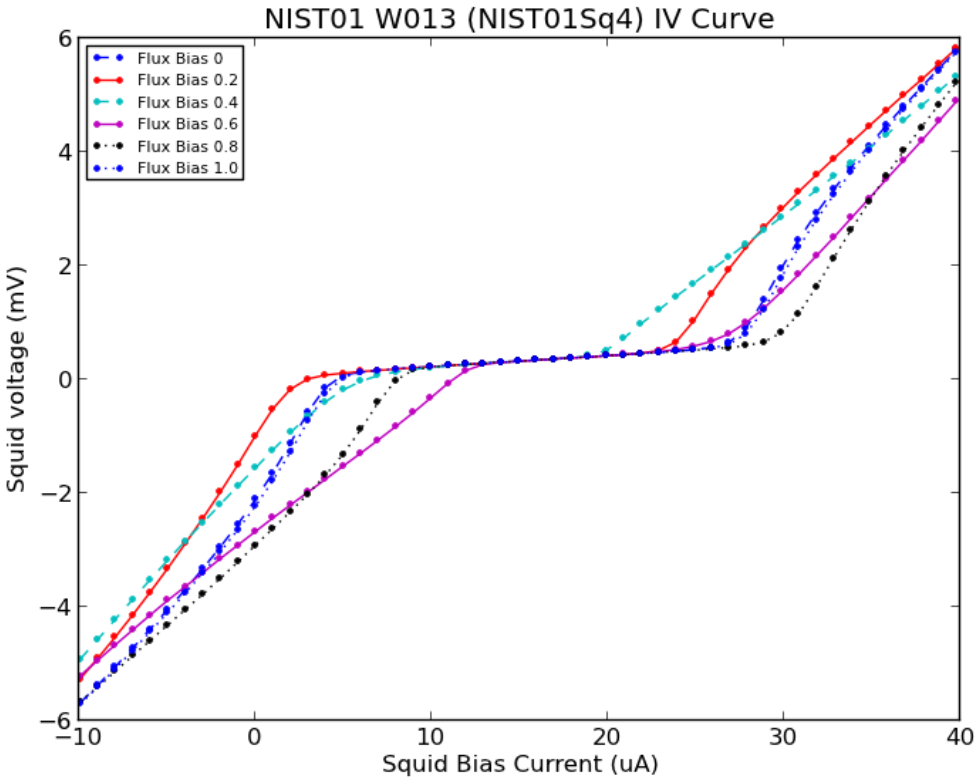

Figure 2.7: **IV Curve for SQUID** — IV curves for different flux values for SA13a design SQUID, fabricated by NIST.

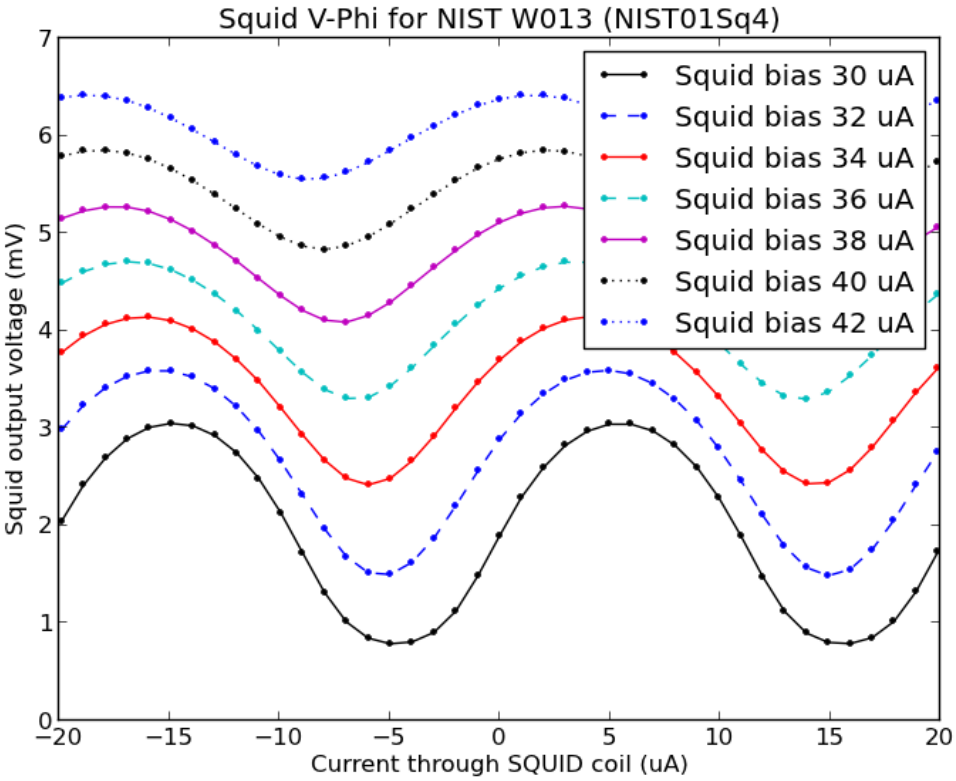

Figure 2.8: **V-Phi Curves for SQUID** — V-phi curves for different values of current bias for a SA13a design SQUID, fabricated at NIST.

As current is applied directly to the SQUID, the output voltage is zero until the current I_{bias} exceeds twice the critical current, I_c. At this point, the maximum supercurrent through the junction is exceeded and a voltage develops. This is shown in Figure 2.7 for several values of applied flux (applied through the input coil).

If the SQUID is biased with a current $I_{bias} \sim 2I_c$, changes in the magnetic flux cause the SQUID output voltage to oscillate with a period of Φ_0 [31]. This is shown in Figure 2.8 for several values of I_{bias}, where the applied flux is given by a current through the input coil. This can be approximated as a sinusoidal function, as shown in Equation 2.19, where V_{pp} is the peak-to-peak voltage, I_{input} is the current through the input coil, and I_{Φ_0} is defined in Equation 2.18:

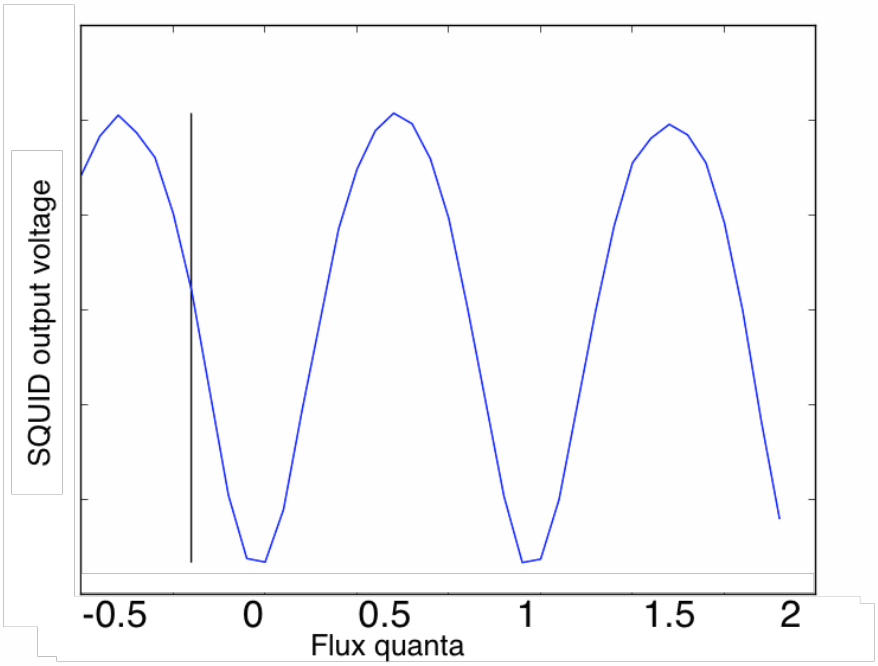

Figure 2.9: **SQUID output voltage vs. applied flux** — Plot of SQUID output voltage vs. applied flux, in units of the flux quantum Φ_0, showing their periodic relationship.

$$V_{out}^{SQUID} \approx V_{pp} \sin(2\pi I_{input}/I_{\Phi_0}) \; . \tag{2.19}$$

SQUIDs can also be voltage biased, resulting in an output current that is proportional to flux, with similar behavior.

The voltage response to a small flux change is defined in Equation 2.20:

$$V_\Phi = |\Big(\frac{\delta V}{\delta \Phi_a}\Big)_I| \; . \tag{2.20}$$

The maximum of this flux-to-voltage transfer coefficient V_Φ is at the point with the steepest slope (one of which is marked with the black vertical line in Figure 2.9), which occurs at known points given in Equation 2.21:

$$\Phi = (2n+1)\Phi_0/4 \; . \tag{2.21}$$

The current bias is chosen to maximize V_{pp}, and the flux bias is chosen as the point where V_Φ is maximally negative (as discussed further in Section 2.3.2) to maximize sensitivity. Using the approximation for V_{out} in 2.19, $\frac{\delta V}{\delta \Phi_a}|_{max} \approx \pi V_{pp}$. At this operating point, for small changes in flux, the SQUID output voltage δV is relatively linear with change in flux $\delta \Phi_a$. When using SQUIDs to read out current from a TES sensor, they are acting as a transimpedance amplifier, converting input current into output voltage, so we define a convenient transresistance measured in Ohms, shown in Equation 2.22 [32]:

$$Z_{sq} = M_{input} \frac{\delta V}{\delta \Phi_a}|_{max} = (\delta V_{SQ}/\delta I_{input})|_{max} \; . \tag{2.22}$$

There is very little usable dynamic range in this simple configuration, and the use of feedback to further linearize the SQUID output and increase its dynamic range is discussed in Section 2.3.2.

For a single dc SQUID, V_{pp} is very small, $\sim 10 \; \mu V$. In a series array of SQUIDs, the input coils and outputs are connected in series, and it can have a current bias applied through the array, so the series array essentially acts the same as a single element SQUID, with enhanced properties. For this arrangement, the output voltage V_{out} scales with the number of SQUIDs, N, while the output voltage

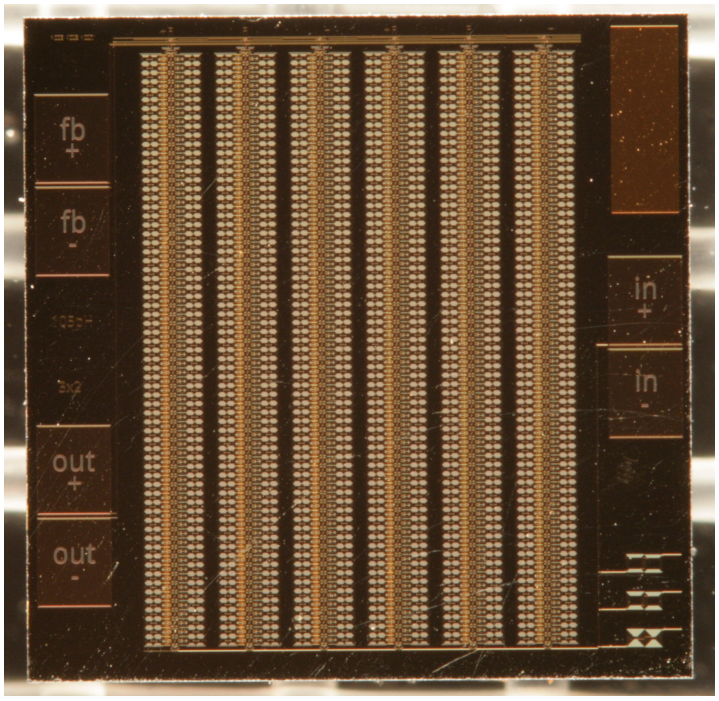

Figure 2.10: **Photograph of SQUID** — Photograph of a SA13a design SQUID, fabricated by NIST.

noise scales as $\sqrt{N}$, so the signal-to-noise ratio is improved by $\sqrt{N}$, where N can be on the order of 100 elements. For a series array of SQUIDs, the current noise can be below $\sim 5pA/\sqrt{\text{Hz}}$ (for $I_{\phi_0} \sim 25\ \mu A$), and Z_{sq} can be hundreds of Ohms. Series arrays of SQUIDs are sensitive to gradients in magnetic field across the array, which would cause non-uniform responses to flux by the SQUIDs within the array. These effects can be reduced by mounting the SQUID array on or within a superconducting shield to eliminate time-varying magnetic fluxes, and by enclosing the SQUID array inside of a μ-metal shield to reduce the absolute value of magnetic field present at the SQUID array [28]. A photograph of a series array of SQUIDs is shown in Figure 2.10. Each of the six columns has $N = 64$ dc SQUID elements in series. Bond pads are along the outer edges to connect to the input coil, feedback coil, and SQUID output. The size of the chip shown is approximately 1 cm by 1 cm.

2.3.2 SQUID Readout

Now that the basic characteristics and operation of a dc SQUID have been discussed, here we go into a more detailed description of the readout system that can take the small TES current at subKelvin temperatures, and convert it to a voltage measurable with room-temperature electronics. Figure 2.11 shows a SQUID with its input coil on the bottom left. The SQUID is biased with a constant current $I_{bias} \sim 2I_c$. The input current flows through the input coil L_{input}, applying a magnetic flux Φ_a. There is also a flux bias current which can be applied in addition to I_{input}, which is used to apply flux to the SQUID to get it to the operating point described in Equation 2.21. The SQUID couples to the current through the mutual inductance M_{input}, creating a small voltage as described in Equation 2.19. Figure 2.11 shows the SQUID in a configuration known as a flux-locked loop. The SQUID output voltage is now fed into an amplifier with negative feedback connected back to the SQUID's input coil, working to cancel out any changes in flux. The flux inside the SQUID is now constant, and the voltage across the feedback resistor is proportional to the input current I_{input} [31]. The flux-locked loop extends the dynamic range of input current that can be measured, and keeps the transimpedance constant over this broader range, which is determined by the circuit parameters. If the input current exceeds the dynamic range, the SQUID array "flux-jumps" to a new state one or more flux quanta away from the original working point, which greatly decreases the dynamic range of the readout due to the extra current in the flux-locked loop. The overall dynamic range of the SQUID is set by M_{input} and can be chosen so that flux-jumping is a rare occurrence.

The generic flux-locked loop configuration is very common for reading out SQUIDs, and there are many variations on its implementation. Feedback is typically applied through a dedicated inductive feedback coil. The specific configuration shown in Figure 2.11 is known as shunt-feedback, since the feedback is coupled directly into the SQUID's inductive input coil. This is the SQUID readout configuration used in POLARBEAR-1. Directly coupling the input coil to room temperature electronics makes it susceptible to rf pickup, which must be carefully shielded against. The configuration is necessary to keep the SQUID input

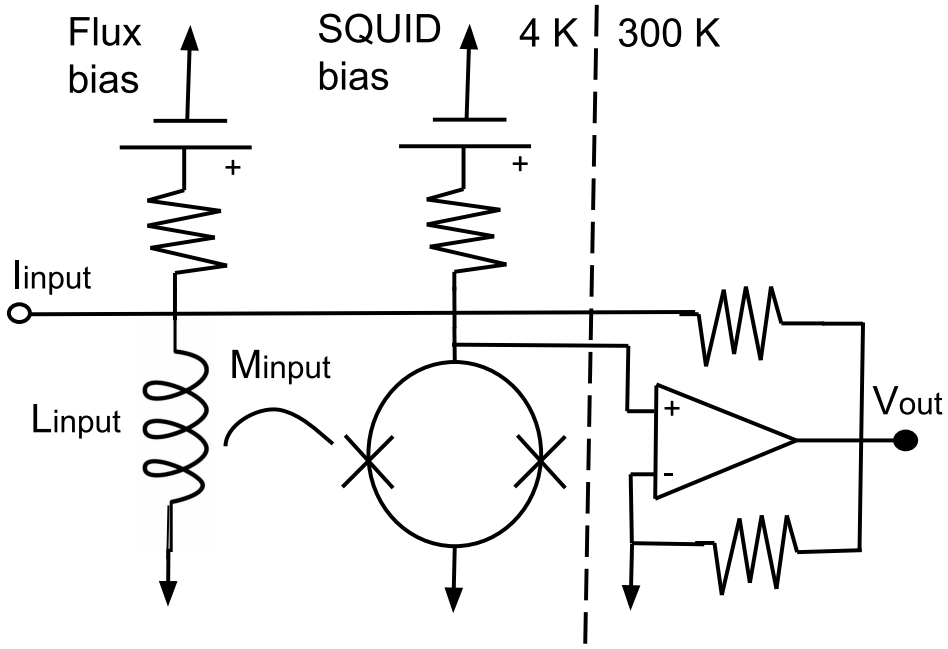

Figure 2.11: **Circuit diagram of SQUID operated in shunt-feedback configuration** — Diagram of a SQUID acting as a transimpedance amplifier, with negative feedback applied to keep the flux within the SQUID constant.

impedance very low, since the SQUID is in series with the TES detectors, and the TES impedance must be dominant. In the shunt-feedback configuration, the input impedance is suppressed to $< 100\ m\Omega$ for a feedback resistor value of $10\ k\Omega$ [32].

One limitation of the flux-locked loop is the achievable readout bandwidth, which is much less than the SQUID bandwidth ($\sim$ 100 MHz). The readout bandwidth determines how fast of a measurement is possible, and for a frequency domain multiplexing system, this bandwidth determines how many channels can be used. Since the SQUIDs must be at cryogenic temperatures, with minimal thermal loading, and the amplifiers and other readout electronics are at room temperature, there are minimum lengths for the cryogenic wiring that carries the feedback signal. For a 1 meter wiring length, the theoretical limit for the bandwidth of a flux-locked loop is about 20 MHz [33], which is due to the propagation delay in the feedback signals. In practice, the bandwidth can be much less, due to the difficulty in maintaining stability in the feedback loop across the entire bandwidth in the presence of multiple phase delays, resonances, and non-ideal components, which can all cause resonances and oscillations. For the shunt-feedback configuration used in POLARBEAR-1, the achieved bandwidth was approximately 1.3 MHz [32], with tightly constrained cold wiring lengths. There are many ways to try to improve the usable bandwidth, and for POLARBEAR-2, traditional shunt-feedback as shown in Figure 2.11 has been replaced with digital baseband feedback, which extends the bandwidth to $\sim$ 10 MHz (described further in Section 2.5.

2.3.3 SQUID Noise Contribution

Using a SQUID ammeter to read out bolometers makes a contribution to the bolometer noise that can be kept small compared to other noise sources (see Section 2.6). The SQUID fundamental noise is characterized as a noise equivalent current, NEI_{SQUID}, which can be referred to the input of the bolometer as a noise equivalent power NEP_{SQUID} using the bolometer responsivity at high loop gain from Equation 2.7:

$$NEP_{SQUID} = NEI_{SQUID} \times \left(\frac{\delta I}{\delta P_{opt}}\right)^{-1} = \frac{NEI_{SQUID}}{S_i} \approx V_{bias} \times NEI_{SQUID} \ . \tag{2.23}$$

There is also a noise contribution from any non-ideal amplifier used to measure the SQUID output voltage, which has a characteristic voltage noise E_n. This can be converted to a current noise NEI_{amp} using the transimpedance of the SQUID Z_{SQ} (given in Equation 2.22), and then to a noise equivalent power NEP_{amp} as shown in Equation 2.24:

$$NEP_{amp} \approx V_{bias} \times \frac{E_n}{Z_{SQ}} \ . \tag{2.24}$$

These two terms NEP_{SQUID} and NEP_{amp} are a significant contribution to $NEP_{readout}$ for POLARBEAR. Since these two noise terms are both proportional to V_{bias}, being able to operate a given bolometer at a lower R_{frac} would reduce $NEP_{readout}$. Also, a bolometer with P_{bath} much higher than P_{opt} would require more electrical power and a higher V_{bias} to stay within the superconducting transition, causing an additional noise penalty beyond the additional thermal carrier noise discussed in Section 2.2.1 and Section 2.2.2.

2.4 Performance of a 4 Kelvin pulse-tube cooled cryostat with dc SQUID amplifiers for bolometric detector testing

Commercial cryocoolers have become an attractive alternative to liquid cryogen cooling for experimental studies requiring temperatures below 4 K. As the reliability, cost, and cooling power of cryocoolers have improved, the main drawbacks remain the electromagnetic interference (EMI), mechanical vibration, and temperature fluctuations inherent to cryocoolers [34]. These effects can have a significant impact on sensitive measurements, especially the operation of superconducting quantum interference (SQUID) devices. The pulse-tube cooler (PTC) has the advantage of having no moving parts inside the cold head, reducing the

vibrational noise and EMI generated. Two-stage Gifford-McMahon type pulse-tube coolers are able to reach temperatures below 4 K [35] Many studies have investigated the use of pulse-tube coolers to cool high-T_c SQUIDs [36, 37, 38].

One type of detectors for millimeter-wave astronomy is bolometers, which measure the incident electromagnetic power via the amount of heat deposited on an absorber, typically using a resistive thermometer. Bolometers can achieve high sensitivity by reducing thermal background power loading and other sources of thermal noise by cooling the bolometer and its thermal bath to cryogenic temperatures [27]. The nature of cooling an array of detectors on a telescope installed in a remote location, as is necessary for many millimeter-wave experiments, favors using a cryocooler over liquid cryogens if possible, and several experiments are now using pulse-tube coolers [39, 40]. The current state-of-the-art millimeter-wave detectors are superconducting transition edge sensor (TES) bolometers, read-out by SQUID amplifiers. These bolometers achieve their extreme sensitivity to incident power by means of a superconducting film operating within its steep normal-to-superconducting resistance transition ($T_c \sim 0.5K$) [26]. When operated with a bath temperature $T < 0.25K$, the inherent thermal carrier noise of the bolometer is minimized to the point that, after reducing read-out and other external noise sources, the detectors can reach a sensitivity where they are limited only by the photon noise of the thermal background they observe [41]. In this section we report on the initial design, testing, and operation of a pulse-tube cooled cryostat for TES bolometer testing at sub-Kelvin temperatures.

2.4.1 Refrigeration technology

The main cryocooler used for this work is the PT415 cryorefrigerator by Cryomech Inc., a two-stage pulse-tube cooler with a base temperature of 2.8 K[1]. The remote motor option was chosen, as the motor is known to be a major source of noise. The motor was mounted adjacent to the cryostat, on the side of the cryostat's supporting structure, with vibrational and electrical isolation. A Cryomech vibration isolating bellows assembly was placed between the top of the pulse tube

[1]Cryomech Inc., 113 Falso Dr., Syracuse, NY 13211 USA, www.cryomech.com

head and the cryostat. The PTC's first stage has 40 W cooling capacity at T = 45 K, and an unloaded base temperature of 32 K. The second stage has 1.5 W of cooling power at T = 4.2 K, and an unloaded base temperature of 2.8 K. The PTC and its associated compressor require electricity and cooling water to operate.

To achieve sub-Kelvin temperatures, the pulse-tube cooler is used in combination with a closed-cycle 3He/4He/3He evaporation refrigerator from Chase Cryogenics ("He-10 fridge")[2]. This refrigerator has two cold heads, the "ultra-cold head" and "intermediate-cold head," as well as an additional heat sink point at the heat exchanger between the two heads. The ultra-cold head is expected to operate at approximately 250 mK under a typical load of 2 μW, with an unloaded base temperature of 220 mK. The intermediate-cold heat is expected to operate at approximately 350 mK with 50 μW of loading, with an unloaded base temperature of 330 mK. The refrigerator is a closed-cycle system, and recycling is accomplished using entirely electrical controls. Because of heat generated during the cycle, the refrigerator requires at least 0.5 W of cooling power available. Voltage is initially applied to heaters at the helium cryopumps to liberate the gases. He^4 is able to condense at a lower point cooled to the temperature of the 4 K stage, which is less than the critical temperature of He^4, $T = 5.19K$. A voltage-controlled gas-gap heat switch is opened, and evaporative cooling of the He^4 lowers the temperature of the cold heads to approximately T = 1 K, which allows He^3 to condense (critical temperature 3.35 K). Evaporative cooling of the two stages of He^3, with the intermediate-cold head acting as a buffer, results in the ultra-cold head reaching its base temperature of about 220 mK. The entire cycle can be accomplished in approximately 2 hours, and the hold time with typical loading is several days.

2.4.2 Thermal architecture

For convenience, the cold stages are referred to by their nominal temperature, e.g. "4 K stage." The cryostat design is shown in Figure 2.12, and a photograph is shown in Figure 2.13. The cold stages are supported by thermally isolating supports made of materials selected with a low thermal conductivity at

[2]Chase Cryogenics Ltd., 140 Manchester Rd, Sheffield, UK, www.chasecryogenic.com

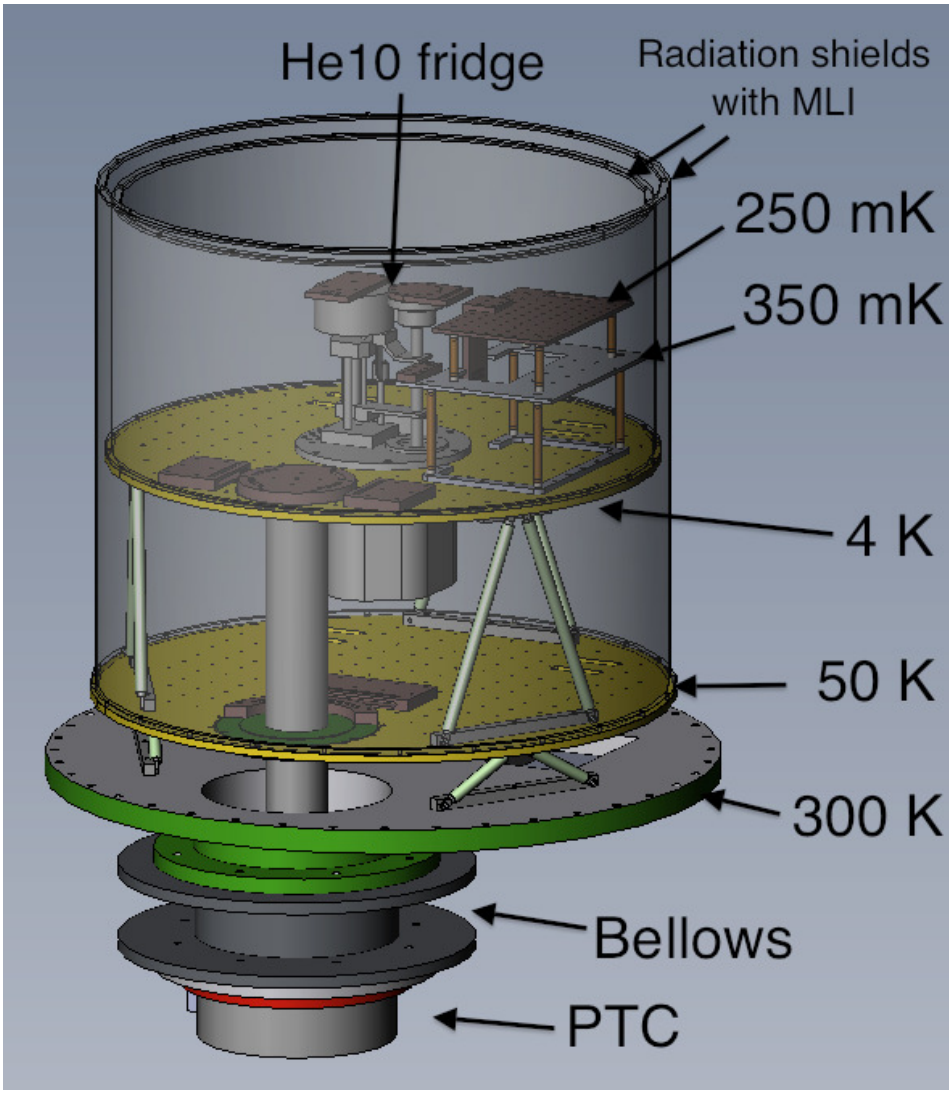

Figure 2.12: **Test cryostat drawing** — Drawing of the cryostat design, with labels for the cryocoolers and temperature stages.

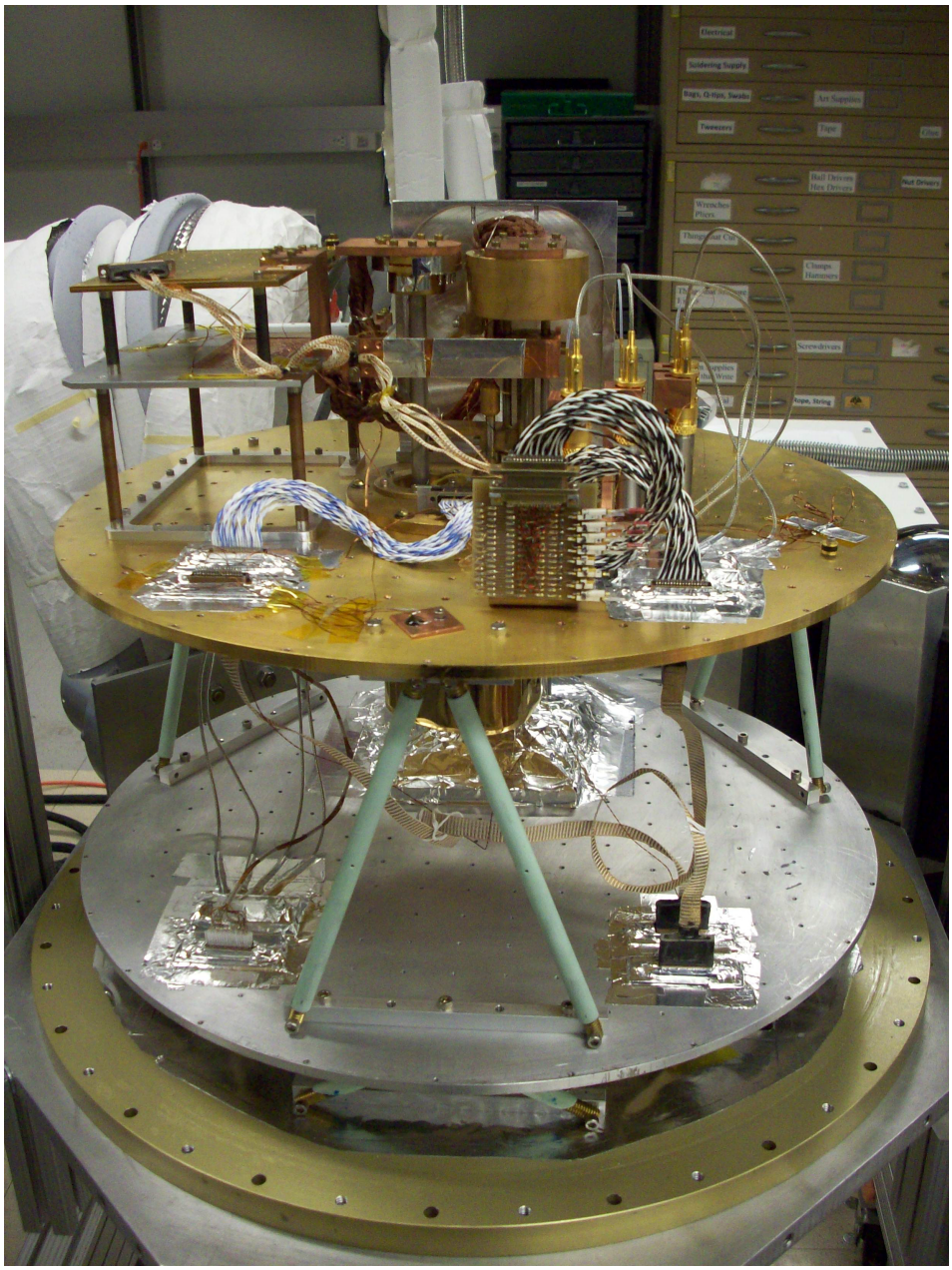

Figure 2.13: **Inner test cryostat** — Photograph of cryostat, with outer shells removed (rotated 180 degrees from drawing view).

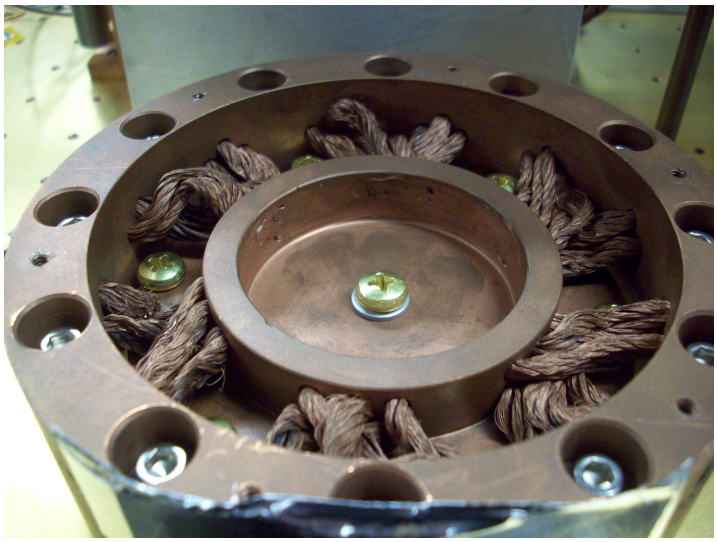

Figure 2.14: **Heat strap** — Photograph of copper heat straps to PTC head.

the relevant temperature values [42]. For supports used at temperatures above 4 K, hollow rods of G-10 fiberglass-epoxy laminate were used. For the sub-Kelvin stages, conductive loading needs to be minimized as much as possible, and so materials with lower thermal conductivities were required. For these stages, hollow rods made of two types of Vespel® polyimide resin were used for supports, with thermal conductivities at 4 K approximately an order of magnitude lower than G-10, but with much higher cost. Vespel SP1 was used for the supports from 4 K to 350 mK. For temperatures below 2 K, the same polyimide resin with 40% graphite added, Vespel SP22, has an even lower thermal conductivity. This Vespel SP22 was used for supports from 350 mK to 250 mK. All cryogenic wiring is small gauge wire made of low thermal conductivity material (manganin, phosphor bronze, superconducting NbTi for $T < 10$ K) with thermal breaks at each cold stage. A total of about 150 wires were permanently installed from room temperature to the 4 K stage, and as many as 48 wires can be brought to the 250 mK stage.

To thermally connect the refrigerators to the cold stages, heat straps were designed that would have a high thermal conductivity with minimal vibrational coupling. Copper speaker wire is ideal for this purpose as it is flexible and readily available in high purities. The thermal conductivity of copper depends strongly on purity at low temperatures, so speaker wire was selected (Bell'O SP7605 High

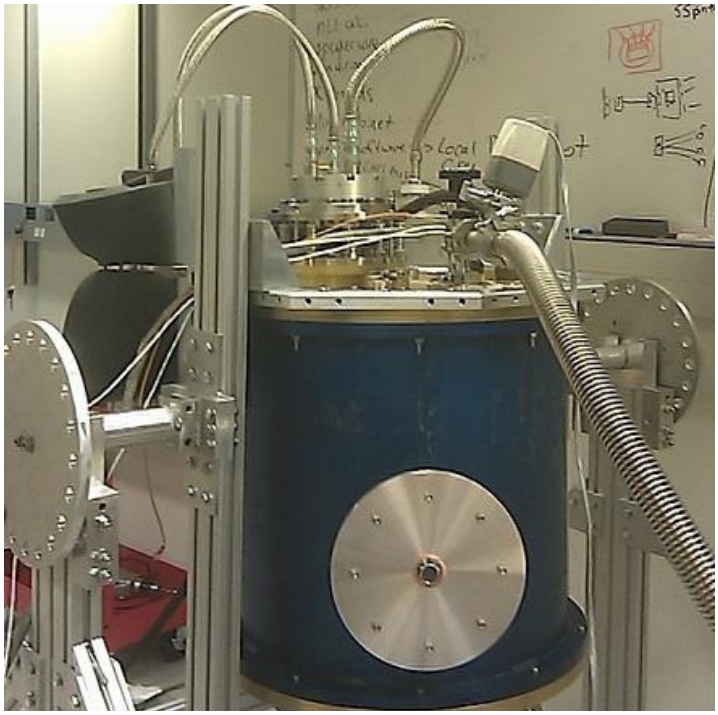

Figure 2.15: **Outer shell of cryostat** — Photograph of outside of cryostat.

Performance 14 AWG speaker wire) that was made of 99.99% oxygen-free copper, the highest purity readily available for commercial speaker wire. The heat straps consist of speaker wire stranded together and TIG welded to copper blocks to interface with the cold heads and the cold stages (see Figure 2.14). This general design was used for all the heat straps in the system.

300 K stage: The outer room-temperature shell (Figure 2.15) is a large aluminum vacuum chamber capable of maintaining a vacuum of $P < 10^{-6}$ Torr. A turbomolecular pump with backing pump is used to pump down to $P = 10^{-3}$ Torr, before beginning cooling with the PTC. The vacuum pressure is further improved by cryopumping, reaching a pressure at the cryostat inlet of $P = 10^{-6}$ Torr. To improve the effectiveness of cryopumping, pieces of activated charcoal attached to a copper mount are mounted on the 4 K and 50 K stages. These are baked at $100\,\mathrm{deg}\,C$ between each run.

50 K stage: The first stage of the PTC is used to cool an intermediate "50 K stage" with a large aluminum cold plate. This stage acts as a thermal break for radiative and conductive loading, and typical and acceptable loading can be

near the capacity of the cooler, resulting in a temperature of about 40-45 K. A cylindrical aluminum radiation shield attaches to the 50 K cold plate and encloses the inner stages, with six layers of aluminized mylar (multi-layer insulation, MLI) to decrease emissivity and radiative loading. Aluminum tape is used to seal any gaps or holes that would result in additional radiative loading reaching the inner stages.

4 K stage: The second stage of the PTC is used to cool the main cold stage, the "4 K stage." This stage consists of a large plate made of oxygen-free high-conductivity (OFHC) copper, gold-plated for improved thermal contact. This stage is also used as a thermal break for radiative and conductive loading on the sub-Kelvin stages. A similar aluminum radiation shield is used with 10 layers of MLI, and any gaps here are also covered with aluminum tape. With 0 W loading, this stage is expected to reach 2.8 K, and the typical temperature achieved in our system is 2.9 K. The DC SQUIDs are mounted on this stage (operation requires $T < 7K$), as well as readout circuits and the base of the He-10 fridge.

Sub-Kelvin stages: The He-10 fridge has two cold heads as well as an additional heat sink point at the heat exchanger between the two heads, at about 1.5 K. The heat exchanger is used as heat sink for wires running to the sub-Kelvin stages. The intermediate-cold head is attached via heat strap to the "350 mK stage," an aluminum stage used for heat sinking wires as well as additional higher-temperature testing space. The ultra-cold head is attached to the "250 mK stage", a 6 inch $\times$ 4 inch gold-plated OFHC plate used as the main cold stage for superconducting detector testing.

2.4.3 Readout system

A superconducting quantum interference device (SQUID) is a very sensitive magnetometer, with operation based on the principles of flux quantization and Josephson tunneling. A dc SQUID consists of two Josephson junctions in parallel in a superconducting loop which, when biased with an appropriate current, results in a voltage-to-flux $V - \phi$ relation that is periodic with applied flux. DC SQUIDs are typically operated in a flux-locked feedback loop, operating at an op-

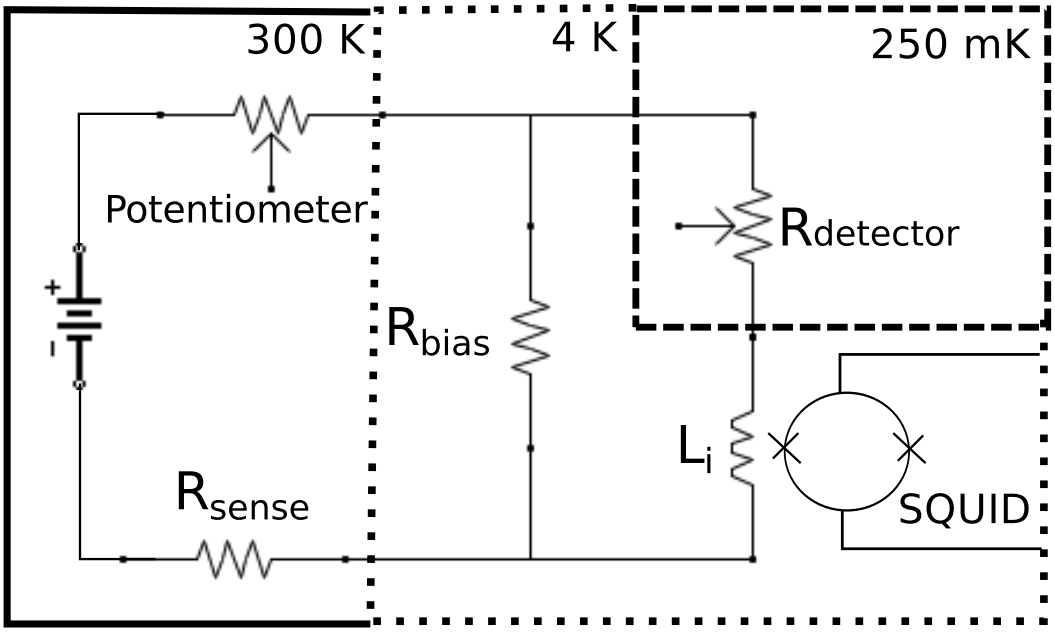

Figure 2.16: **Detector bias circuit** — Schematic of circuit to voltage bias bolometers.

timum working point located near the steepest part of the $V - \phi$ response. This linearizes the SQUID response and allows detection of very small changes in flux [31]. Commercial low-T_c dc SQUIDs were chosen for our readout system, a Quantum Design Model 5000 dc SQUID controller with four channels of Model 50 DC thin film SQUID sensors[3]. These SQUID sensors are made of a niobium/aluminum trilayer, with an operating temperature of T < 7 K, and an expected flux noise of $5\times10^{-6}\phi_0/\sqrt{\text{Hz}}$, where ϕ_0 is the magnetic flux quantum, $\phi_0 = h/2e = 2.067\times10^{-15}$ Wb.

In order to accurately measure the resistance of the TES detectors, both the voltage and current at the detector must be accurately measured. The detector current readout requires an amplifier with low input impedance (since $R_{TES} < 1\Omega$), high sensitivity, and high gain [26]. To keep readout noise sub-dominant to other noise sources, the current noise must be less than about 10 pA / $\sqrt{\text{Hz}}$.

[3]Quantum Design, Inc., 6325 Lusk Blvd., San Diego, CA 92121 USA, www.qdusa.com

SQUID amplifiers are ideal candidates. The SQUID is connected in series with the detectors to act as a sensitive ammeter, with the current proportional to a voltage read out with the room temperature SQUID controller. Superconducting NbTi wire is used for all connections from the circuit board at 4 K to the detector and the SQUID sensor, eliminating any lead resistance. TES detectors also require a voltage bias to stably operate within the narrow superconducting transition using electrothermal feedback [26]. The custom detector voltage bias circuit, shown in Figure 2.16, consists of a current-biased shunt resistor at 4 K with $R \ll R_{TES}$, in parallel with the superconducting loop containing the detector in series with the input coil to the SQUID. The current in the entire loop is determined by measuring the voltage across a precision resistor at room temperature, and from this the voltage across the detector can be accurately determined. This voltage is measured using an instrumentation amplifier (Stanford Research Systems Model SIM911)[4] and a data acquisition device (DAQ) (Labjack UE9)[5]. The SQUID controller voltage is recorded with the same DAQ.

In addition to the detector readout, additional inputs and readouts are brought into the cryostat for monitoring temperatures, controlling heaters, operating and cycling the He-10 fridge, and other purposes. Most of these were read out and controlled using off-the-shelf electronics, including many modules in a single mainframe from the SRS SIM series[6], and various dc power supplies. The He-10 fridge cycle is controlled using custom LabVIEW® programs with serial readout of temperatures from the SIM mainframe and power supplies controlled via GPIB.

Much effort was necessary to reduce noise in the readout system and the surrounding environment. SQUIDs are sensitive to electromagnetic interference (EMI), and the pulse tube cooler can be major contributor [31]. Other major electrical noise sources included environmental rf sources, the auxiliary readout and control systems, ac power mains in the building, and the vacuum system. Noise and unwanted ground connections from the vacuum system were eliminated, as

[4]Stanford Research Systems, Inc. 1290-D Reamwood Ave., Sunnyvale, CA 94098 USA. www.thinksrs.com

[5]Labjack Corporation, 3232 S Vance St STE 100, Lakewood, CO 80227 USA, www.labjack.com

[6]Stanford Research Systems

cryopumping dominated over the effectiveness of the turbomolecular pump. The cryostat could be removed from the vacuum system once it reached its base temperature. Auxiliary readout noise and interference could be temporarily eliminated during the most sensitive science measurements by disconnecting everything but the necessary signal lines. The other sources of noise were not able to be eliminated entirely, but were mitigated to the point that they were negligible. Direct EMI from the PTC motor driver was reduced by mounting the motor as far from the cryostat case as possible ($\sim 2ft$ away), as well as running the motor cable as far from other cables as possible. The readout lines were physically separated into three cables: the clean signal lines, He-10 fridge readout, and all other auxiliary readout. The signal cable runs separately from the other lines both inside and outside of the cryostat. All lines are filtered at the input to the cryostat, with pi filters (Spectrum Control 5000 pF Pi type filters)[7] inside rf sealed boxes at 300 K. All external cables were completely shielded, and sensitive signals were placed on individually shielded twisted pairs within the shielded cable. The cryostat case, both ends of all shields, and common ground signals were all kept at a common potential, and any stray ground connections and ground loops were eliminated. Additional braided shield ground straps were added between the cryostat case and the common potential as an rf ground conductor. All AC mains connected equipment (power supplies, SQUID controller, computer, etc) is served from a common power phase.

2.4.4 Thermal Performance

Pulse-tube coolers can offer very good long-term stability compared to liquid cryogens, since they can run indefinitely. However, the main drawback can be that the pulsing action also causes low frequency temperature variations near the pulse-tube frequency. Changes in temperature change the effective area of a SQUID, which with a constant background magnetic field results in a change in flux. Changing temperature also causes thermal motion of vortices that are trapped within the SQUID on cooldown. Calculations of expected noise contributions from

[7]Spectrum Control Inc., 8031 Avonia Rd., Fairview, PA 16415 USA

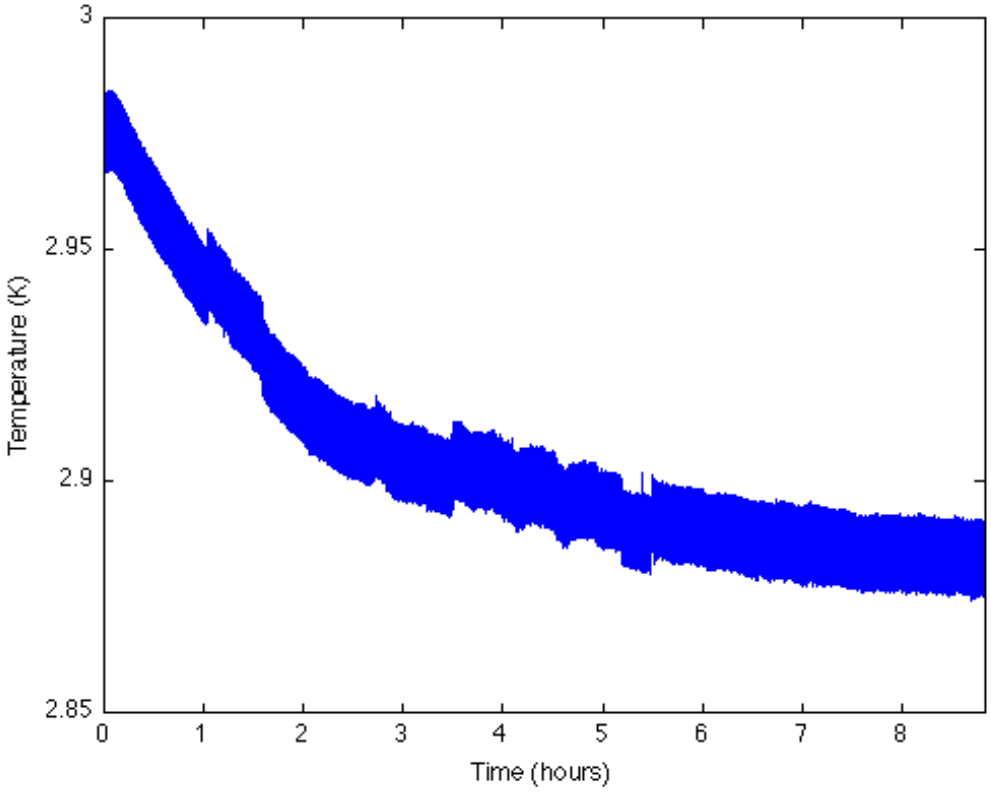

Figure 2.17: **Initial cooldown of cryostat** — Plot of temperature vs. time for the cryostat cooling down to base temperature, starting at room temperature at t=0. Temperature fluctuations are shown in detail in Figure 2.18.

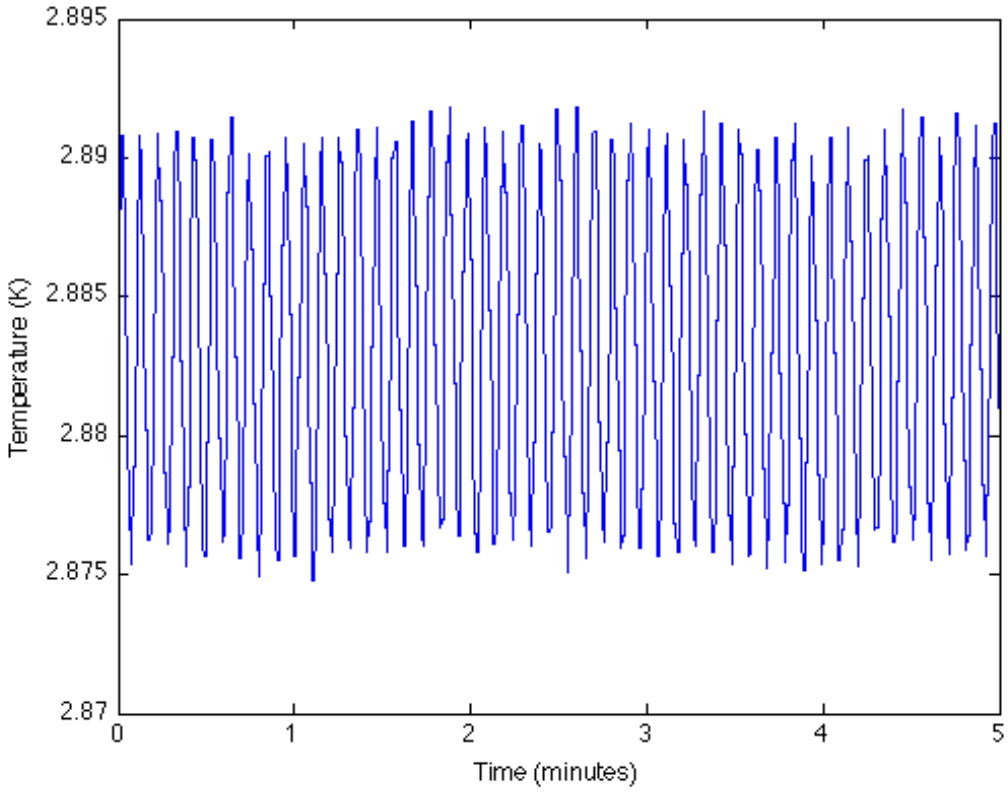

Figure 2.18: **Temperature fluctuations from PTC head** — Plot of temperature fluctuations at the 4 K stage after overall temperature stabilization, showing small-scale temperature fluctuations from the pulse-tube head.

temperature fluctuations for low-T_c dc SQUIDs near 4 K predicts fluctuations of 0.1 K to have a noise contribution of $5 \times 10^{-7}\phi_0/\sqrt{\text{Hz}}$ [43]. Additional thermal mass or thermal isolation from the cold head can mitigate fluctuations. These must be balanced with the limited thermal conductivity, which can result in long cool down times for large systems. For our system, cooling from room temperature to 4 K takes about 24-32 hours (Figure 2.17). At this point the He-10 fridge can be cycled and stable base temperatures are achieved after several hours. Temperature fluctuations from the pulse-tube cooler of 0.016 K with a period of 6 seconds are seen at the 4 K stage (Figure 2.18). These fluctuations do not affect the sub-Kelvin stage temperature, and the 250 mK stage temperature is stable to within approximately 0.001 K.

2.4.5 Noise performance

The white and 1/f noise of the SQUIDs was measured as described in the SQUID manual, and compared with the SQUID sensor specifications. With the SQUID in open loop operation, the output is a sensitive measure of noise in the system, and potential noise sources can be investigated and quantified. A spectrum analyzer (Stanford Research Systems Model SR770) was used to measure the noise spectral density of the zeroed open-loop voltage in many configurations.

Noise contributions at different frequencies were investigated. A uniaxial accelerometer (Endevco Corp. Model 2215, uniaxial accelerometer) on the outer case of the cryostat was used to investigate the spectrum of vibration peaks, to check for correlations with low frequency noise (Figure 2.19). As the accelerometer was only measuring on the outer case, it is only a relative measurement of the vibration amplitude at the cold stages, and there is always the possibility of resonances of internal structures resulting in a different vibration spectrum at the cold stages. A more thorough investigation would involve measuring vibrations directly at the cold stage. A detailed study of the vibration spectrum of a pulse-tube cooler has been done, finding vibrations up to 15 KHz [44]. Temperature fluctuations, with a low amplitude and frequency, had no significant effect on noise. At high frequencies, peaks from the pulse-width modulated motor driver of the PTC dom-

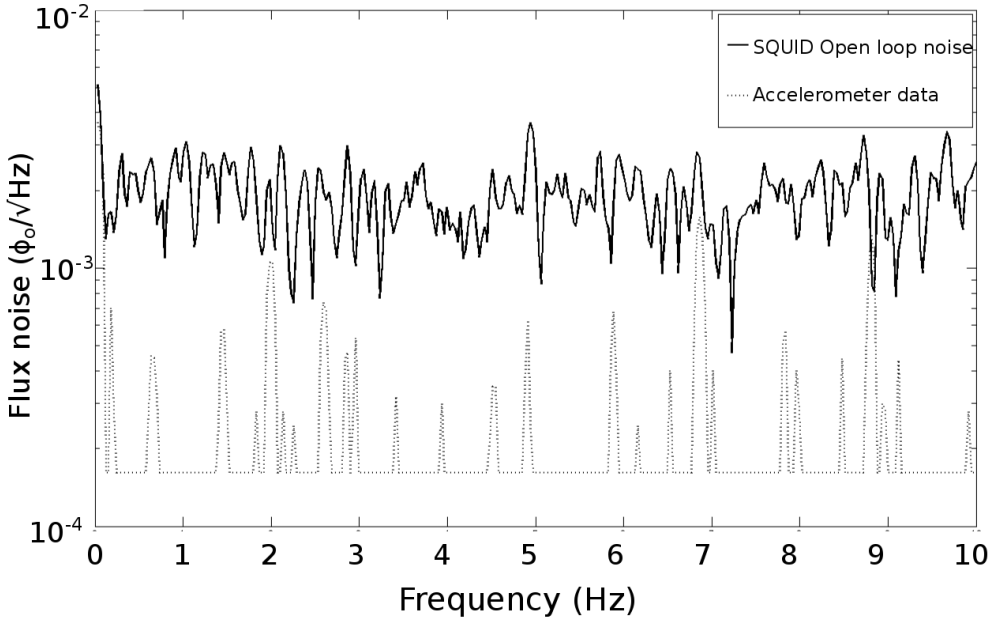

Figure 2.19: **Low frequency SQUID noise** — Low frequency voltage noise on SQUID, plotted with accelerometer spectra.

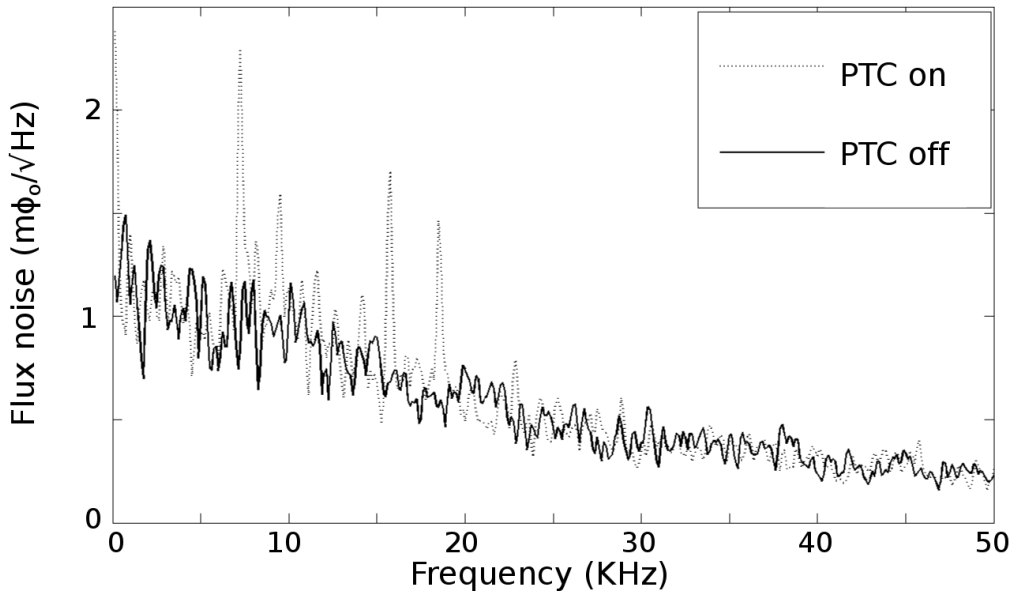

Figure 2.20: **High frequency SQUID noise** — High frequency voltage noise on SQUID, showing the peaks from the PTC's pulse-width modulated motor driver.

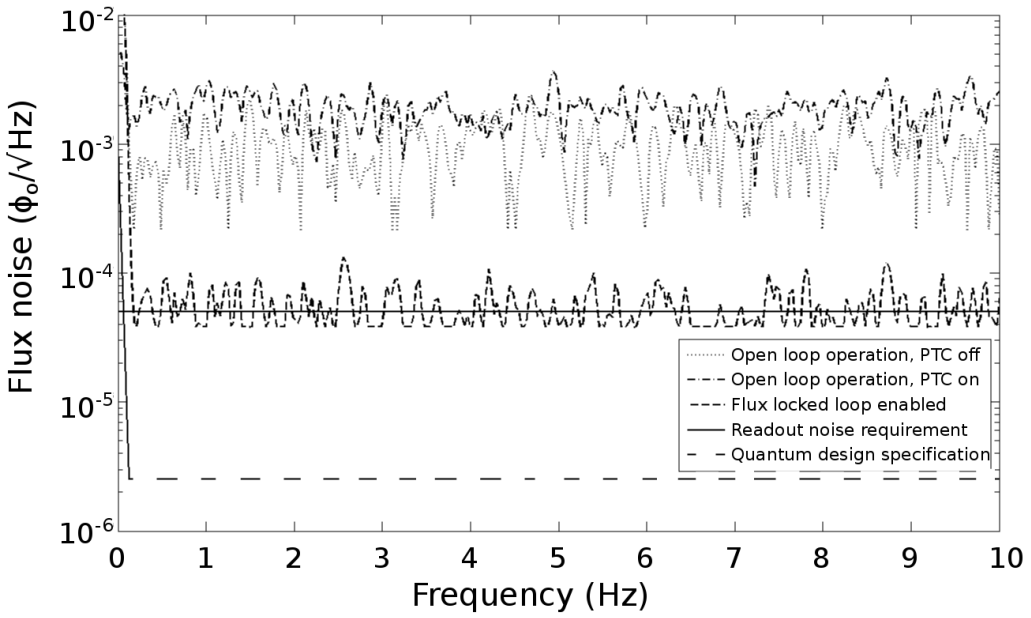

Figure 2.21: **Flux noise performance of dc SQUID** — Flux noise performance of a single squid channel, compared to Quantum Design specifications.

inate the noise (Figure 2.20). Replacing this with a linear driver made significant improvements to high frequency noise contributions, in later testing not described here.

Noise spectral densities of flux noise for a single SQUID channel are shown in Figure 2.21, comparing the baseline from Quantum Design with our achieved values. The baseline value from Quantum Design ($3 \times 10^{-6}\phi_0/\sqrt{\text{Hz}}$) is plotted. Noise peaks from the PTC are apparent at lower frequencies (black) when compared to the data taken with the PTC off. The noise floor is lowered and several peaks are eliminated in flux-locked loop operating mode. Converting the flux noise seen (up to 10 Hz) to a current noise results in a current noise of approximately 10 pA / $\sqrt{\text{Hz}}$, which just meets our readout noise requirement, based on requiring the readout noise to be subdominant to other noise sources. The 1/f knee is approximately 0.2 Hz. At higher frequencies, the noise increases to a level of approximately 100 pA / $\sqrt{\text{Hz}}$. Since this is a test cryostat for detector prototyping and not long-term science observations, these noise levels are acceptable to operate and test detectors, but we will continue to work on improvements. Since high fre-

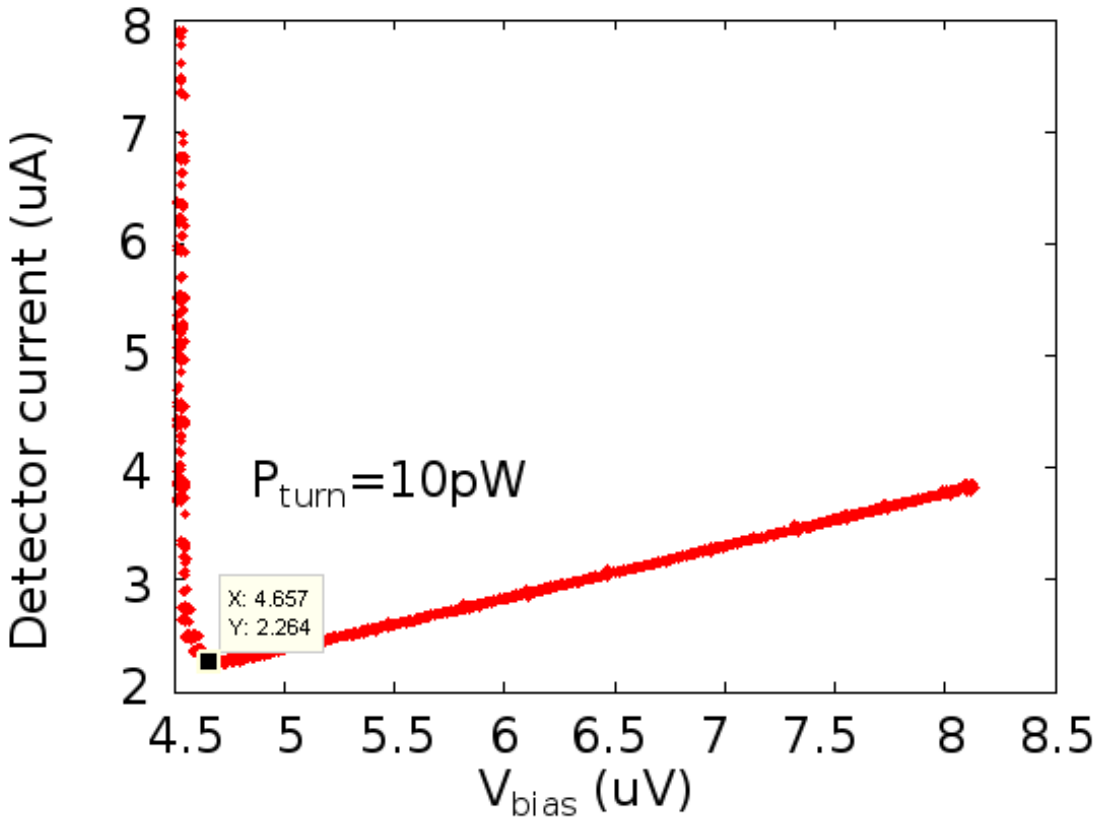

Figure 2.22: **Detector performance** — IV curve of a TES bolometer, taken at T = 300 mK.

quency noise dominates, for dc operation, further noise reduction is possible with low-pass filtering, and the noise does not affect our science results. Figure 2.22 shows a typical bolometer current-voltage (I-V) curve, with a 1 KHz Butterworth low-pass filter on the SQUID output.

2.4.6 Conclusions

The successful design and operation of a pulse-tube cooled test cryostat with low-T_c dc SQUID amplifiers was demonstrated. High frequency noise from the pulse-tube cooler, especially its pulse-width modulated motor driver, dominated the noise, but this noise can be mitigated to levels where SQUID operation and detector testing was uncompromised. Improvements can be made to increase rf shielding and reduce EMI interference from the pulse-tube cooler.

2.5 Frequency domain multiplexing readout

The system described in Section 2.4 has all the necessary cryogenic and readout systems for operating a few TES bolometers at a time, with each bolometer having dedicated readout wires and a dedicated low-T_c dc SQUID amplifier. However, the current generation of CMB instruments must operate many thousands of TES bolometers simultaneously to reach the sensitivity needed to probe the faint B-mode signal. These large focal planes are still cooled to sub-Kelvin temperatures by refrigerators similar to the sorption fridge described in Section 2.4, with typical cooling powers at base temperature of tens of microWatts. Running thousands of pairs of cryogenic wires to the cold focal plane, with a pair for each bolometer, would be result in a thermal load that is unacceptably high for any reasonable dimensions of cryogenic wire. Instead, the signals for multiple bolometers are multiplexed, running these multiple signals on a single pair of wires, as well as sharing other readout hardware. For example, with a multiplexing factor of 10, with frequency domain multiplexing there are 10$\times$ fewer wires running to the cold focal plane.

While the limitations of thermal load from wiring on the cold focal plane

is the driving reason behind multiplexed readout, there are several other important motivations to increase the multiplexing factor as much as possible. The space within a cryostat is extremely limited, and reducing the amount of wiring and components and their complexity by sharing them with multiplexing helps maximize the use of this valuable space. Cost is another important consideration, especially since high-quality, low-T_c dc SQUIDs are relatively expensive and difficult to fabricate, and other readout components like FPGAs can be expensive as well. The benefits of multiplexing must not be outweighed by detrimental effects on the noise and stable operation of the SQUIDs and bolometers.

Currently there are several different methods of multiplexed TES bolometer readout, including time-domain multiplexing [26], frequency-domain multiplexing [32], and microwave SQUID multiplexing [26]. Both time-domain multiplexing (TDM) and frequency-domain multiplexing (FDM) have been successfully deployed as TES readout on several current CMB instruments, including BICEP2 (TDM) [45], ACTPol (TDM) [46], SPTPol (FDM) [32], and POLARBEAR-1 (FDM) [39].

In this section, we give an overview of frequency-domain multiplexing, specifically the frequency-domain multiplexing readout system (fMUX) which is used in both POLARBEAR-1 and POLARBEAR-2, and is described in detail in Reference [32]. Section 3.4.2 has more details on recent developments to increase the multiplexing factor for POLARBEAR-2.

Frequency-domain multiplexing takes advantage of the relatively large bandwidth of the SQUID amplifier compared to the small bandwidth of CMB signal incident on a TES bolometer. The frequency response can be described using the bandwidth or the time constant τ, which is the inverse of the bandwidth, $\tau = 1/2\pi f_{3dB}$. The SQUID bandwidth is on the order of $\sim MHz$, while the CMB signals for a telescope scanning across the sky are relatively slow (narrow bandwidth). Even with signal modulation at a few Hz (for example, a spinning half-wave plate) the science signal bandwidth would still be $< 100Hz$. The optical time constant must be short enough that it can resolve the signal as the telescope scans across the sky. If the time constant were too slow, the optical beam would

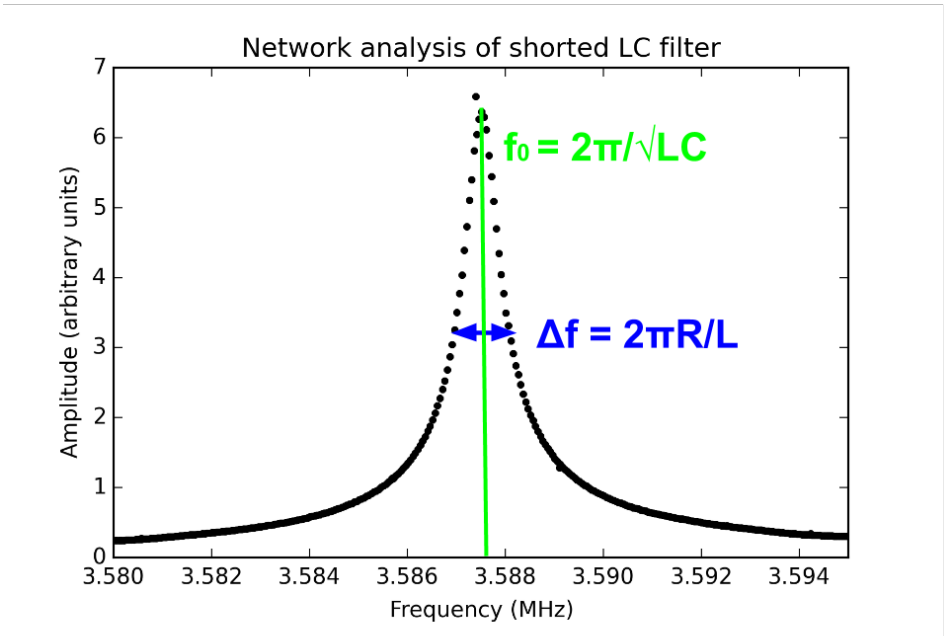

Figure 2.23: **Frequency response of series RLC resonant peak** — The frequency response of a series RLC resonant peak is shown, with the center frequency f_0 labeled in green, and the bandwidth Δf labeled in blue. The shape of the peak is described by Equation 2.28

be elongated and the telescope's resolution degraded [47].

The readout bandwidth must also be broader than the detector's inherent bandwidth for stable operation under feedback, meeting the criterion $\tau_{TES} > 5.8\tau_{readout}$. The detector time constant is set by the bolometer's thermal time constant τ_{TES} and the loop gain $\mathcal{L}$, as discussed in Section 2.2. In the fMUX system, the electrical bandwidth is set by a resonant series RLC circuit, with the bolometer R_{TES} acting as the resistor.

A channel's center frequency f_0 is set by the capacitance and and inductance values, as shown in Equation 2.25 and Figure 2.23. The bandwidth Δf at full-width half-max for a resonant series LCR circuit is set by the inductance L and the resistance R_{TES}, as shown in Equation 2.26, and as shown in Figure 2.23, and $\tau_{readout}$ is given in Equation 2.27. The curve in Figure 2.23 is given by the power distribution in Equation 2.28, which reduces to $P_{avg} = V_{rms}^2/R$ at f_0:

$$f_0 = \frac{2\pi}{\sqrt{LC}} \, , \tag{2.25}$$

$$\Delta f = 2\pi R/L \, , \tag{2.26}$$

$$\tau_{readout} = \frac{2\pi L}{R_{TES}} \, , \tag{2.27}$$

$$P_{avg}(f) = \frac{V_{rms}^2 R(2\pi f)^2}{R^2(2\pi f)^2 + L^2((2\pi f)^2 - (2\pi f_0)^2)^2} \, . \tag{2.28}$$

Many of these channels can be placed within the SQUID readout bandwidth, and each bolometer channel can be operated almost completely independently, by setting its bias power and reading out its sky signals within its defined band. With careful design and implementation, there is no degradation of the individual bolometer performance by multiplexing them in this way. To keep a constant readout bandwidth, the inductance of each channel is constant, and the capacitance is varied to set the channel frequency. In current implementations of the fMUX system, there is a comfortable margin designed between the necessary optical time constant, the detector time constant, and the readout time constant.

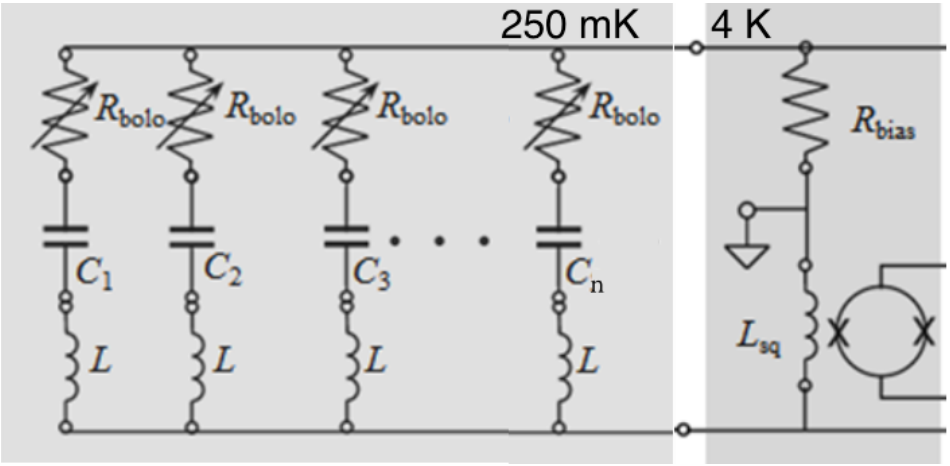

Figure 2.24: **Circuit diagram of cold portion of frequency-domain multiplexing readout system** — A circuit diagram of only the cold portion of the frequency-domain multiplexing readout system is shown, with the SQUID at far right, and the channel-defining LC filters and TES bolometers shown as variable resistors at left. The nominal stage temperatures of the location of the two parts of the circuit are labeled.

The spacing of the channels in a frequency comb must be large enough so that the off-resonance current from neighboring channels does not spoil the voltage bias on-resonance, and so that crosstalk between neighboring channels is small (discussed below in Section 2.5.3). Another consideration is that the spacing also must be large enough so that the Johnson-Nyquist noise contributions from neighboring channels are small. At the spacings dictated by the first two conditions, this is typically a $< 1\%$ increase in the Johnson-Nyquist current noise on a detector.

2.5.1 Cold components

The circuit that contains the channel-defining LC filters and bolometers is relatively simple, as shown in Figure 2.24. This is similar to the readout circuit used for a single bolometer in Figure 2.16, with the bolometer portion expanded with multiple channels and LC filters. The set of n multiplexed bolometers will be referred to here as a "comb." The frequency response of a comb of eight bolometers with LC filters is shown in Figure 2.25. This type of network analysis sweep of

the frequency response is used to determine the peak locations, f_0, so that these values can be used to determine the frequency of the sinusoidal voltage bias for each bolometer. The bias frequency is much faster than the bolometer thermal response, so the bolometer sees a constant electrical bias power.

A bias resistor for each comb is located at 4 Kelvin, in series with the SQUID and in parallel with the bolometer LCR circuit, with $R_{bias} << R_{TES}$. This bias resistor, in combination with a current source and precision current-sensing resistor, creates a stiff voltage bias to the $\sim 1\ \Omega$ bolometers, so that their voltage bias V_{bias} is known, in the same way as described in Section 2.4.3. This resistor is located at 4 Kelvin so that the voltage bias can be supplied by a single pair of wires to the subKelvin focal plane for each comb of bolometers. These bias resistors dissipate a small amount of power, which is well below the cooling power of the 4 Kelvin stage. The bias resistor does contribute Johnson noise which increases with the temperature of the resistor, but this is very small (see Section 2.5.4). Locating this resistor at a colder stage would result in additional thermal loading from additional wires and the dissipated electrical power, which are undesirable since the cold stages have such limited cooling power.

A current-biased series array of dc SQUIDs (referred to here as a "SQUID") is used to read out a comb of n channels, and this SQUID is located at the nominal 4 Kelvin stage. The current from the bolometers is summed at the SQUID, which has a modulated output dependent on the current through the bolometers. The SQUID output is linearized through negative feedback, as described in Section 2.3.2. The SQUID still has a limited dynamic range, and so the voltage bias input, which is a sum of sinusoidal voltages at each bolometer bias frequency, is nulled by sending in its inverse, to cancel out its contribution to current through the SQUID.

The operation of the resonant series RLC circuit depends on there being negligible impedance outside of the well-defined components of the circuit. The bolometer resistance R_{TES} must be the dominant resistance within this series circuit, and there also must be minimal stray inductance from wiring and circuit boards. The effect of this stray impedance is quantified in Section 2.5.3. The inductors and capacitors must have low loss, to maintain low impedance of

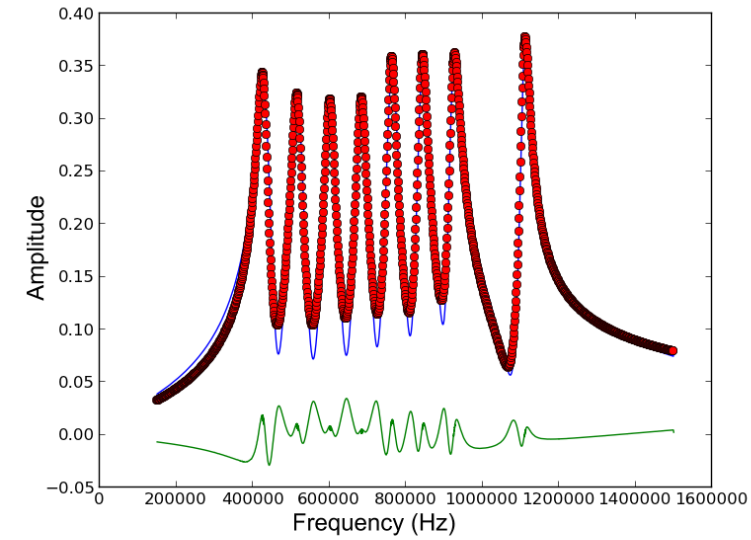

Figure 2.25: **Frequency response of a comb of eight TES bolometers with channel-defining LC filters.** — The frequency response of a comb of eight TES bolometers with channel-defining LC filters is shown, with the data in blue, the model fit in red points, and the residuals in green.

these elements across the readout bandwidth. These components and wiring are all at sub-Kelvin temperatures, which helps to achieve these specifications. All wiring within the series circuit is superconducting NbTi, high purity copper (with residual-resistivity ratio RRR $>$ 100), or tin-lead covered copper, and contact resistance of connectors is kept to a minimum. The stray inductance is kept to a minimum by the use of broadside-coupled striplines for the only relatively long length of cable, which runs from the SQUID and bias resistor at the 4 Kelvin stage to the LC circuit at the cold focal plane.

The equivalent series resistance (ESR) of the LC filters and any stray resistance from wiring and connections can be determined by measuring the width of the resonant peak of shorted filters, just as described in Equation 2.26. The resistance R_{ESR} is measured instead of R_{TES} by either electrically shorting the filters, or by allowing the TES bolometers to drop completely through their transition to

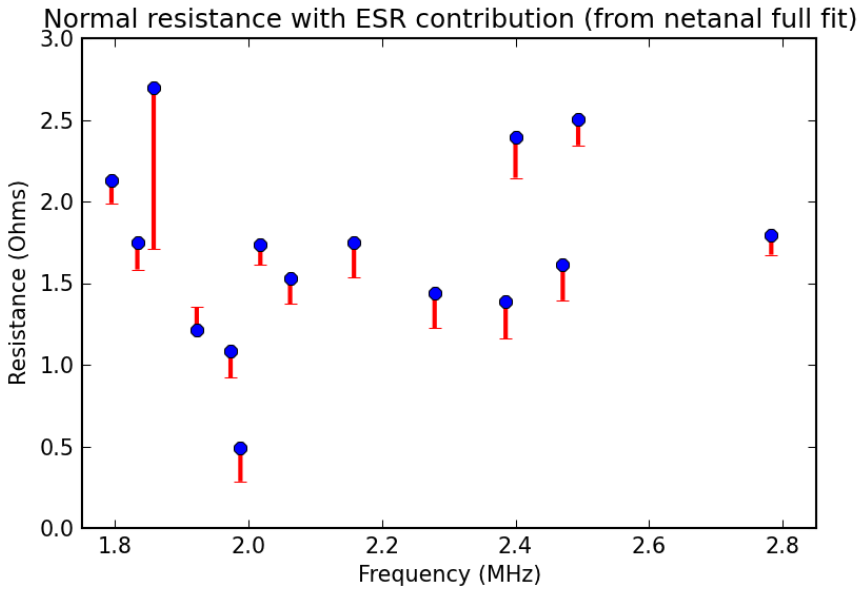

Figure 2.26: **Measured resistance of bolometers with contribution from ESR)** — The measured bolometer resistance R_{TES} is shown as a dot along with the measured ESR contribution shown as a dash (measured with bolometers superconducting with $R_{TES} = 0$)

superconducting, so that $R_{TES} = 0$. An example of measuring the resistance R_{TES} and R_{ESR} for the same comb is shown in Figure 2.26.

2.5.2 Warm electronics

To control and read out the cold circuit described in the previous section, the fMUX readout system uses custom warm electronics designed by collaborators at McGill University. These custom warm electronics are described in detail in References [32], [48], [49].

The far left side of Figure 2.27 represents the custom electronics that synthesize the bolometer voltage biases (labeled "Carrier Bias Comb"), the nulling signal that is applied to the SQUID to increase its dynamic range (labeled "Nulling Comb"), and the demodulators. The carrier bias comb are sine-wave generators creating the sinusoidal voltages bias for each bolometer channel frequency, and which are summed together and applied to the bias resistor and bolometer comb.

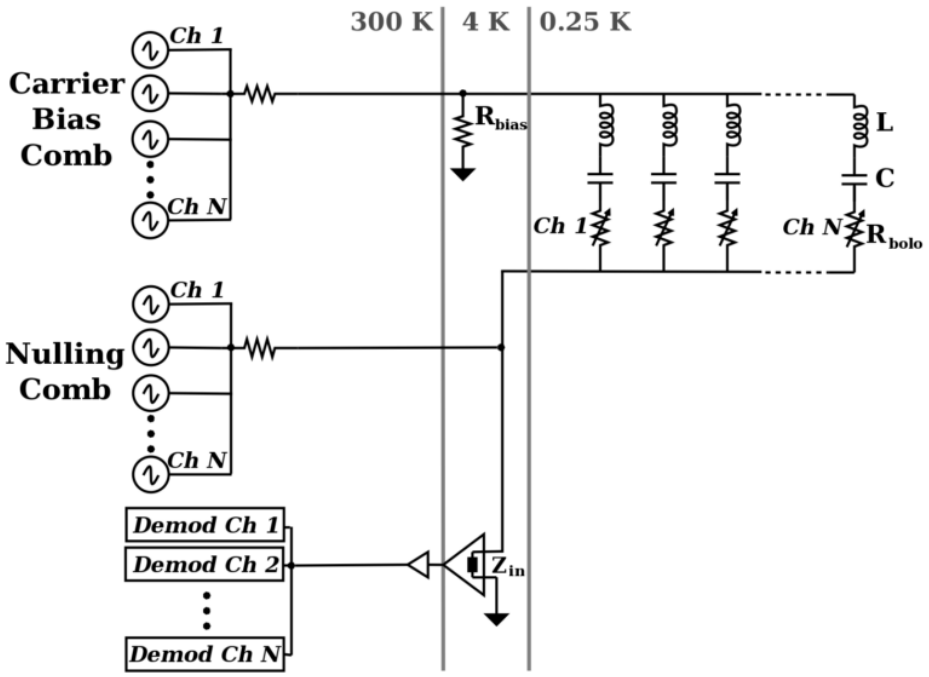

Figure 2.27: **Simplified schematic of fMUX readout system** — The overall fMUX readout for a single comb of bolometers is shown in a simplified schematic, with the sections labeled by the nominal temperature stage where they are located. The cold sections are the same as in Figure 2.24. (Figure from Dobbs et. al 2012)

Since the SQUID has a limited dynamic range, the nulling comb, which is the inverse of the carrier bias comb, is also applied to the SQUID. This decreases the dynamic range of the signal by removing the component at the carrier frequency, which contains no astrophysical signal. Scanning the sky produces a changing optical power that results in a modulation of the resistance of the TES bolometer. This results in amplitude modulation of the carrier current. These bolometer currents are all summed and input to the SQUID, which outputs a voltage that is the modulated sum of the signals on all the bolometers for a comb.

The SQUID, as described in the previous section and in Section 2.3, has a transimpedance that is high enough to convert small current through the bolometers into a voltage that can be read out with a room-temperature amplifier. This is shown in Figure 2.27 as the amplifier at 4 Kelvin (the SQUID) and the amplifier at 300 Kelvin. For POLARBEAR-1 and first-generation fMUX readout CMB instruments, the SQUID feedback was broadband feedback, achieved through the shunt-feedback configuration described in Section 2.3 and Reference [32], with a feedback resistor creating a flux-locked loop. The first-stage amplifier for the SQUID output voltage is at room-temperature outside of the cryostat, but must be as close to the SQUID as possible with minimal wiring lengths ($\leq 20cm$) to keep the transmission delay within the feedback loop small. This cryogenic wiring also has a hard limit for its minimum length since it is connected to several temperature stages and must not have an excessive thermal load.

For the shunt-feedback configuration, which provided negative feedback over the entire bandwidth, the SQUID bandwidth was limited to $\sim$ 1.3 MHz, due to the difficulty maintaining stability across a large bandwidth. For frequency channels with the necessary bandwidth and frequency spacing, this limited the multiplexing factor to about $10\times$. To extend the usable bandwidth, the feedback was changed to a form of baseband feedback known as Digital Active Nulling (DAN), described in Reference [48], where feedback is applied only around the bolometer carrier frequencies. The signal from the SQUID is measured and used to determine the feedback to apply. The amplified SQUID output is sent to a bank of analog demodulators, with one for each TES, that mixes the signal down

to baseband.

2.5.3 Sources of crosstalk

A multiplexed readout system can create many kinds of electrical crosstalk, where signals from one detector have an effect on the signals for another detector. This can have a range of effects, depending on the source of the crosstalk, including excess signal on a detector (referred to here as signal crosstalk) and excess noise on a detector. Crosstalk can also be created in the optical system, with imperfect optics causing stray reflections of the optical signal. The overall specification for electrical crosstalk is that it is small compared to optical crosstalk, which is expected to be about one percent. Electrical signal crosstalk can cause systematic effects that degrade the scientific data from the instrument, but the layout of the system can be designed to minimize or mitigate these effects. For example, for a dual-polarization experiment like POLARBEAR, where each detector is sensitive to a single polarization, signal crosstalk that leaks from one polarization to the other causes the bright unpolarized signal to turn into a spurious polarization signal.

In the fMUX system, signal crosstalk onto a detector can only occur if the crosstalk signal lies within its frequency bandwidth. There is a small amount of crosstalk from its nearest neighbors in frequency space and physical space in the comb, quantified below, and there is also the possibility of crosstalk from another comb if there is a source of crosstalk (for example, through inductive coupling of cables) and the detector frequency bands overlap. The physical layout of pixels and LC channels and the layout of channels into combs and frequency channels can be arranged to make sure no detectors are neighbors or share a pixel in both physical space and frequency space.

There are three potential forms of electrical signal crosstalk within a multiplexed comb of detectors. The first is bias carrier leakage, which results in the off-resonance current from adjacent channels in frequency space to crosstalk onto a channel. The current I at the detector's carrier frequency ω_i from neighboring channels $Ch\,i \pm 1$, with voltage bias $V_{bias}^{\omega_i}$ and LCR_{TES} parameters, is given in Equation 2.29 [32]:

$$I^{\omega_i}_{Chi\pm1} = \frac{V^{\omega_i}_{bias}}{R_{TES} + j\omega_i L + 1/(j\omega_i C_{Ch\,i\pm1})} \simeq \frac{V^{\omega_i}_{bias}}{2j\Delta\omega L}(1 + \frac{jR_{TES}}{2\Delta\omega L}) \ . \tag{2.29}$$

This results in the current modulation from neighboring channels shown in Equation 2.30, which can be compared with the current modulation on-resonance in Equation 2.31 [32]:

$$\frac{\Delta I^{\omega_i}_{Ch\,i\pm1}}{\Delta R_{TES}} \simeq \frac{V^{\omega_i}_{bias}}{2\Delta\omega L} \ , \tag{2.30}$$

$$\frac{\Delta I^{\omega_i}_{Ch\,i}}{\Delta R_{TES}} \simeq \frac{-V^{\omega_i}_{bias}}{R^2_{TES}} \ . \tag{2.31}$$

The magnitude of the ratio of these two modulations, $|R^2_{TES}/(2\Delta\omega L)^2|$, is the approximate level of crosstalk. For POLARBEAR-1's readout parameters, this results in $\sim 0.25\%$ crosstalk. For POLARBEAR-2's readout parameters, the channel spacing $\Delta\omega$ is smaller, and the bolometer resistance R_{TES} is slightly higher, but the inductance L is also significantly higher, so this crosstalk is expected to be at a similar level.

Another source of signal crosstalk is due to the non-zero impedance of the wiring from the SQUID at 4 Kelvin to the LCR comb on the 250 mK focal plane. The input coil of the SQUID also has a non-zero impedance which must be included in this series circuit. These stray impedances within the bolometer bias Z_{stray} cause a non-ideal voltage bias across a detector channel, with some voltage drop across these stray impedances. The stray impedances are dominated by stray inductances, L_{stray}.

The change in voltage bias across the bolometer V_{bias} and the stray bias V_{stray} from a current modulation on the on-resonance channel, $dI^{\omega_i}_{Chi\pm1}$, is given in Equation 2.32, where dV_{module} is the total voltage across the input of the cold circuit, and with a constant voltage bias, dV_{bias} is zero [32]:

$$dV_{module} = dV_{bias} - dV_{stray} = -dV_{stray} \simeq dI^{\omega_i}_{Ch\,i} j\omega_i L_{stray} \ . \tag{2.32}$$

This voltage induces a current $dI^{\omega_i}_{Ch\,i\pm1}$ in the neighboring bolometer channels, given in Equation 2.33 [32]:

$$dI^{\omega_i}_{Ch\,i\pm1} = \frac{dV_{module}}{Z^{LCR}_{Ch\,i\pm1}} \simeq \frac{-dI^{\omega_i}_{Ch\,i} j\omega_i L_{stray}}{j2\Delta\omega L} \ . \tag{2.33}$$

The ratio of the power fluctuations induced in the neighboring channels to the power induced in the on-resonance channel (from the sky signal incident on the on-resonance channel) is the magnitude of this form of crosstalk, and is given in Equation 2.34:

$$\frac{dP^{\omega_i}_{Ch\,i\pm1}}{dP^{\omega_i}_{Ch\,i}} \simeq -\frac{I^{\omega_i}_{Ch\,i\pm1}}{I^{\omega_i}_{Ch\,i}} \frac{\omega_i}{\Delta\omega} \frac{L_{stray}}{L} \ . \tag{2.34}$$

For the POLARBEAR-1 fMUX system parameters, this is approximately 0.3%. POLARBEAR-2 has smaller channel spacing $\Delta\omega$ and much higher frequencies ω, with a higher inductance L, so there was a much tighter constraint on L_{stray} to keep this kind of crosstalk at an acceptable level. This motivated the development of the NbTi striplines described in Section 3.4.2.4.

The inductors within a comb are placed onto the same circuit board, possibly fabricated and physically located on the same monolithic chip of silicon. There is some mutual inductance $M_{i,j}$ between inductors that are physical neighbors. This mutual inductance between the two inductors L_i and L_j for channels i and j is characterized by a coupling coefficient $k_{i,j}$, $M_{i,j} = k_{i,j} L_i L_j$. The current for the i^{th} channel induces a voltage $|V_j| = \omega_i M_{i,j} I_i$ in the inductor for the j^{th} channel. This form of crosstalk can be minimized by keeping the maximum coupling coefficient very low ($k \sim 0.01$ for POLARBEAR-1), and physically separating channels that are neighbors in frequency space.

Crosstalk can also induce additional loading on the SQUIDs and noise in the system. For the DAN feedback implementation, the feedback provided to the SQUID depends on the measured signal at the analog-to-digital converter, which goes to the digital demodulators. However, the desired feedback is on the signal present at the SQUID output. Crosstalk within the electronics or cabling between these two points will cause imperfect feedback and nulling at the SQUID, degrading its performance. The development of cables with minimal crosstalk for this purpose is described in Section 3.4.2.5.

2.5.4 Sources of readout noise

The contribution to readout noise $NEP_{readout}$ from the SQUID has already been discussed in Section 2.3.3, including the SQUID current noise and the noise contribution from the room-temperature voltage amplifier for the SQUID.

An additional noise contribution in the fMUX readout system is from Johnson-Nyquist noise on the bias resistor at 4 Kelvin. Unlike the Johnson-Nyquist noise from the bolometer, this is not suppressed by feedback. The current noise $NEI_{Johnson,bias}$ contributes to $NEI_{readout}$, and is calculated using Equation 2.35, where R_{loop} is the total resistance in series:

$$NEI_{Johnson,bias} = \frac{1}{R_{loop}}\sqrt{4k_BTR}\,. \tag{2.35}$$

These three sources of readout noise are the majority of the measured $NEI_{readout}$. There are also small contributions from the Johnson noise of resistors in the room temperature electronics, the DAC generating the carrier voltages, and other non-ideal parts of the system. For the fMUX system, the total $NEI_{readout}$ is expected to be ~ 7 pA/$\sqrt{\text{Hz}}$. For POLARBEAR-1, the measured $NEI_{readout}$ was slightly higher, ~ 9 pA/$\sqrt{\text{Hz}}$.

2.6 Expected noise contributions

The total noise equivalent power NEP consists of several uncorrelated terms that can be calculated individually, and which add in quadrature, as shown in Equation 2.36 [26]:

$$NEP^2 = NEP_\gamma^2 + NEP_G^2 + NEP_{Johnson}^2 + NEP_{readout}^2 + NEP_{excess}^2\,. \tag{2.36}$$

In Section 2.2.2, we discussed the thermal carrier noise contribution, NEP_G, and the Johnson-Nyquist noise from the bolometer resistance, $NEP_{Johnson}$. In Section 2.3.3, we discussed SQUID noise and its contribution to readout noise, $NEP_{readout}$, and in Section 2.5.4 we discussed additional contributions to $NEP_{readout}$ for the fMUX readout system. The final term NEP_{excess} is used to quantify any

noise beyond the relatively well-understood contributions from the other noise terms. For ground-based instruments, atmospheric fluctuations are one source of noise beyond those discussed here (see for example [50]). The remaining noise term, NEP_γ, is the photon noise, which is the dominant noise source for a well-designed microwave detector. After deriving the expected NEP_γ, the other noise sources can be re-framed in terms of NEP_γ to compare their relative contributions.

Photon noise is caused by fluctuations in incident radiative power, and is dependent on the magnitude of incident power P_{opt}. This includes all sources of radiative power, including the CMB, the atmosphere, and internal loading from the instrument and its optics. For a detector within an optical system which limits the beam to an area A and a solid angle Ω, with an overall optical efficiency $\eta(\nu)$, where ν is the frequency, the power incident on the detector from a blackbody source is given in Equation 2.37 [27], where $B_\nu(\nu, T)$ is the Planck spectral brightness given in Equation 2.38:

$$P_{opt} = \int_0^\infty P_\nu d\nu = \int_0^\infty A\Omega\eta(\nu)B(\nu,T)d\nu \ , \tag{2.37}$$

$$B(\nu,T) = \frac{h\nu^3}{c^2 e^{h\nu/k_BT} - 1} \ . \tag{2.38}$$

For a single-moded detector, where the throughput $A\Omega = \lambda^2$, this is given in Equation 2.40, which is simplified using the definition of the Boltzmann occupation number n_{occ}, given in Equation 2.39. The expression for P_{opt} can be approximated for a detector with an average optical efficiency η with a narrow bandwidth $\delta\nu$ given by $\int_0^\infty \eta(\nu)d\nu$, which is centered around ν_0, and this expression is given in Equation 2.41.:

$$n_{occ} = \frac{1}{e^{h\nu/k_BT} - 1} \ , \tag{2.39}$$

$$P_{opt} = \int_0^\infty \eta(\nu)P_\nu d\nu = \int_0^\infty \eta(\nu)\frac{h\nu d\nu}{e^{h\nu/k_BT} - 1} = \int_0^\infty \eta(\nu)n_{occ}h\nu d\nu \ , \tag{2.40}$$

$$P_{opt} \approx \eta h\nu_0 \Delta\nu n_{occ} \ . \tag{2.41}$$

The fluctuations in this radiative power incident on a detector over a time period τ is given in Equation 2.42 [51]:

$$\sigma^2 = \frac{1}{\tau}\int (h\nu)^2 \eta n_{occ}(1+\eta n_{occ})d\nu \ . \tag{2.42}$$

The photon occupation number n_{occ} given in Equation 2.39 depends on the frequency and temperature of the source. For $n_{occ} \ll 1$, which is the case for optical wavelengths, these fluctuations follow Poisson statistics, $\sigma \sim \sqrt{N}$, where N is the number of photons received. For $n_{occ} >> 1$, which is the case for radio wavelengths where $h\nu << k_B T$, photon bunching becomes significant, and the fluctuations are instead $\sigma \sim N$. Observing at microwave frequencies, detectors are near the boundary where n_{occ} 1.

Equation 2.42 can be converted to NEP using $\bar{\sigma^2} = |NEP|^2/2$, which is given in Equation 2.43, and simplified using Equation 2.41, and so NEP_γ is given in Equation 2.44 [29]:

$$NEP_\gamma = \sqrt{2\int (h\nu)^2 \eta n_{occ}(1+\eta n_{occ})d\nu} \ , \tag{2.43}$$

$$NEP_\gamma \approx \sqrt{2}\sqrt{h\nu_0 P_{opt} + \frac{P_{opt}^2}{\Delta\nu}} \ . \tag{2.44}$$

The source's Rayleigh-Jean temperature, T_{RJ}, is defined in Equation 2.45, which converges to the blackbody temperature in the Rayleigh-Jeans limit where $h\nu << k_B T$:

$$T_{RJ} \equiv T \times \frac{h\nu/k_B T}{e^{h\nu/k_B T} - 1} \ . \tag{2.45}$$

The emission spectrum for a source with temperature T_{RJ} is given in Equation 2.46:

$$P_{opt} = \eta \Delta\nu k_B T_{RJ} \ . \tag{2.46}$$

Equation 2.46 gives the incident optical power P_{opt} for a source with temperature T_{RJ} and approximate bandwidth $\Delta\nu$, which is an important term for designing detectors as well as determining noise contributions from different sources.

Table 2.1: Contributions to NEP

Source	Equation
NEP_{γ}	$\sqrt{2\int (h\nu)^2 \eta n_{occ}(1+\eta n_{occ}) d\nu}$
$NEP_{Johnson}$	$\frac{\mathcal{L}+1}{\mathcal{L}^2}\sqrt{4k_B T_c P_{bias}}$
$NEP_{Readout}$	$V_{bias}\frac{\mathcal{L}+1}{\mathcal{L}} \cdot NEI_{readout}$
NEP_G	$\sqrt{4k_B P_{bath} T_{bath}}\sqrt{\frac{(n+1)^2}{2n+3}\frac{((T_c/T_b)^{2n+3}-1}{((T_c/T_b)^{n+1}-1)^2}}$

For a ground-based experiment, the dominant source of optical power P_{opt} is the atmosphere, which also has varying effective temperature and optical loading. To enable observations through a range of atmospheric conditions with an average $\overline{P_{opt}}$, P_{bath} (as described in Section 2.2.1) is typically designed to be $\sim 2\overline{P_{opt}}$. This results in $P_{bias} \sim P_{opt}$ for typical observing conditions.

A summary of the noise contributions is shown in Table 2.1. With careful design and optimization, the noise levels of $NEP_{readout}$, NEP_G, and $NEP_{Johnson}$ can be minimized and kept small compared to the photon noise NEP_{γ}. Therefore, a well designed instrument can have a noise level that is set by the incident radiative power. To improve the sensitivity of the instrument, the number of detectors must be increased.

The NEP is useful for characterizing and comparing the noise contributions from different sources, but the overall sensitivity of the instrument is characterized in terms of the NET_{CMB}, which is the change in CMB temperature that can be measured with a signal-to-noise of one with one second of integration, given in Equation 2.47:

$$NET_{CMB} = \frac{1}{\sqrt{2}}\frac{NEP}{dP/dT} \, . \tag{2.47}$$

The optical power P_{opt} was given in Equation 2.41, and using that to solve for dP_{opt}/dT_{CMB} is given in Equation 2.48:

$$\frac{dP}{dT} = \eta \Delta\nu k_B (h\nu/k_B T)^2 n_{occ}^2 e^{h\nu/k_b T} \ . \tag{2.48}$$

For sources in the Rayleigh-Jeans limit where P_{opt} simplifies to Equation 2.46, this NET_{RJ} is given in Equation 2.49. For the specific case of the CMB, a blackbody source with $T_{CMB} = 2.725$ K and ν_c =150 GHz, Equation 2.48 and Equation 2.47 can be combined with these specific values to determine NET_{CMB}, which is given in Equation 2.50:

$$NET_{RJ} = \frac{NEP}{2\sqrt{2} \cdot k_B \eta \Delta\nu} \ , \tag{2.49}$$

$$NET_{CMB} = \frac{NEP}{0.576\sqrt{2} \cdot k_B \eta \Delta\nu} \ . \tag{2.50}$$

From Equation 2.50, we can see that the sensitivity increases for an instrument with a wider bandwidth $\Delta\nu$ and a higher optical efficiency η.

2.7 Acknowledgements

Chapter 2, Section 4 is a reprint of material as it appears in: D. Barron, M. Atlas, B. Keating, R. Quillin, N. Stebor, B. Wilson, Performance of a 4 Kelvin pulse-tube cooled cryostat with dc SQUID amplifiers for bolometric detector testing, published in the 17th International Cryocooler Conference Proceedings, 2012. arxiv:1301.0860. The dissertation author was the primary author of this paper.

Chapter 3

The POLARBEAR experiment

3.1 Introduction

The POLARBEAR experiment is measuring fluctuations in the polarization of the cosmic microwave background (CMB), with the goal of characterizing the gravitational lensing signal at small angular scales, as well as the signal from inflationary gravitational waves at large angular scales, as described in Chapter 1. The POLARBEAR experiment is located at the Ax Observatory on Cerro Toco, at an altitude of 5200 meters in the Atacama desert of Chile. The POLARBEAR-1 receiver [39, 52, 53], described in Section 3.2, started observations in 2012, installed on the Huan Tran Telescope (HTT). The first gravitational lensing results from POLARBEAR-1 were recently published [54, 55, 56], and these results are described in Section 3.3. The POLARBEAR-2 receiver, described in Section 3.4, is preparing to deploy in 2016 alongside POLARBEAR-1. The Simons Array expansion, described in Section 4.3, will add two additional telescopes, identical to HTT, which are currently under construction.

3.2 POLARBEAR-1 Overview

The POLARBEAR-1 Cosmic Microwave Background (CMB) polarization experiment has been observing since early 2012 from its 5200 meter site in the Atacama Desert in Northern Chile. POLARBEAR-1's measurements are character-

izing the CMB polarization due to gravitational lensing by large scale structure, and searching for the possible B-mode polarization signature of inflationary gravitational waves. POLARBEAR-1's 250 mK focal plane detector array consists of 1,274 polarization-sensitive antenna-coupled bolometers, each with an associated lithographed band-defining filter and contacting dielectric lenslet, an architecture unique in current CMB experiments.

3.2.1 POLARBEAR-1 Scientific Motivation

From its discovery to the present, a series of more detailed measurements of the cosmic microwave background, including its primary temperature anisotropy and E-mode (curl-free) polarization, have helped refine our models of the universe, as described in Chapter 1. Many current CMB experiments, including POLARBEAR-1, are focused on characterizing the B-mode (divergence-free) polarization component of the CMB.

At large angular scales, B-mode polarization is predicted to have been generated by primordial gravitational wave tensor perturbations during inflation [57], as described in Section 1.2.3. The strength of these tensor perturbations is dependent on the shape of the inflationary potential as well as the energy scale of inflation, but it is expected to peak on an angular scale of 2 degrees. Detection of this B-mode polarization would be direct evidence supporting the inflationary paradigm, and would help to constrain the parameter space of inflationary models [58].

Although tensor perturbations from inflation are the only primordial source of B-mode polarization in most cosmological models, B-modes are also created at later times by weak gravitational lensing of the CMB by large scale structure, as described in Section 1.2.4. This lensing mixes E and B-modes, creating B-mode polarization that has recently been measured on small angular scales [59, 56, 60, 15, 61]. Lensing B-modes can give information about the large scale structure that generated them, as the lensing effect is sensitive to the formation of structure at early epochs. POLARBEAR-1's observation fields overlap with optical and infrared galaxy surveys, and cross-correlation with these data sets will leverage their redshift

information for a more complete picture of the lensing effect.

3.2.2 Instrument Overview

Reaching the sensitivity necessary to measure the CMB's B-mode polarization requires significant advances in detector technology. POLARBEAR-1 uses a unique 637 pixel lenslet-coupled focal plane, integrated with a large field of view telescope and cold reimaging optics, and observing in a spectral band centered at 148 GHz, with a width of 38 GHz. This section gives a brief overview of the instrument. The design and development of the POLARBEAR-1 experiment have been described in detail in previous proceedings [39, 52, 62].

POLARBEAR-1 is mounted on the Huan Tran Telescope (HTT) (built by VertexRSI[1]), which is an off-axis Gregorian design that satisfies the Mizuguchi-Dragone condition. This optical design has a large diffraction limited field of view of 2.3 degrees, along with low sidelobe response and low cross polarization, meeting the systematic requirements for POLARBEAR-1's science goals. [63, 64]. The primary mirror is a 2.5 meter monolithic piece of cast aluminum, precision machined to 53 μm rms surface accuracy, with a lower-precision guard ring extending to 3.5 meter diameter. The primary produces a 3.5 arcminute FWHM beam at 148 GHz. The secondary mirror is 1.4 meter monolithic cast aluminum, with baffling enclosing it and the receiver window to block scattered light.

The transition edge sensor (TES) detectors are designed to operate at 0.25 Kelvin, where thermal carrier noise becomes subdominant compared to expected thermal background loading noise from the Chilean atmosphere. The bolometers have a design noise equivalent temperature (NET) of 500 $\mu \mathrm{K}_{CMB}\sqrt{s}$. The cryogenic receiver, shown in Figure 3.2, has a cumulative optical efficiency of 37%, including contributions from the focal plane, aperture stop, lenses, and filters [39]. A two-stage pulse tube refrigerator[2] provides continuous cooling power at 50 Kelvin and 4 Kelvin. A three-stage helium sorption fridge[3] provides two cooling stages at 0.35 Kelvin and 0.25 Kelvin, with a hold time greater than 30 hours.

[1] http://www.gdsatcom.com/vertexrsi.php
[2] http://www.cryomech.com
[3] http://www.chasecryogenics.com

Figure 3.1: **Huan Tran Telescope** — Photograph of the Huan Tran Telescope at its site in the Atacama desert of Chile.

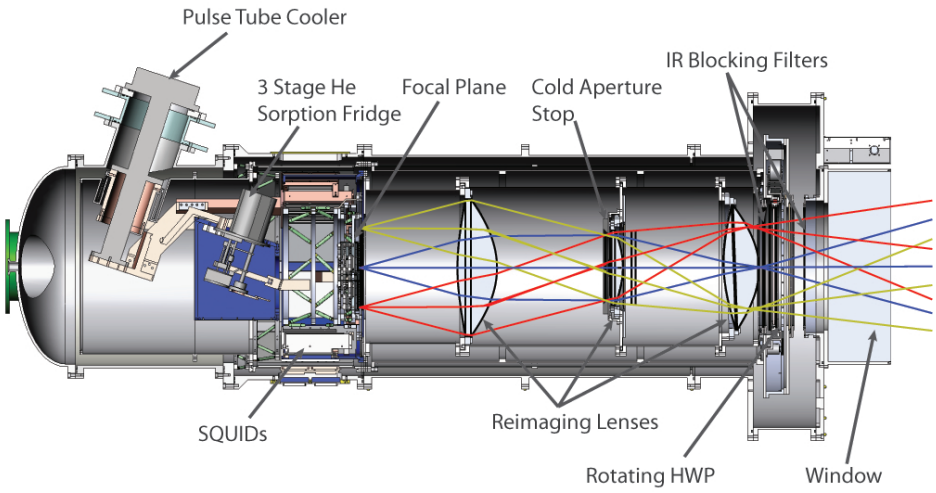

Figure 3.2: **POLARBEAR-1 cryostat** — A cross-sectional drawing of the POLARBEAR-1 cryogenic receiver with major components identified.

The focal plane, shown in Figure 3.3, consists of seven modular arrays of antenna-coupled transition edge sensor (TES) detectors, each with 192 detectors. An individual pixel, shown in Figure 3.4, consists of two Al/Ti bilayer TES detectors, coupled to orthogonal polarizations of the dual-polarized slot antenna, with on-chip band-defining filters [52]. Each pixel is paired with a beam-forming, anti-reflection coated lenslet [65]. Fluctuations in optical power are converted to changes in current in the voltage-biased TES detector, and this current is read out using a superconducting quantum interference device (SQUID). Reading out large arrays of detectors requires signal multiplexing in order to reduce thermal loading on the cold focal plane, as well as to reduce the cost, size, and complexity of cryogenic wiring and other cold readout components. POLARBEAR-1 uses frequency-domain multiplexing [32] with a multiplexing factor of eight.

3.2.3 First-season Instrument Performance

POLARBEAR-1 is located at the James Ax Observatory, at an altitude of 5200 meters on Cerro Toco in the Atacama desert in Chile and achieved first light in January 2012. This site was chosen for its dry, stable weather, with precipitable water vapor (PWV) less than 1.5 mm for over 50% of the year. This corresponds

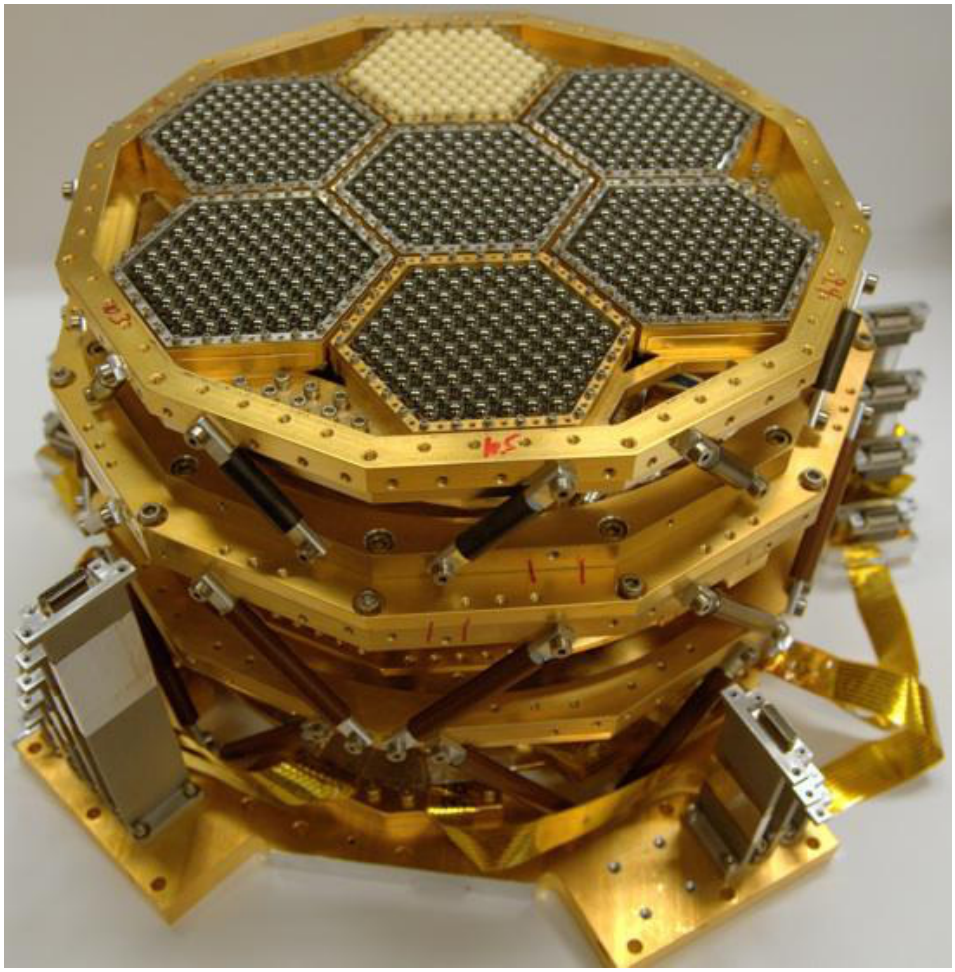

Figure 3.3: **POLARBEAR-1 focal plane** — A photograph of POLARBEAR-1's complete focal plane including lenslets, support structures and wiring. One array module has white alumina lenslets, the other six array modules have silicon lenslets.

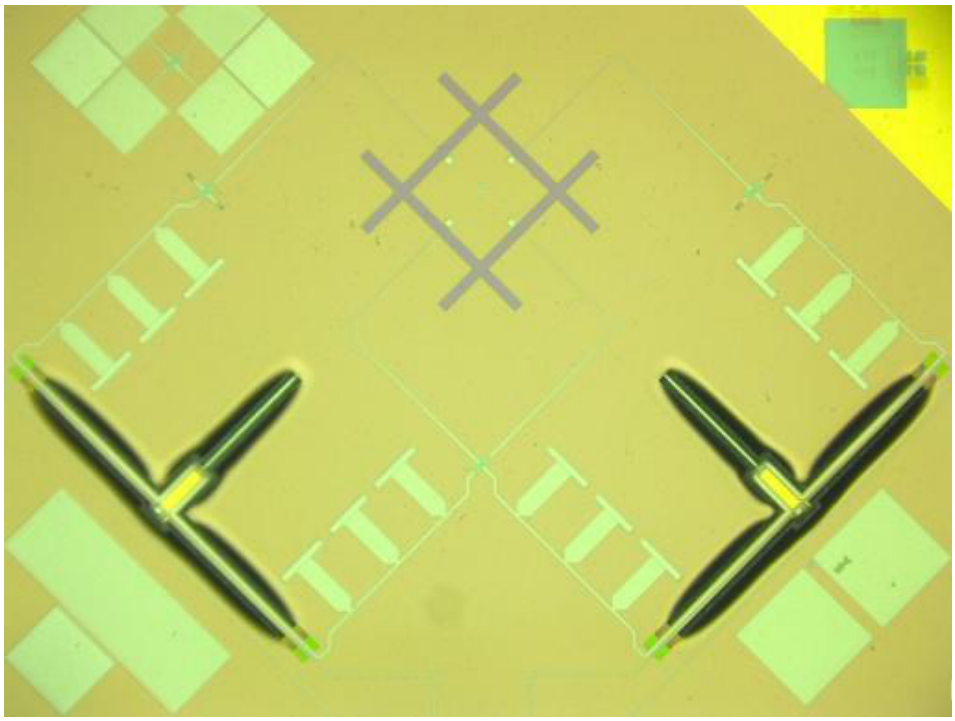

Figure 3.4: **POLARBEAR-1 pixel** — A photograph of a single pixel, with two TES detectors and slot antenna.

to a sky brightness in the POLARBEAR-1 design band of $15K_{RJ}$ at an elevation angle of 60 degrees.

Calibration is key to understanding the instrument's performance, and POLARBEAR-1 uses both hardware and astrophysical calibration sources. Calibration data for relative detector response is taken every hour during observations. The relative detector response is measured using a 3 minute observation of a variable frequency chopped thermal source located behind an aperture in the secondary mirror, with an effective temperature of 0.03 K. Relative detector response is also measured using fast elevation scans that vary detector response due to the changing line-of-sight air mass, spanning 3 degrees of elevation and approximately 0.5 Kelvin of sky temperature modulation. The relative detector response is used to calculate a differential timestream for the response of the two orthogonally oriented detectors within one pixel. This timestream can be used to measure the Q or U Stokes parameters while suppressing the unpolarized atmospheric signal.

The large fraction of the sky available to POLARBEAR-1 means that many

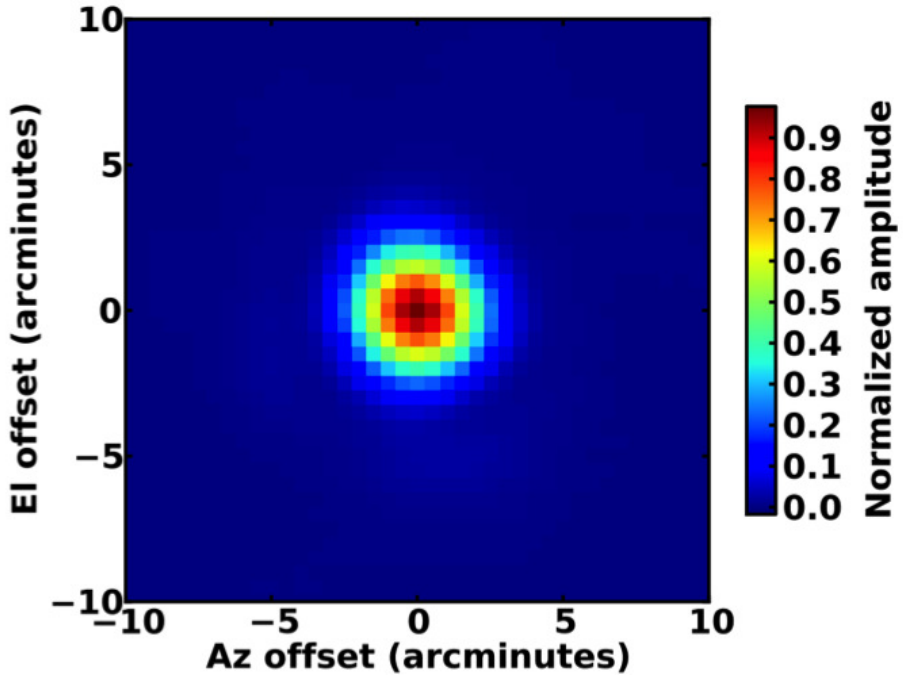

Figure 3.5: **POLARBEAR-1 instrument beam** — Coadded angular response of observations of Saturn.

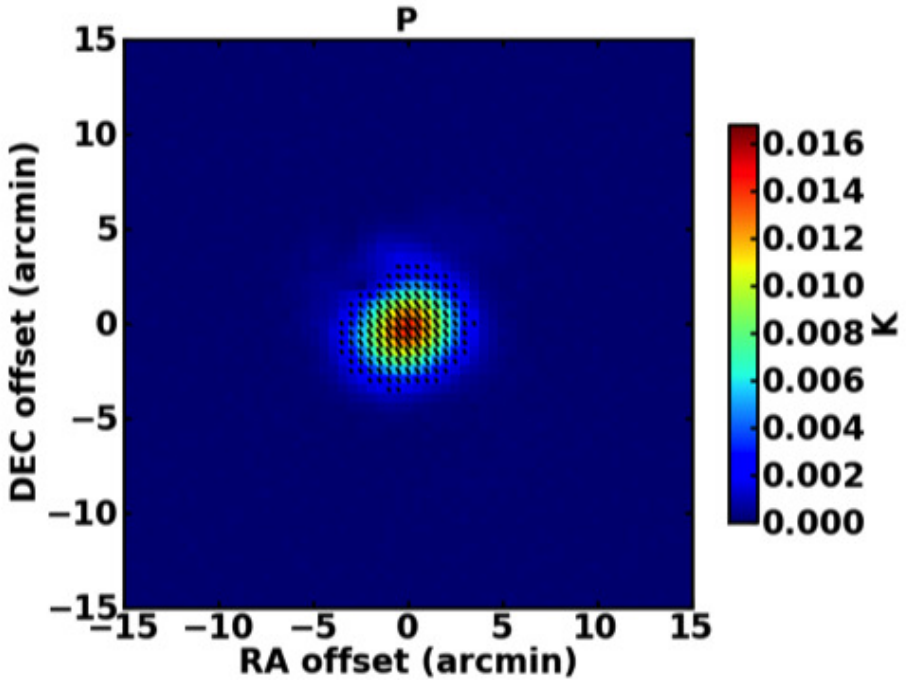

Figure 3.6: **POLARBEAR-1 polarization map of TauA** — Intensity and polarization map of the supernova remnant Taurus A.

astrophysical sources can be observed. Planets like Jupiter and Saturn are bright point sources, so observations of these planets map the structure of the beams. Each detector beam's size, ellipticity, and offset from boresite can be measured using planets. Figure 3.5 shows a coadded map made from all the active detectors during an observation of Saturn. The measured median FWHM beam size is 3.5 arcminutes, with a median ellipticity of 0.05 [39]. Planet observations can also be used to determine detector yield and NET, which vary with atmospheric conditions. The total number of active detectors is 1015, the typical operating yield during observations is about 900 detectors, and the median detector NET is 550 $\mu\mathrm{K}\sqrt{s}$. In the data set from the first season of observations, 746 bolometers were used in analysis, and the average array NET for this data is 23 $\mu\mathrm{K}\sqrt{s}$. Another important astrophysical calibrator for POLARBEAR-1 is Taurus A, a supernova remnant in the Crab Nebula. Taurus A has a well-known polarization angle, caused by synchrotron emission [66], and is used to calibrate relative detector polarization angles. Figure 3.6 shows a coadded temperature map of Tau A with the resulting polarization

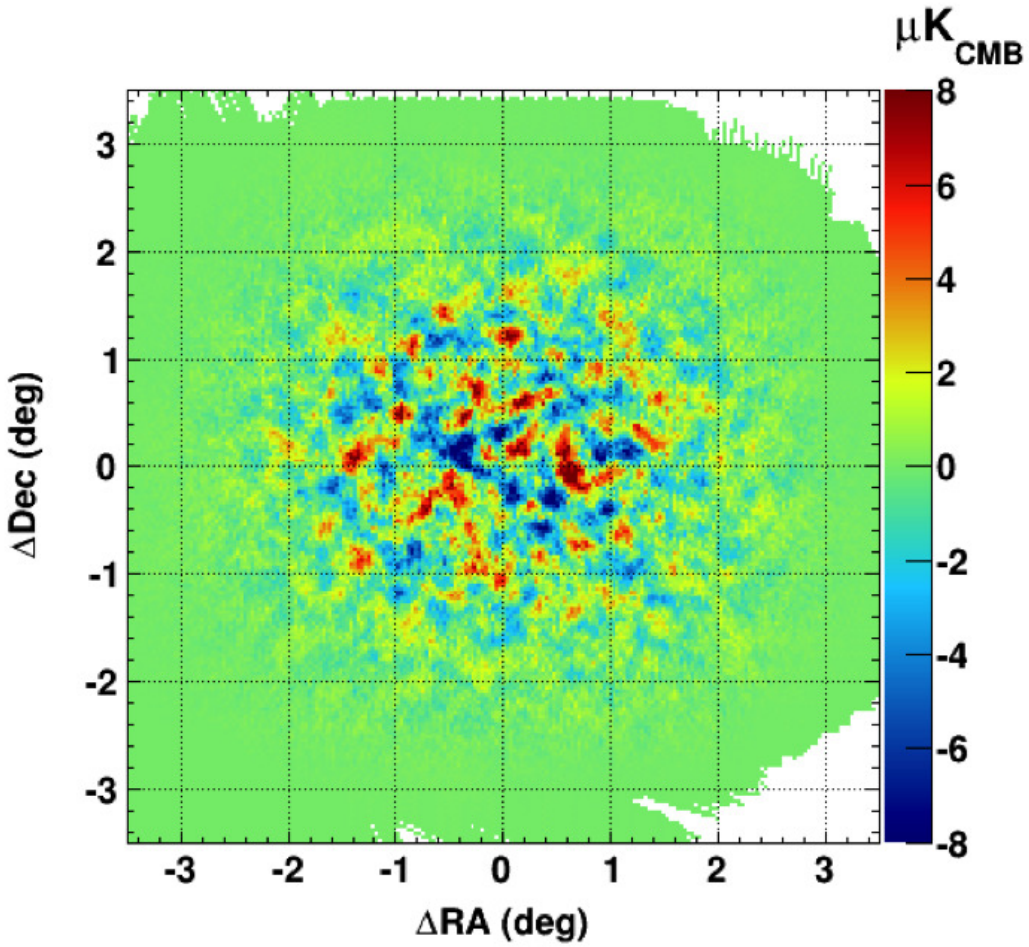

Figure 3.7: **POLARBEAR-1 E-mode map** — Preliminary first season E-mode polarization map for one of three observation patches, with approximately 1700 hours of observation time.

$P = \sqrt{Q^2 + U^2}$ and polarization angle of the source.

Shown in Figure 3.7 is the E-mode polarization for one of three sky patches observed by POLARBEAR-1. The preliminary map depth for this patch is 5 $\mu\mathrm{K}_{CMB}-$ arcminute for polarization.

3.3 POLARBEAR-1 First Season Results

The POLARBEAR collaboration published results from our first season of observations with POLARBEAR-1 (described in Section 3.2) in 2014, using three

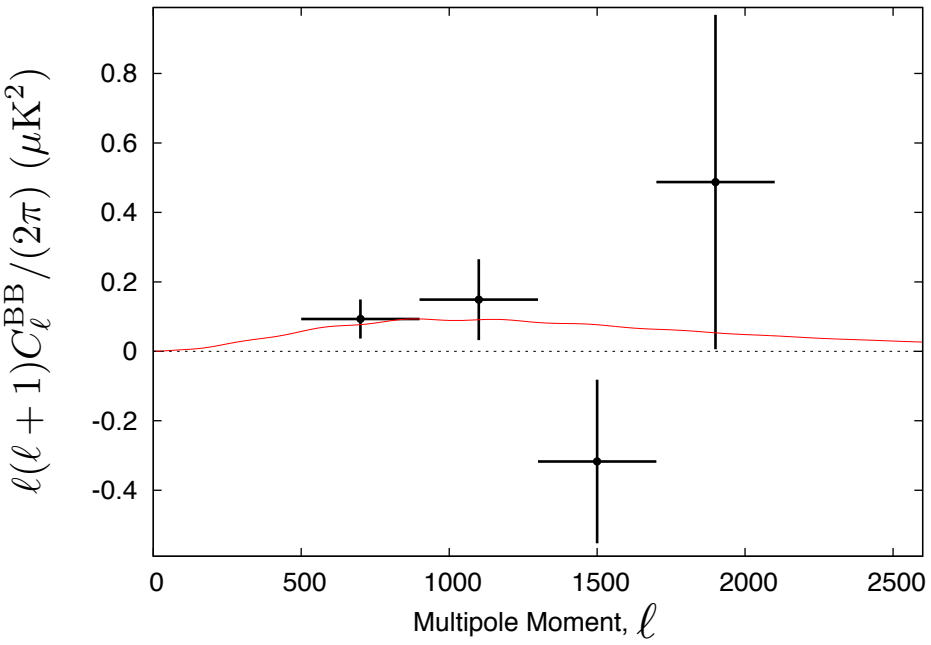

Figure 3.8: **CMB B-mode polarization power spectrum measurement from POLARBEAR-1 first season data** — The binned C_ℓ^{BB} spectrum is shown using data from POLARBEAR-1 first season observations, combining three patches of the sky. The theoretical prediction for the C_ℓ^{BB} spectrum is shown in red, based on WMAP-9 cosmological parameters. (POLARBEAR Collaboration 2014c [56])

different analysis techniques to probe the B-mode polarization signal. The first season of observations focused on deep observations of a small fraction of the sky, in order to quickly reach the sensitivity where CMB polarization is a more sensitive probe of lensing than CMB intensity.

These measurements spanned the angular multipole range $500 < \ell < 2100$, with observations of an effective sky area of $25 deg^2$ with a resolution of 3.5 arcminutes. At these angular scales, the dominant source of B-mode polarization is gravitational lensing of the CMB by large-scale structure (described in Section 1.2.4). At the observation frequency, 150 GHz, at these small angular scales, the CMB is expected to be the dominant source of polarization within the observations areas, far from the Galactic plane.

For the B-mode polarization power spectrum C_ℓ^{BB} results, the data were binned into four multipole bins, and this result is shown in Figure 3.8. The null hypothesis of no B-mode polarization power from gravitational lensing is rejected with 97.2% confidence with these results (including systematic and statistical uncertainties). These results can be compared with the prediction from the standard ΛCDM cosmological model, based on cosmological parameters from WMAP-9, with the amplitude of the lensing peak from the parameters $A_{BB} = 1$. Fitting our data to the ΛCDM model with this single parameter A_{BB}, we find our results fit with $A_{BB} = 1.12 \pm 0.61(stat)^{+0.04}_{-0.12}(sys) \pm 0.07(multi)$, where *stat* refers to the statistical uncertainty, *sys* refers to the systematic uncertainty from the instrument and astrophysical foregrounds, and *multi* refers to calibration uncertainties with a multiplicative effect on the amplitude A_{BB}.

The analysis included many detailed studies and evaluations of the effect of instrumental systematics on C_ℓ^{BB}. The analysis was "blind" to the C_ℓ^{BB} power spectrum results until the analysis pipeline was complete and it was ensured that there was no significant systematic effect on the data that could create a spurious C_ℓ^{BB} signal. Simulations were used to quantify the amplitude of all known systematic effects, and the results of this study are shown in Figure 3.9. An important step in our analysis was ensuring that the sum of these systematics effects was much less than the statistical uncertainty of the data set (here, POLARBEAR-1 first season

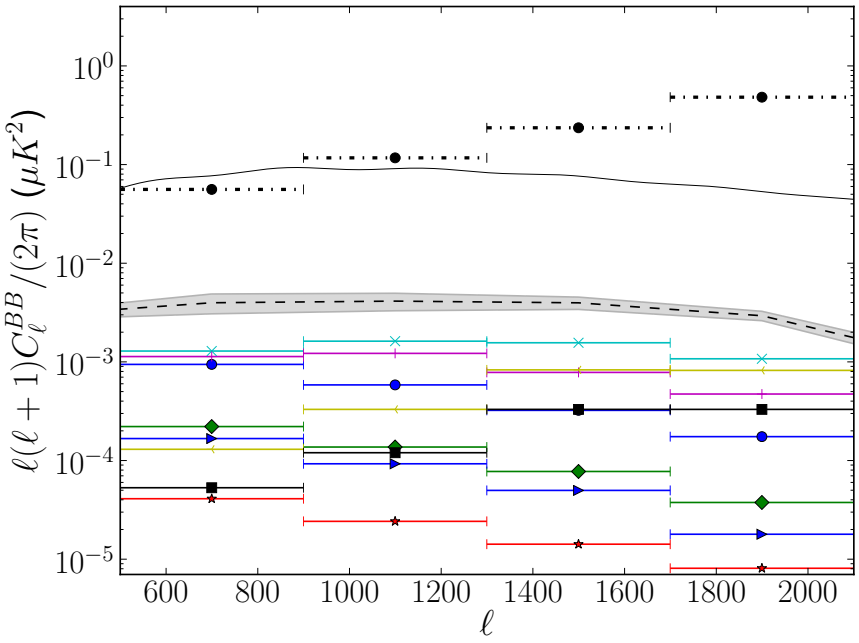

Figure 3.9: **POLARBEAR-1 instrumental systematic effects** — The potential bias from instrumental systematic effects in the C_ℓ^{BB} power spectrum are shown, along with their cumulative effect (black dashed line with grey 1σ bounds, the expected gravitational lensing signal (solid black line), and the statistical uncertainty from the first-season data set (black dashed points). The individual instrumental systematic effects included are the pointing model and differential pointing uncertainty (light blue cross), the residual uncertainty in instrumental polarization angle after calibration (purple plus), the differential beam size (yellow arrow), the beam ellipticity (black square), electrical crosstalk (blue arrow), gain drift (red star), and gain model changes (green diamond and blue circle) (POLARBEAR Collaboration 2014c [56])

observations). To search for unknown or unexpected systematic effects, and to ensure that the data set is internally consistent, we used a null test framework. A null test splits a data set into two parts based on potential sources of systematic contamination or miscalibration, and the data set passes the null test if these two parts are shown to be as consistent as expected. The POLARBEAR null test framework included a suite of nine null tests that the data set was required to pass. These tests were required to be reasonably independent from each other. The full description of these null tests can be found in Reference [56].

In addition to the C_ℓ^{BB} power spectrum results, the POLARBEAR collaboration used two additional complementary analysis techniques to probe the B-mode signal from gravitational lensing. The B-mode polarization signal due to gravitational lensing arises from the conversion of E-mode polarization to B-mode polarization when the CMB photon trajectories are deflected (as described in Section 1.2.4). We used our CMB polarization data to estimate these deflections, taking advantage of the conversion from Gaussian primary anisotropy to non-Gaussian lensed anisotropy. We use two quadratic estimators for lensing of CMB polarization $< EEEB >$ and $< EBEB >$ to determine the power spectra of the lensing deflection field, C_ℓ^{dd}, and combine the two estimators to increase the signal-to-noise. With the POLARBEAR-1 first season observations, this resulted in a rejection of the absence of polarization lensing at 4.2σ, and found an amplitude of the polarization lensing power spectrum of $\mathcal{A} = 1.06 \pm 0.47^{+0.35}_{-0.31}$, normalized to the standard ΛCDM prediction. A complete description of this analysis and results can be found in Reference [54].

The CMB lensing signal can also be cross-correlated with maps that trace the large-scale structure which is generating the gravitational lensing of the CMB. This technique was first used to detect the gravitational lensing signal with CMB temperature data [67, 68, 69, 70]. Maps of the cosmic infrared background (CIB) at a wavelength of $\sim 500\mu m$ trace the high-redshift distribution of luminous galaxies, and have been found to be highly correlated with the CMB lensing signal[71]. By cross-correlating the POLARBEAR-1 first season observations with CIB maps from the *Herschel* satellite, we were able to show evidence for the presence of a

lensing B-mode signal at a significance of 2.3σ [55]. These results through cross-correlation with two independent data sets from different instruments are valuable because they are much less sensitive to potential contamination and systematic effects.

3.4 POLARBEAR-2

POLARBEAR-2 is a next-generation receiver for precision measurements of the polarization of the cosmic microwave background (CMB). Scheduled to deploy in early 2016, it will observe alongside the existing POLARBEAR-1 receiver, on a new telescope in the Simons Array on Cerro Toco in the Atacama desert of Chile. The POLARBEAR-2 receiver will onto a telescope that will be identical to the Huan Tran Telescope, described in Section 3.2. A drawing of the new telescope with POLARBEAR-2 receiver is shown in Figure 3.10.

For increased sensitivity, it will feature a larger area focal plane, with a total of 7,588 polarization sensitive antenna-coupled TES bolometers, with a design sensitivity of 4.1 $\mu\mathrm{K}\sqrt{\mathrm{s}}$. The focal plane will be cooled to 250 milliKelvin, and the bolometers will be read-out with 40× frequency domain multiplexing, with 36 optical bolometers on a single SQUID amplifier, along with 2 dark bolometers and 2 calibration resistors. To increase the multiplexing factor from 8× for POLARBEAR-1 to 40× for POLARBEAR-2 requires additional bandwidth for SQUID readout and well-defined frequency channel spacing. Extending to these higher frequencies requires new components and design for the LC filters which define channel spacing. The LC filters are cold resonant circuits with an inductor and capacitor in series with each bolometer, and stray inductance in the wiring and equivalent series resistance from the capacitors can affect bolometer operation. We present results from characterizing these new readout components. Integration of the readout system is being done first on a small scale, to ensure that the readout system does not affect bolometer sensitivity or stability, and to validate the overall system before expansion into the full receiver.

In Section 3.4.1, we discuss the overall instrument design for POLARBEAR-2. In Section 3.4.2, we discuss the readout system and the requirements placed on it from the overall instrument design and specifications. In Section 3.4.3, we describe the characterization of the detectors and the expected sensitivity of the array. Further details can be found in proceedings on the Simons Array [16], POLARBEAR-2 [72] and the room temperature electronics [49].

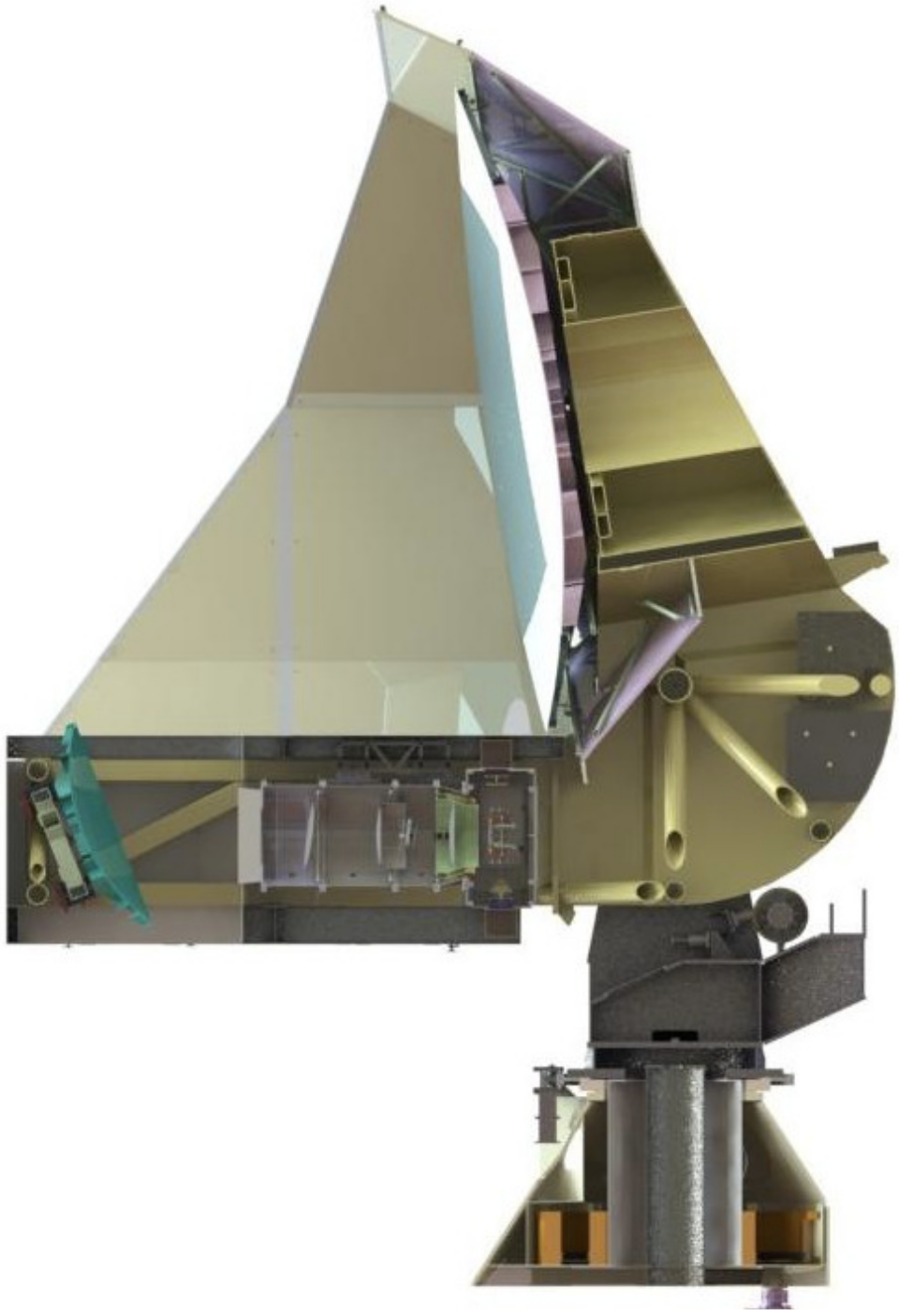

Figure 3.10: **POLARBEAR-2 telescope** — Drawing of the POLARBEAR-2 receiver mounted on the telescope.

3.4.1 POLARBEAR-2 Instrument Design

Improving the sensitivity of CMB measurements requires expanding to many more detectors, since the sensitivity of transition-edge sensor (TES) bolometers observing at millimeter-wave is limited by photon statistics [27]. Observations at multiple frequencies are also necessary, in order to separate out the underlying CMB signal from astrophysical foreground contamination. The POLARBEAR-1 focal plane has 1,274 detectors observing at a single frequency, 150 GHz. The overall design of POLARBEAR-2 is similar to POLARBEAR-1, with significant differences that improve the overall sensitivity. POLARBEAR-2 will have a larger focal plane area, with 1897 pixels with a new sinuous antenna design. The sinuous antenna can couple to multiple frequencies, with a broader bandwidth than the slot dipole used in POLARBEAR-1. Each pixel has four transition edge sensor (TES) bolometers, coupled to the sinuous antenna with two frequency bands at 95 GHz and 150 GHz, and two polarization orientations, shown in Figure 3.12. The focal plane will have a total of 7,588 detectors. The increase in detector count on the focal plane required an increase in the readout multiplexing factor, from 8× in POLARBEAR-1 to 40× in POLARBEAR-2, requiring changes to the readout system. The POLARBEAR-2 receiver design also includes an additional two-stage pulse-tube cryocooler dedicated to the cold optics, reducing the background photon loading on the focal plane and decreasing the detector noise equivalent temperature (NET). POLARBEAR-2, shown in Fig. 3.11, is scheduled to deploy at the end of 2015 onto a new telescope at the POLARBEARsite in the Atacama desert [72]. After POLARBEAR-2 is deployed, a copy of this receiver will be made and installed on the third telescope of the Simons Array. The original POLARBEAR-1 receiver will finally be replaced with a third receiver with this style of expanded multichroic array. The full Simons Array of three telescopes will include 5691 multichroic pixels with 22,764 detectors observing at three different frequencies.

Table 3.1: Design comparison of POLARBEAR-1 and POLARBEAR-2

Specification	POLARBEAR-1	POLARBEAR-2
Frequencies	150 GHz	95 GHz and 150 GHz
Number of pixels	637	1897
$NET_{bolometer}$	550 μK$\sqrt{\text{s}}$ (median, first season)	360 μK$\sqrt{\text{s}}$ (design)
NET_{array}	23 μK$\sqrt{\text{s}}$ (median, first season)	4.1 μK$\sqrt{\text{s}}$ (design)
Field of view	2.3 deg	4.8 deg
Beam size	3.5 arcmin	3.5 arcmin at 150 GHz, 5.2 arcmin at 95 GHz

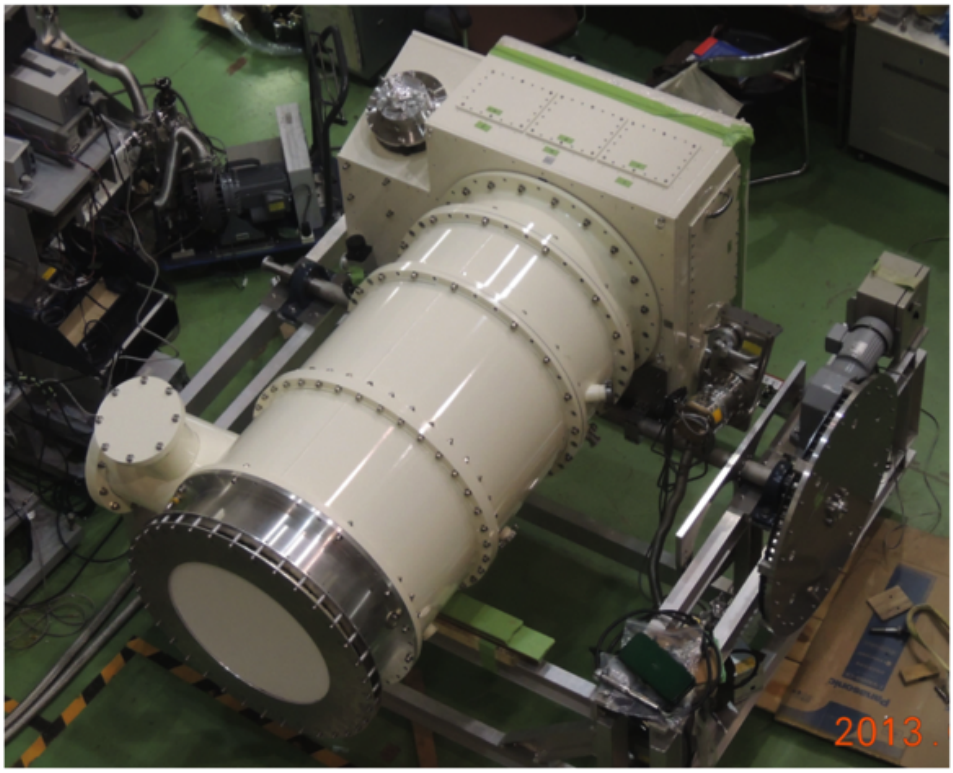

Figure 3.11: **POLARBEAR-2 receiver** — Photograph of the POLARBEAR-2 receiver in the lab at KEK.

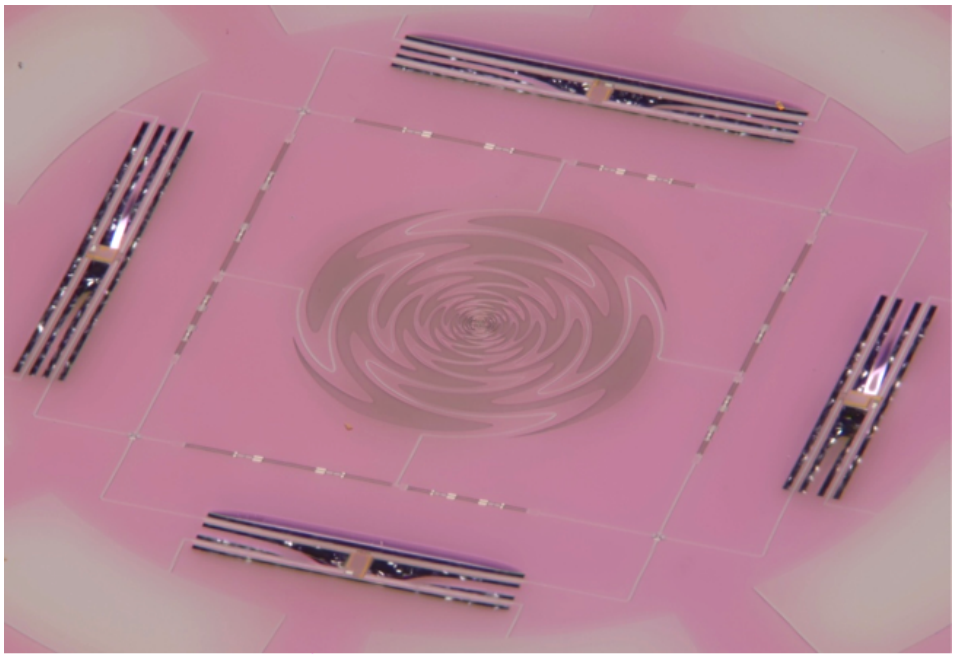

Figure 3.12: **Sinuous antenna for POLARBEAR-2** — Photo of a dichroic pixel for POLARBEAR-2, with the sinuous antenna at the center, surrounded by four TES bolometers.

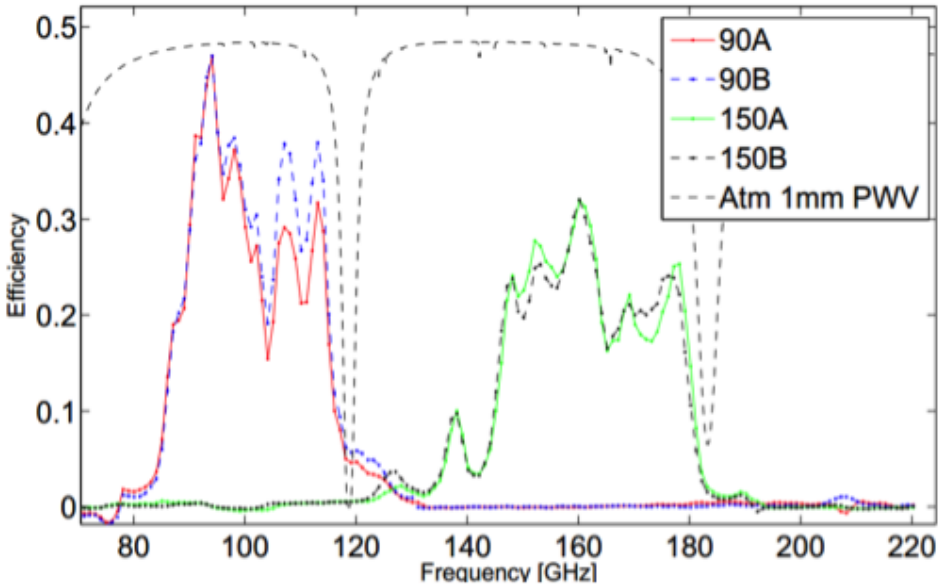

Figure 3.13: **POLARBEAR-2 frequency bands** — Measured spectra of a prototype POLARBEAR-2 pixel, showing the two frequency bands centered at 95 GHz and 150 GHz, which are within atmospheric windows.

3.4.2 Readout System and Requirements

TES detectors are thermistors with a steep power-resistance relation at their superconducting transition, as described in detail in Section 2.2. The TES detectors are operated with a low-impedance voltage bias, which causes electro-thermal feedback (ETF) that keeps the total power (optical power and electrical power) at a constant level. Incident optical power is then converted into a changing current, which can be measured by a Superconducting Quantum Interference Device (SQUID) (described in Section 2.3). In the frequency-domain multiplexing (fMux) readout system, described in detail in Section 2.5 and in Reference [32], multiple detectors are read out continuously on the same set of wires by separating their signals in frequency space. Each detector in a module is voltage biased at a unique frequency, defined by a cold resonant filter with an inductor and capacitor in series with the detector. Current from the bolometers are summed and pre-amplified by series-arrays of SQUIDs, cooled to 4 Kelvin. The signal is amplified and demodulated by room-temperature electronics.

The increased number of detectors requires the multiplexing factor to increase as well, due to constraints from thermal loading from wiring, space inside the cryostat, cost, and other factors. The multiplexing factor will increase from 8× for POLARBEAR-1 to 40× for POLARBEAR-2, and will eventually increase further for future instruments. This requires additional bandwidth for SQUID readout and well-defined frequency channel spacing. While expanding the readout system to this higher multiplexing factor, we must ensure that detector performance is not compromised by factors like readout noise, electrical crosstalk, and detector stability.

3.4.2.1 SQUID Amplifiers

Current through the bolometers is summed and pre-amplified by a SQUID at 4 Kelvin, coupled through a superconducting input coil. This coil's low impedance preserves the voltage bias across the bolometers, which have a resistance of approximately 1Ω. Series-array SQUIDs, described in Section 2.3.1, can achieve a high transimpedance amplification, and the SQUID output voltage is read out with

room-temperature amplifiers.

The response of a SQUID can be approximated using Equation 3.1, where V_{OUT}^{SQ} is the output voltage, I_{IN} is the current through the input coil, V_{pp} is the peak-to-peak output voltage, and I_{ϕ_0} is the input current which produces a quantum of magnetic flux:

$$V_{OUT}^{SQ} = 1/2 V_{pp} \sin(2\pi I_{IN}/I_{\phi_0}) \; . \tag{3.1}$$

The relation of input current to flux quanta is fixed by geometry, but the transimpedance depends on the SQUID temperature and the current bias applied. The operating point is set along the downward sloping linear region of this curve, where the transimpedance Z_{SQ} is approximately $\pi V_{pp}/I_{\phi_0}$. For our devices, manufactured at NIST [73], V_{pp} ranges from $1.5 - 5$ mV, and $I_{\phi_0} \approx 25\mu A$. The SQUIDs undergo initial screening where they are submerged in liquid helium and the output response is measured. From these measurements, V_{pp} and the transimpedance are determined. An example showing the fit to the simple sine wave approximation is shown in Figure 3.14. Results from screening a wafer of SQUIDs is shown in Figure 3.15. SQUIDs with high transimpedance are selected and undergo further characterization to find optimal bias values and determine noise properties.

The requirements for SQUID performance are calculated based on keeping the SQUID readout noise contributions subdominant to the bolometer power noise terms, as described in Section 2.3.3. This power noise is referred to the input of the SQUID as a current noise in order to compare to readout noise. Each SQUID readout noise terms is expected to be subdominant to the bolometer power noise contribution, as calculated when the optical loading is the lowest. The first SQUID readout noise contribution is fundamental SQUID noise, which is around 3.5 pA$\sqrt{\text{Hz}}$. The room-temperature amplifier also contributes noise, with a specification of 1.2 nV$\sqrt{\text{Hz}}$[32]. To keep this contribution low, below 3.1 pA$\sqrt{\text{Hz}}$, there is a minimum requirement on the transimpedance of each SQUID, $Z_{SQ} > 400\Omega$.

We are investigating two different SQUID designs for use in POLARBEAR-2 and the future Simons Array receivers. The existing SQUID design used in POLARBEAR-1 is a 100 element series array of SQUIDs, with a typical array noise

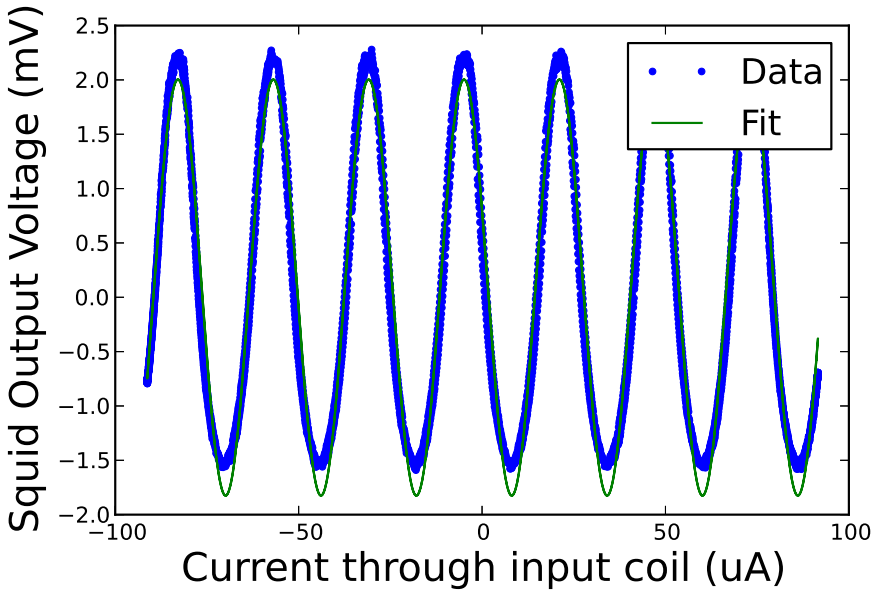

Figure 3.14: **SQUID Response** — Output response of a typical SQUID series array, with model to estimate transimpedance.

of 3.5 pA$\sqrt{\text{Hz}}$, and a bandwidth of 120 MHz. With screening, these SQUIDs will have acceptable properties to keep their readout noise within specifications. However, there are still gains to be made with reducing this noise by reducing the fundamental SQUID noise and increasing the transimpedance, which would help improve the overall NET_{array}. The alternate SQUID design, also made by NIST, consists of banks of 64 element arrays, that can be connected in series and parallel combinations, for example a 3 by 2 array, depending on the desired configuration for output impedance and transimpedance. We are continuing to test different designs of SQUIDs for their noise and transimpedance properties, and will screen for the best elements to include in the final receivers.

For POLARBEAR-1 and other first-generation fMux systems, the SQUIDs were operated using a flux locked loop with shunt feedback [32], described in Section 2.3.2. This shunt feedback works to keep the SQUID in the linear region of its output, extending the dynamic range of input current. However, shunt feedback has a limited usable bandwidth of about 1.3 MHz, and increasing the multiplexing factor will require extending the usable readout bandwidth to several MHz.

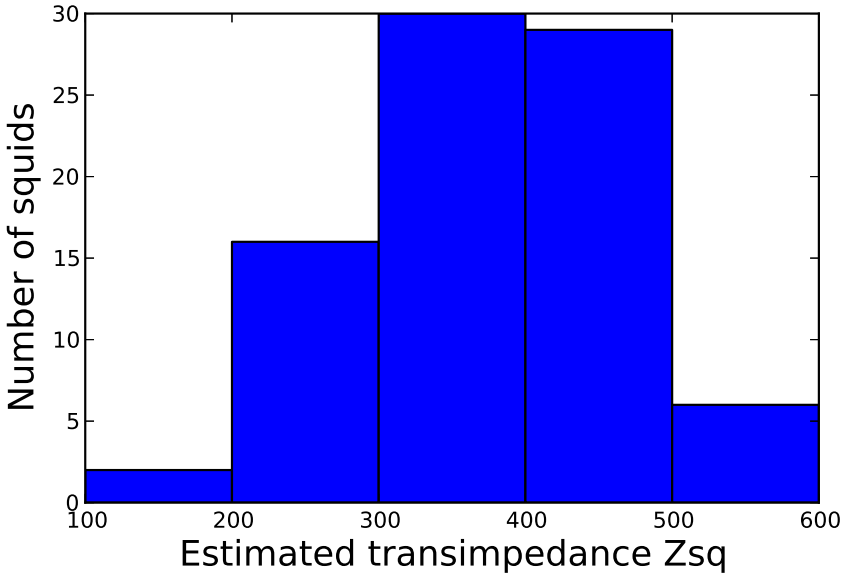

Figure 3.15: **Transimpedance distribution** — Distribution of estimated transimpedance values for a wafer of SQUID series arrays.

For POLARBEAR-2 and other experiments with higher multiplexing factor, a new feedback scheme will be used which is called Digital Active Nulling (DAN), which is described in Section 2.5 and Ref. [48]. With DAN, the current at the SQUID is nulled in a digital feedback loop for each bolometer frequency channel. The bandwidth of the new electronics with DAN implemented is now 10 MHz.

With increased readout bandwidth, the low pass RF filtering on the cryostat, achieved with pi filters, will need to be relaxed out to several MHz. Noise pickup from auxiliary electronics, telescope motors, and other sources will need to be characterized and eliminated from the readout band. Figure 3.16 shows a typical noise spectral analysis for the SQUID output from the POLARBEAR-1 system, showing the noise floor with Johnson noise peaks at the bolometer frequencies.

3.4.2.2 Channel Defining Filters

The readout channels are defined by an LC filter with an inductor and a capacitor in series with each bolometer. For POLARBEAR-1, these were 16 μH inductors made by NIST along with commercial ceramic capacitors. For POLARBEAR-2,

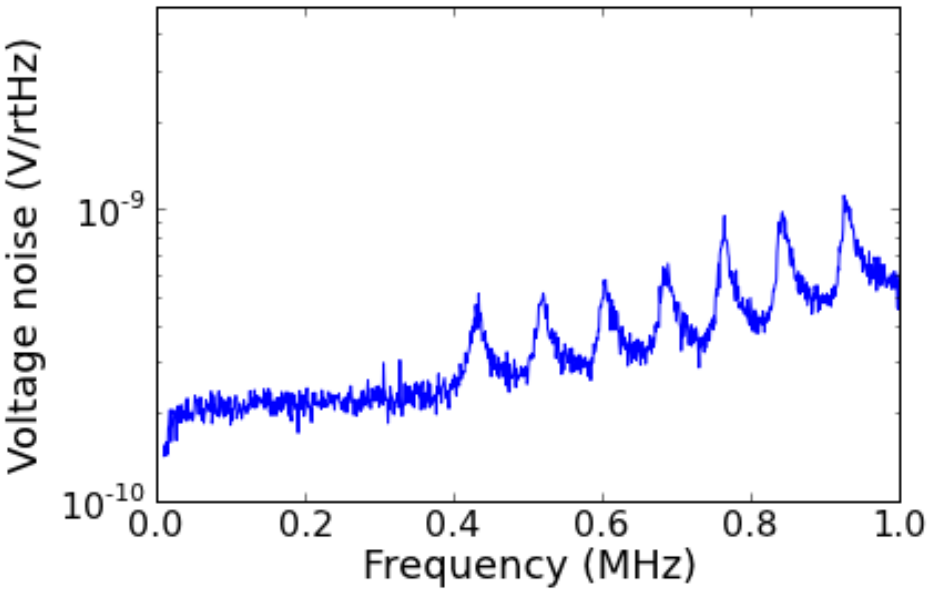

Figure 3.16: **SQUID noise** — Voltage noise vs frequency for a SQUID in a flux-locked loop, with Johnson noise peaks from bolometers at 1.5 Kelvin.

the increase in readout bandwidth and decrease in channel spacing requires significant improvements in the inductor and capacitor properties. The equivalent series resistance (ESR) of commercial capacitors increases with frequency, and at the higher end of the readout bandwidth this would become so large that it is comparable to the bolometer resistance, affecting bolometer performance and stability, as described in Section 2.5. Interdigitated capacitors with low ESR have been developed, and are now fabricated at UC Berkeley and Lawrence Berkeley National Laboratory [74]. These interdigitated capacitors are made of a single layer of aluminum on single crystal silicon. Current limits to the physical size and capacitance of these components sets the lower end to the frequency band, 1.5 MHz. At our focal plane base temperatures, the aluminum goes superconducting and these components have very low loss. The inductance value has been increased to 60 μH, which makes the resonance peak narrower and allows closer channel spacing. The decrease in bandwidth is not expected to affect bolometer stability, as the electrical time constant is still more than 10$\times$ faster than the detector time constant [26]. These inductors and capacitors are being fabricated together on the same chip. To reduce mutual inductance between inductors, their physical spacing is

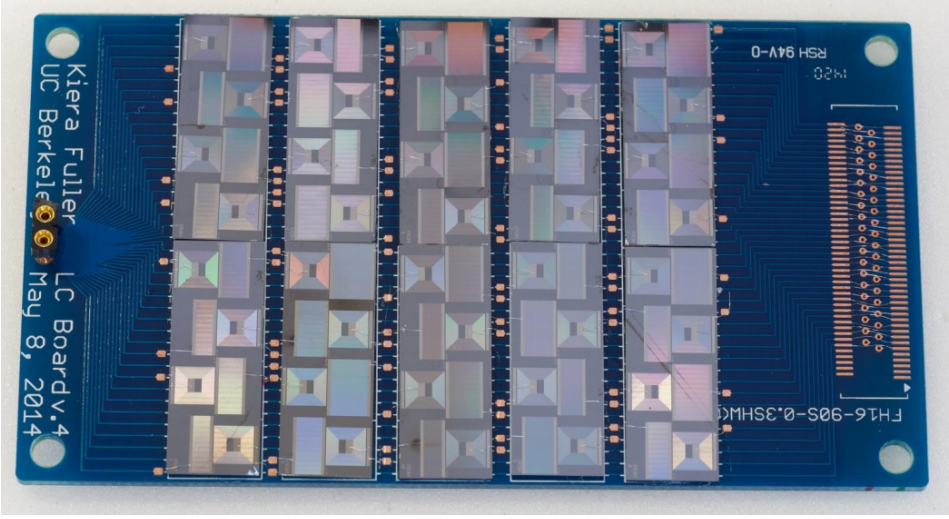

Figure 3.17: **Channel-defining LC filters for** 40× **comb** — Photograph of a set of 40 LC filter channels on a prototype mounting board.

maximized using a checkerboard pattern, with alternating placement of inductors and capacitors. The requirement on electrical crosstalk is that it is less than the optical crosstalk, which is expected to be $<\sim 1\%$. The layout and spacing of the LC components, along with the frequency schedule values and channel spacing, ensures that crosstalk is below this specification. The fabrication process allows us to achieve tight tolerances in values so that the channel locations and spacing are well-constrained. A full 40 channel set of LC filters is shown in Figure 3.17.

The ESR of these components has been shown to be very low out to several MHz, and is measured as described in 2.5 and Equation 2.26. The expected total series resistance, including ESR from the capacitors and inductors, and stray resistance from connectors and wiring, is less than 0.2 Ohms. These LC chips went through initial detailed characterization to understand the expected properties of mass-fabricated chips. Screening every set of LC chips would be a time-consuming process, especially since the resonant peaks can only be measured below the transition temperature of aluminum, 1.2 Kelvin. The key properties of these chips are the ESR and the scatter in component values. The spacing of channels in the frequency schedule is set by the expected scatter in channel placement, which is caused by scatter in component values. For a set of 40 channels to be acceptable

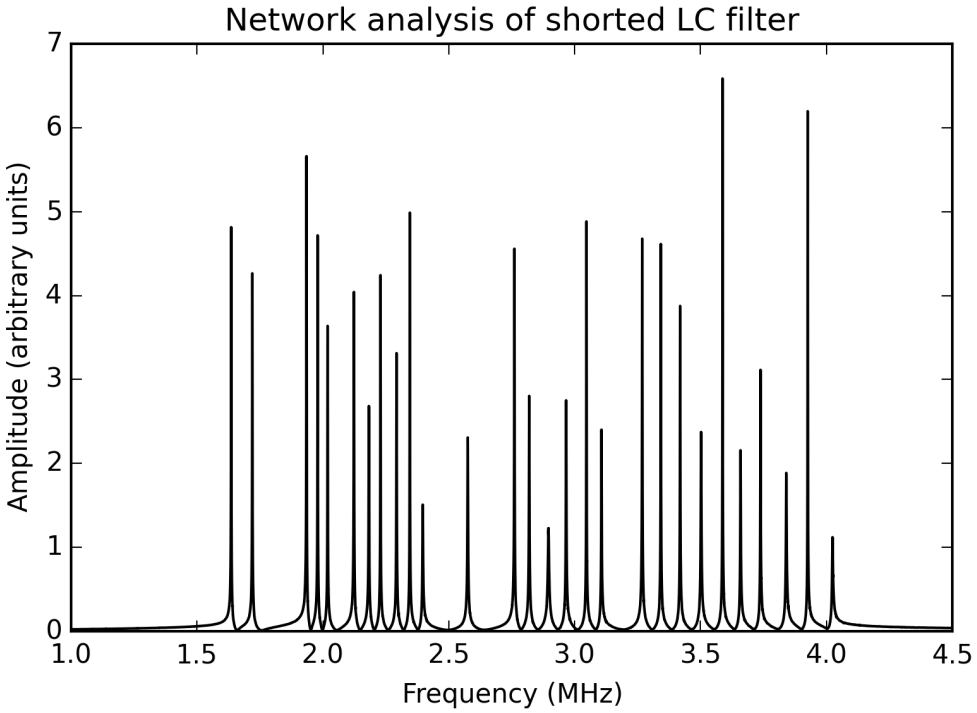

Figure 3.18: **Network analysis of prototype 40 channel LC comb** — Network analysis results of a prototype 40 channel LC comb. Missing peaks are thought to be due to bad wirebond connections.

for deployment, it must have high yield, the integrated LC filters and wiring must have a measured ESR below 0.2 Ohms, and channel spacing must be greater than 40 kHz. The electrical connection to these chips is made with an aluminum wirebond, which we found could have inconsistent connections due to the wirebonder punching through the thin aluminum layer. Using an automatic wirebonder both eliminated this problem, as well as made the mass-fabrication of these assembled components much easier. A network analysis of one of the prototype 40 channel LC combs is shown in Figure 3.18, along with the ESR measurements derived from these results in Figure 3.19.

3.4.2.3 Frequency Schedule

With the current constraints for the lower and upper bounds for the readout bandwidth, and the expected scatter in channel placement, the result is that the

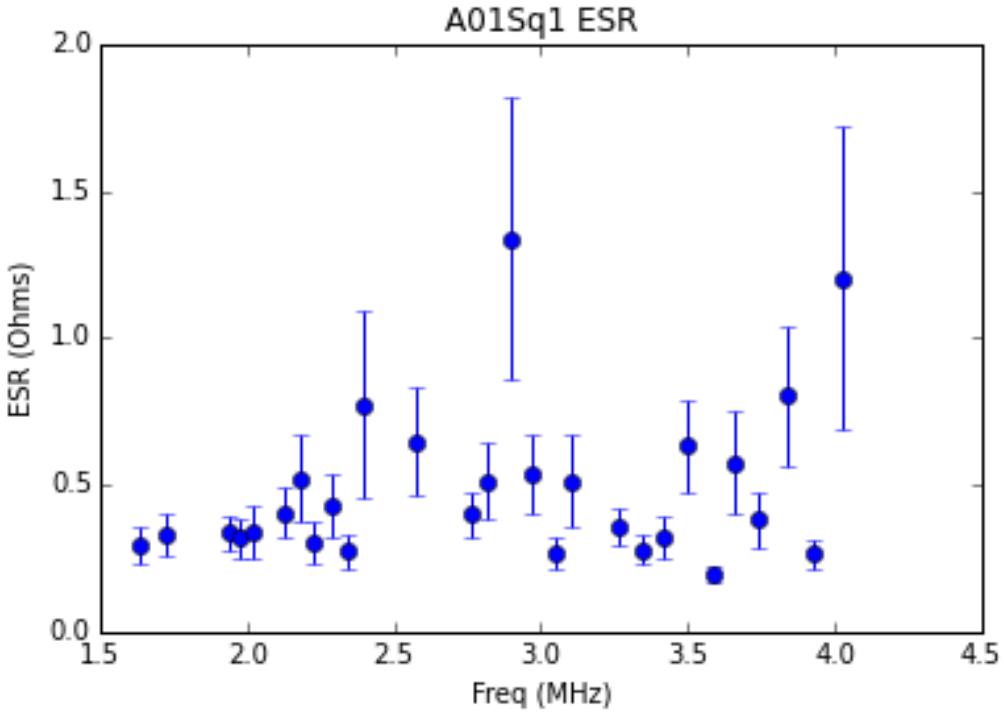

Figure 3.19: **Equivalent series resistance of prototype** $40\times$ **comb** — Equivalent series of a prototype comb, measured using a shorted network analysis of the resonant LCR peaks. The scatter results from the ESR of the components, as well as stray resistance from connections.

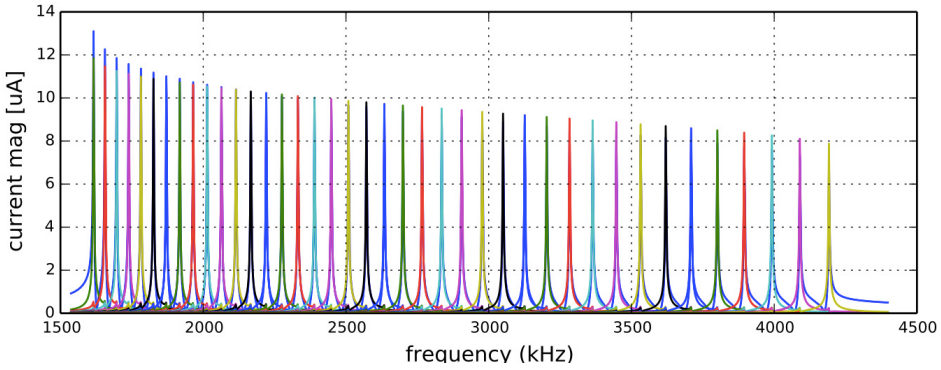

Figure 3.20: **Simulated frequency channels** — Simulated frequency response for a 40 channel frequency multiplexing setup, showing admittance of the resonant filters, each consisting of a 60 μH inductor and an interdigitated capacitor

currently achievable multiplexing factor is 40, shown in Figure 3.20. We expect to be able to expand the usable bandwidth and increase to at least 64× multiplexing for future experiments.

3.4.2.4 Cold Cable Design

While the multiplexing system greatly reduces the numbers of wires needed to run to the detectors at the cold stage, these wires must be carefully designed to minimize their effect on the readout system. This wiring connects the SQUIDs on the 4 Kelvin stage with the LC boards at 250 mK, and must both connect these components with minimal resistance ($R << R_{TES}$), as well as minimal thermal loading on the subKelvin stages. It must also be long enough to physically make these connections across a large focal plane ($L \sim 0.5m$). This wiring introduces a stray inductance in series with the detectors and LC filters, outside of the LCR resonant circuit. The voltage drop caused by this impedance reduces the bolometer voltage bias, with an effect that increases with frequency. This effect is described in more detail in Section 2.5. The impedance of this wiring must remain small compared to the $\sim 1\Omega$ bolometer impedance at the highest readout frequency of 4 MHz [32].

Superconducting materials can meet the electrical and thermal requirements, since below the critical temperature, the resistivity drops to zero, and

the thermal conductivity also drops rapidly. The electron contribution to thermal conductivity is suppressed by electrons forming Cooper pairs and no longer carrying thermal energy [75]. The phonon conductivity is determined by the lattice structure, and can remain relatively high in pure metals [76]. The material used for these wires is NbTi, an alloy of niobium and titanium that is a type II superconductor with a critical temperature of 10 Kelvin. The thermal conductivity below the critical temperature varies depending on the concentration and the manufacturing process, but is known to be very low [77, 78]. These cold cables will be used at temperatures exclusively below 5 Kelvin, well below the critical temperature, and the expected thermal conductivity in this range is shown in Figure 3.21. These cables will have thermal intercepts at two different temperature stages before reaching the 250 mK focal plane. The penultimate intercept is at the 350 mK stage, cooled by the intermediate cold head, which has much greater cooling power than the ultra cold head, but the loading on this stage can have a negative effect on the overall hold time of the sorption fridge, affecting observing efficiency. Ensuring that the NbTi cable has a good thermal connection to the first thermal intercept, at the heat exchanger stage, greatly reduces the loading on the intermediate cold head, as shown in Figure 3.22.

NbTi is a relative brittle metal that forms a strong oxide layer, and can be difficult to work with. In its most common application, superconducting magnets, NbTi is embedded in a copper matrix that is used to add mechanical strength and facilitate electrical connections [79]. Since we require low thermal conductivity, copper cannot be part of a significant length of the final cable. One potential fabrication method was to include this copper cladding and then etch it away, except for the ends. The copper cladding must be included starting with surrounding the initial ingot of NbTi with copper, and rolling it out into sheets, which is a relatively complicated process. To keep the total inductance low, the design for this wiring is a broadside coupled stripline, where the inductance can be determined using the width of the traces w, the distance between traces h, and the permeability μ, using Equation 3.2:

$$L = \mu h/w \ . \tag{3.2}$$

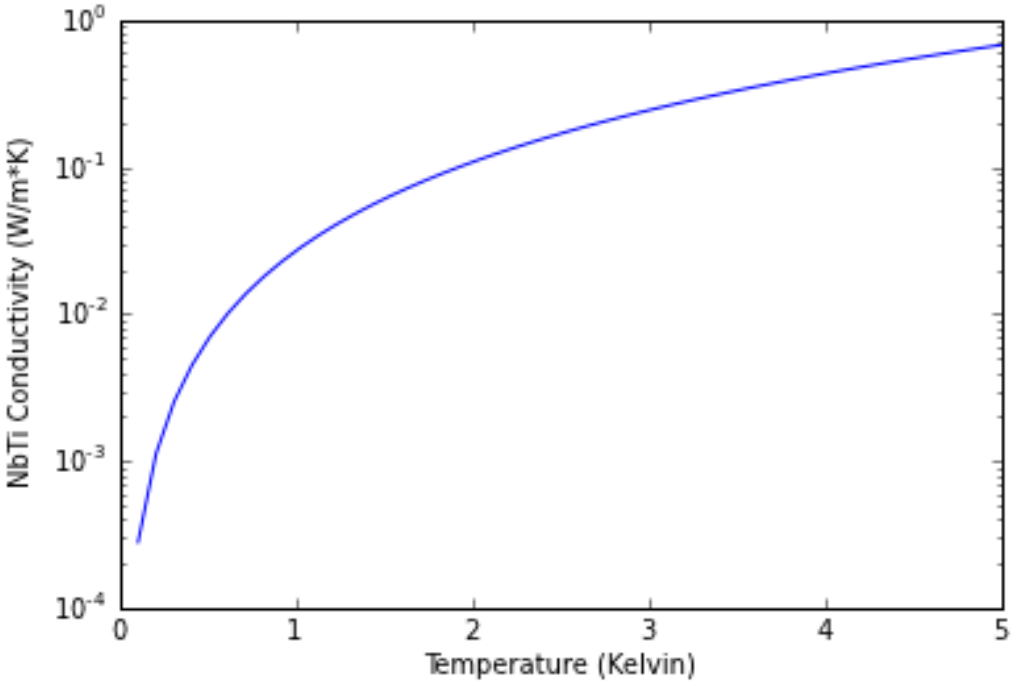

Figure 3.21: **Thermal conductivity of NbTi below 5 Kelvin** — The expected thermal conductivity of NbTi is shown for temperatures below 5 Kelvin, which is the range where it will be utilized in POLARBEAR-2. This is well below the critical temperature of NbTi, which is 10 Kelvin.

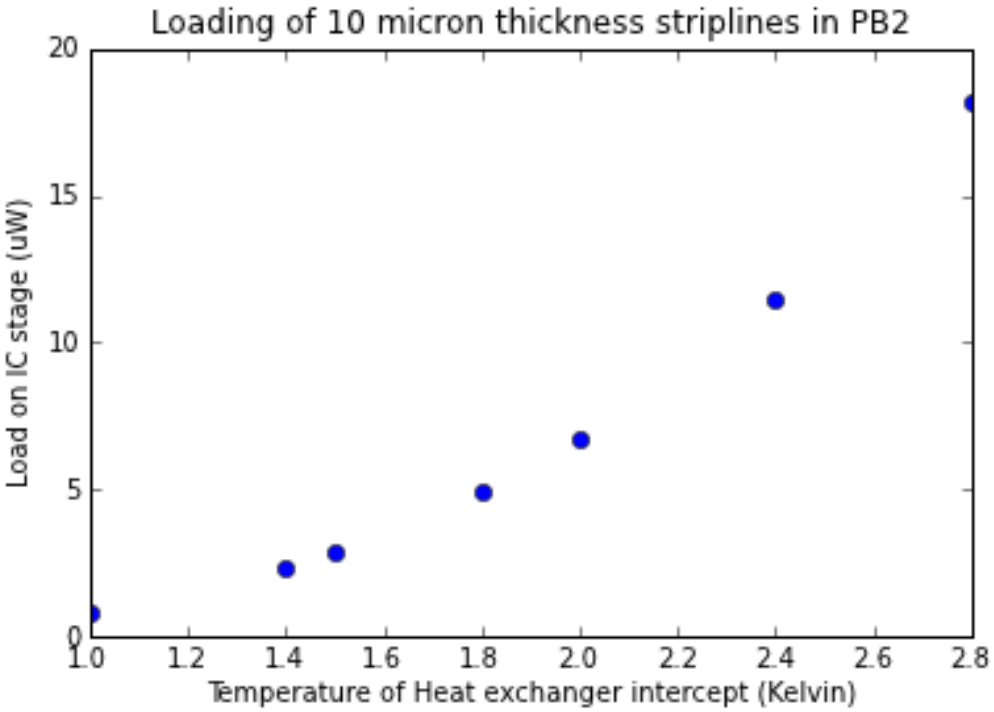

Figure 3.22: **Wiring contribution to thermal load on intermediate cold head** — The expected thermal load on the intermediate cold head is shown for a range of temperatures of the previous thermal intercept, the heat exchanger stage.

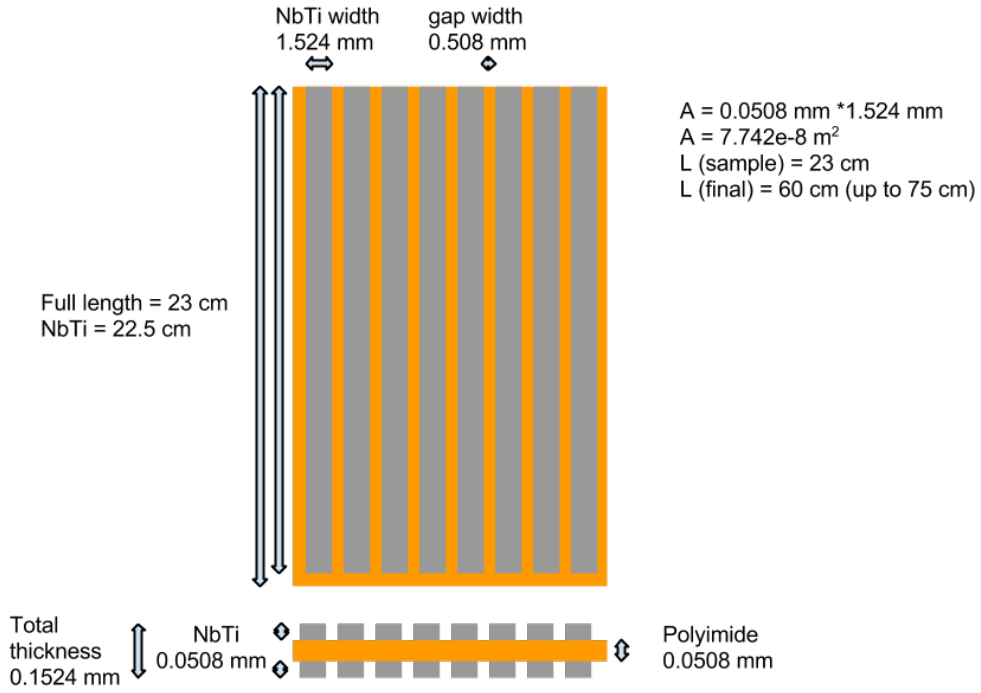

Figure 3.23: **Drawing of prototype NbTi stripline** — Drawing of prototype low-inductance NbTi stripline, which acts as both a zero-resistance connection between the SQUID and LC filters, as well as a thermal break to the cold focal plane.

This wiring will be commercially fabricated striplines with NbTi on a polyimide film Kapton®. The design of a prototype stripline with an expected inductance of $0.4nH/cm$, made by TechEtch, is shown in Figure 3.23. The current requirement for the POLARBEAR-2 wiring is a total inductance of 45 nH. These constraints will keep the stray inductance at an acceptable level for our readout bandwidth and channel spacing. The measured thermal conductance of this prototype is shown in Figure 3.24, along with the predicted conductance [77]. The contribution of the thin polyimide film to the thermal conductivity is negligible.

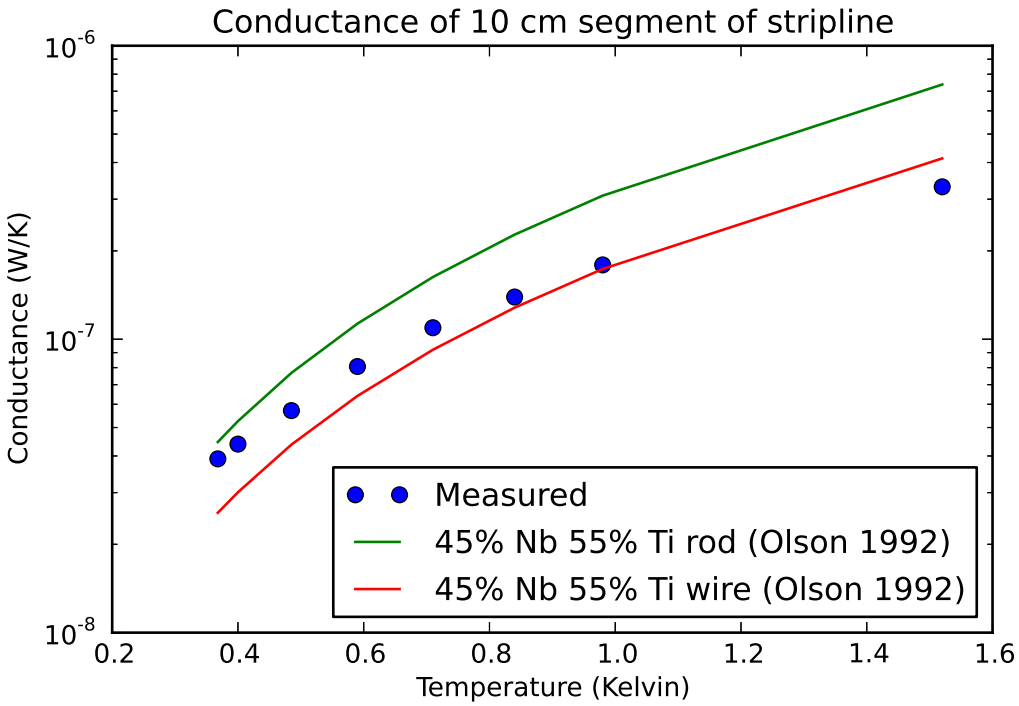

Figure 3.24: **Measured conductance of prototype NbTi stripline** — Measured conductance per 10 cm length of a prototype NbTi stripline (circles), along with the expected conductance given the geometry of the NbTi and two different values of conductivity from Olson 1993 [77].

3.4.2.5 Analog Signal Cables

The analog signals for frequency domain multiplexing must be carried across a length of cable from the receiver cryostat, mounted in the telescope, to the electronics that synthesize the carrier and nuller frequencies and demodulates the signals, located in a co-moving electronics enclosure. The cables that carry these signals required a significant re-design to work well with both the expanded readout bandwidth, as well as the new implementation of digital baseband feedback (DAN), described in Section 2.5. Signal crosstalk in the context of warm cables is mostly a concern for excessive noise. Crosstalk is especially problematic for DAN operation, which is sending a nulling signal based on the measured demodulator signal. Any additional pickup past the SQUID results in incorrect feedback, resulting in poor nulling and excess noise. To minimize crosstalk, these cables have a varying pitch in the different twisted pairs for a readout module, as well as shielding over the individual pairs. Each readout module also has a layer of shielding and insulation over it, to prevent coupling between similar pairs with the same twist pitch across modules. With this design, similar to the specifications for CAT-7 cable, the crosstalk between pairs was reduced to 60 dB (0.1%) across the frequency range of 100 KHz to 10 MHz, for a cable length of 5 meters. The two layers of inner shielding are foil, partly for space constraints with multiple layers of shielding, but also because foil has 100% coverage. The readout module shields are also foil, with a drain wire for grounding. Braid is bulkier and more expensive, has less even coverage, but is more effective at shielding, especially at lower frequencies, and it can be grounded directly, and so this is used for the overall cable shield. At the cryostat end, this shield is doubled back onto the metal backshell, which is connected to the RF box face plate, making a continuous RF shield with the entire length of cable shield, and the RF box.

3.4.3 Array Characterization

The POLARBEAR-2 design is an array with an NET of 4.1 $\mu\mathrm{K}\sqrt{\mathrm{s}}$ based on 7,588 detectors with an NET_{bolo} of 360 $\mu\mathrm{K}\sqrt{\mathrm{s}}$. Many factors can reduce the final array sensitivity, including excess noise and yield. The end-to-end readout system,

from warm electronics to cold components, is being validated before expanding to read out the entire array. The overall expected readout noise contribution is expected to be 7 pA$\sqrt{\text{Hz}}$. Detailed screening and characterization of components, including the SQUIDs and LC filters described above, is being performed at several institutions to select components for the final receiver. The detector wafers are also tested and screened to check that they meet the expected properties like saturation power and frequency band placement. A prototype wafer was tested at UC San Diego with the new LC components and squid controller with DAN operation, with a 15× multiplexing factor. The wafer setup in the test cryostat is shown in Figure 3.25, and bolometer IV curves are shown in Figure 3.26. The detectors must also be characterized in the integrated system for characteristics like stability and sensitivity. This process will be ongoing after the POLARBEAR-2 receiver is complete as we continue to commission the second and third Simons Array receivers.

The final array yield and sensitivity is determined by observations on the sky [39]. During observations, the SQUIDs are tuned daily during a cryogenic cycle, and the bolometers are typically tuned every hour to adjust for changing atmospheric conditions. Robust software that can use saved detector properties to quickly re-tune the entire array of detectors, without any user interaction, is important for observation efficiency. The stability of the detectors to changing power is also important, since detectors that go unstable and become superconducting due to fluctuations in atmospheric loading must be shut off until the next daily cryogenic cycle.

3.4.4 Conclusion

Development, construction, and testing of POLARBEAR-2 is ongoing at several institutions within the POLARBEAR collaboration. The full receiver will be assembled and characterized in the laboratory at KEK in Japan, before deploying to the Chilean site in 2016. The full complement of Simons Array receivers, described in Section 4.3 is expected to be complete in 2017.

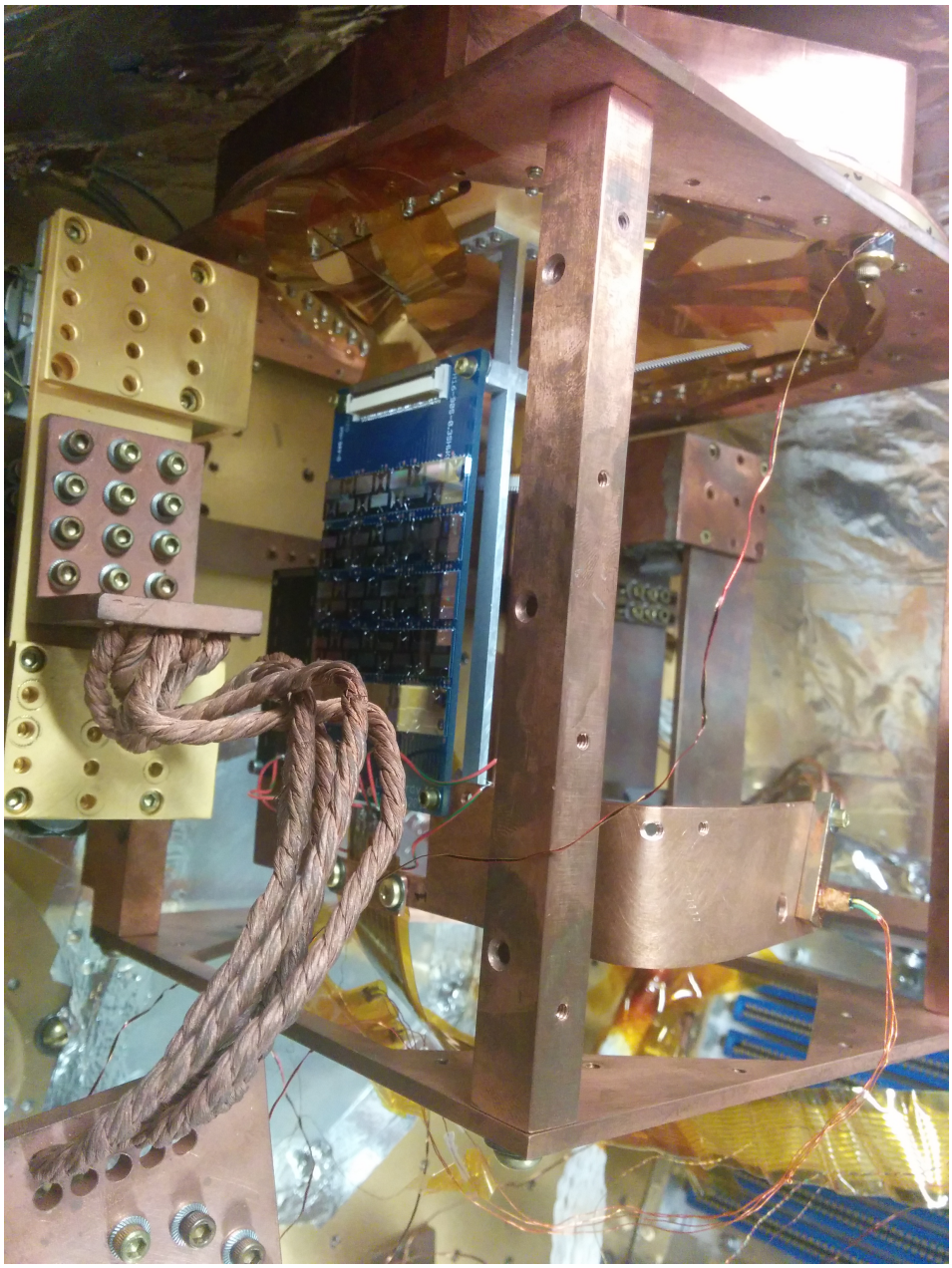

Figure 3.25: **UC San Diego Wafer Test Cryostat with POLARBEAR-2 Wafer** — Photograph of POLARBEAR-2 version 2 wafer installed in UC San Diego test cryostat for bolometer and readout testing. The six-inch diameter wafer is located at the top of the figure, facing up. The LC filters and NbTi cold cables are also visible.

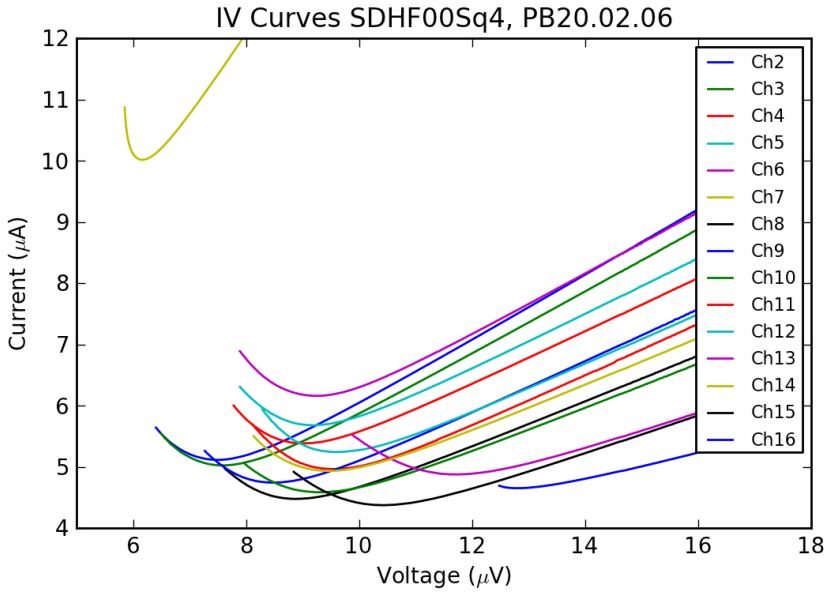

Figure 3.26: **IV curves for** 15× **comb of POLARBEAR-2 bolometers** — Measured IV curves overplotted for each bolometer with 15× multiplexing factor, using prototype low-loss LC filters and NbTi cold cables.

3.5 Acknowledgements

Section 3.2 is an updated reprint of material as it appears in: D. Barron, P. Ade, A. Anthony, K. Arnold, D. Boettger, J. Borrill, S. Chapman, Y. Chinone, M. Dobbs, J. Edwards, J. Errard, G. Fabbian, D. Flanigan, G. Fuller, A. Ghribi, W. Grainger, N. Halverson, M. Hasegawa, K. Hattori, M. Hazumi, W. Holzapfel, J. Howard, P. Hyland, G. Jaehnig, A. Jaffe, B. Keating, Z. Kermish, R. Keskitalo, T. Kisner, A. T. Lee, M. Le Jeune, E. Linder, M. Lungu, F. Matsuda, T. Matsumura, X. Meng, N. J. Miller, H. Morii, S. Moyerman, M. Meyers, H. Nishino, H. Paar, J. Peloton, E. Quealy, G. Rebeiz, C. L. Reichart, P. L. Richards, C. Ross, A. Shimizu, C. Shimmin, M. Shimon, M. Sholl, P. Siritanasak, H. Spieler, N. Stebor, B. Steinbach, R. Stompor, A. Suzuki, T. Tomaru, C. Tucker, A. Yadav, O. Zahn, The POLARBEAR Cosmic Microwave Background Polarization Experiment, published in J. Low Temp. Phys. Vol. 176, 5-6, pp 726-732, 2014, doi:10.1007/s10909-013-1065-5. The dissertation author was the primary author of this paper.

Figures 3.8 and 3.9 are reprints of material as it appears in: The POLARBEAR Collaboration: P. A. R. Ade, Y. Akiba, A. E. Anthony, K. Arnold, M. Atlas, D. Barron, D. Boettger, J. Borrill, S. Chapman, Y. Chinone, M. Dobbs, T. Elleflot, J. Errard, G. Fabbian, C. Feng, D. Flanigan, A. Gilbert, W. Grainger, N. W. Halverson, M. Hasegawa, K. Hattori, M. Hazumi, W. L. Holzapfel, Y. Hori, J. Howard, P. Hyland, Y. Inoue, G. C. Jaehnig, A. H. Jaffe, B. Keating, Z. Kermish, R. Keskitalo, T. Kisner, M. Le Jeune, A. T. Lee, E. M. Leitch, E. Linder, M. Lungu, F. Matsuda, T. Matsumura, X. Meng, N. J. Miller, H. Morii, S. Moyerman, M. J. Myers, M. Navaroli, H. Nishino, H. Paar, J. Peloton, D. Poletti, E. Quealy, G. Rebeiz, C. L. Reichardt, P. L. Richards, C. Ross, I. Schanning, D. E. Schenck, B. D. Sherwin, A. Shimizu, C. Shimmin, M. Shimon, P. Siritanasak, G. Smecher, H. Spieler, N. Stebor, B. Steinbach, R. Stompor, A. Suzuki, S. Takakura, T. Tomaru, B. Wilson, A. Yadav, and O. Zahn, A Measurement of the Cosmic Microwave Background B-mode Polarization Power Spectrum at Sub-degree Scales with POLARBEAR, ApJ 794, 171 , 2014. The dissertation author made essential contributions to many aspects of this work.

Section 3.4 is an updated and expanded reprint of the material as it appears in: D. Barron, P. A. R. Ade, Y. Akiba, C. Aleman, K. Arnold, M. Atlas, A. Bender, J. Borrill, S. Chapman, Y. Chinone, A. Cukierman, M. Dobbs, T. Elleflot, J. Errard, G. Fabbian, G. Feng, A. Gilbert, N. W. Halverson, M. Hasegawa, K. Hattori, M. Hazumi, W. L. Holzapfel, Y. Hori, Y. Inoue, G. C. Jaehnig, N. Katayama, B. Keating, Z. Kermish, R. Keskitalo, T. Kisner, M. Le Jeune, A. T. Lee, F. Matsuda, T. Matsumura, H. Morii, M. J. Myers, M. Navroli, H. Nishino, T. Okamura, J. Peloton, G. Rebeiz, C. L. Reichardt, P. L. Richards, C. Ross, M. Sholl, P. Siritanasak, G. Smecher, N. Stebor, B. Steinbach, R. Stompor, A. Suzuki, J. Suzuki, S. Takada, T. Takakura, T. Tomaru, B. Wilson, H. Yamaguchi, O. Zahn, Development and characterization of the readout system for POLARBEAR-2, published in the Proceedings of SPIE 9153: Millimeter, Submillimeter, and Far-Infrared Detectors and Instrumentation for Astronomy VII, 915335, 2014, doi:10.1117/12.2055611. The dissertation author was the primary author of this paper.

Chapter 4

Conclusions and Future Outlook

4.1 Introduction

The field of CMB polarization measurements has made rapid progress over the past decade, with the sensitivity of several experiments finally reaching the level to measure B-mode polarization signals [59, 55, 54, 80, 56]. The measurement of B-mode polarization at small angular scales, generated by gravitational lensing of the CMB, is both a milestone in sensitivity and a demonstration of a powerful new probe to study the CMB. The measurement of B-mode power at large angular scales by BICEP2 [80], which was shown to be consistent with the level expected from galactic dust emission [81], highlighted the need for more spectral information from the next generation of CMB experiments. A convincing detection of the primordial B-mode signal from inflation will require a measurement of its frequency spectrum, showing that it is consistent with the CMB blackbody spectrum, as well as measurements of the signal across the sky, demonstrating that it is a cosmological signal. In this chapter, we review the recent CMB B-mode measurements and the state of the field, and discuss upcoming experiments and beyond. In Section 4.2, we review the current state of the field in 2015. In Section 4.3, we discuss the prospects for Simons Array, the expansion of the POLARBEAR site with POLARBEAR-2 as the first new receiver. Finally in Section 4.4 we discuss the future of the field and the instruments and measurements beyond the next generation of CMB experiments.

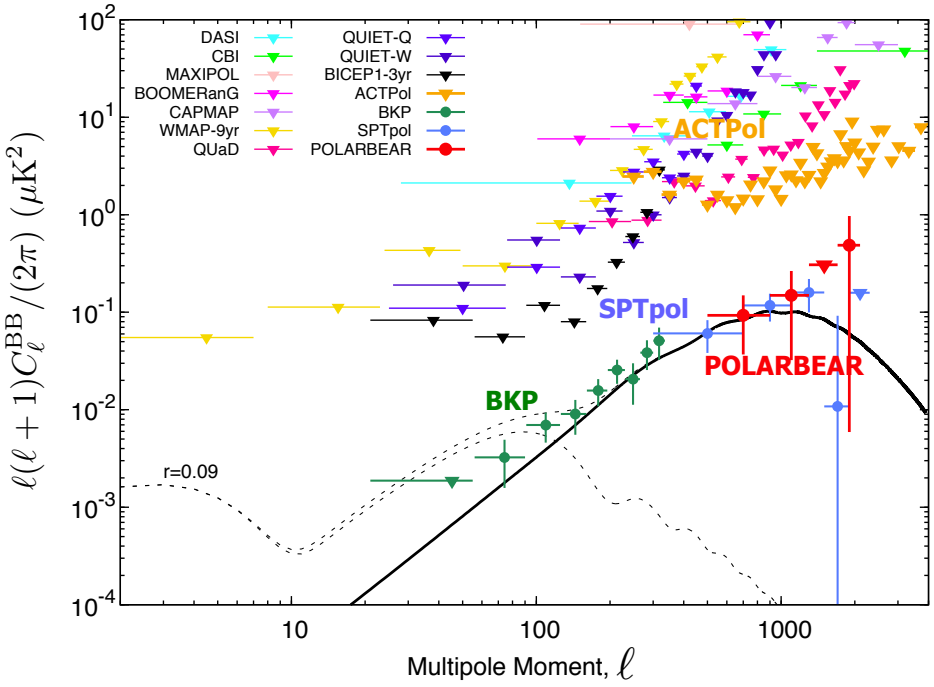

Figure 4.1: **Current CMB B-mode polarization power spectrum measurements** — Current CMB B-mode polarization power spectrum measurements (as of May 2015) are shown, including the dust-subtracted points from the joint BICEP2-Planck analysis (BKP)[61]. The expected gravitational lensing signal is shown with the solid black line. The predicted inflationary signal for $r = 0.09$ is shown with the lower dashed line, which is consistent with the measured points from BKP[61]. (Figure courtesy of Yuji Chinone) [56, 82, 60, 61, 58]

4.2 Current State of the Field

The POLARBEAR-1 results discussed in Section 3.3 were just part of an exciting year for the CMB field, with results from several other experiments also confirming the B-mode lensing signal [59, 61, 60, 15]. The measurements of C_ℓ^{BB} are an impressive milestone in sensitivity, as shown in Figure 4.1, coming after a decade of experiments setting upper limits on the signal. While BICEP2 announced a detection of B-mode polarization at large angular scales arising from inflation [80], based on deep observations of a single patch of the sky at 150 GHz, there was immediate skepticism about the origin of the signal. As of 2014 when BICEP2 first released their results, there was still essentially no measurements of the polarization signal from Galactic dust at millimeter wavelengths, only models

based on measurements of its millimeter-wavelength emission, and the intensity and polarization properties of starlight absorbed by the same galactic dust [83]. The long-awaited Planck all-sky polarization results started to be released in 2015, giving us broader spectral and spatial information about the CMB signal and astrophysical foregrounds. The Planck data include all-sky polarization observations at 353 GHz, a frequency where the dust intensity is greater than the CMB intensity for most of the sky, and the characteristics of dust emission can be studied.

Combining Planck's broader maps with the BICEP2 deep observations at 150 GHz enabled tight constraints on the inflationary portion of the B-mode polarization signal seen by BICEP2, placing a constraint on the tensor-to-scalar ratio $r < 0.12$ at 95% confidence [61]. For perspective, this is still a looser constraint on r than had already been in place from CMB temperature data from Planck, SPT, and ACT, and WMAP low-frequency polarization data, $r < 0.11$. This highlights the challenge that B-mode polarization measurements will face with disentangling the effect of polarized foregrounds. From recent measurements, it appears that the BICEP2 patch was not as "clean" of foreground contamination as expected, and there might be slightly cleaner patches of the sky available with lower dust polarization power. However, the full measurement of the B-mode polarization will require maps across the entire sky, with foreground modeling and subtraction, just as was done for CMB temperature maps, in order to fully characterize the signal and extract cosmology and physics from it.

The next generation of ground-based CMB instruments that are preparing to deploy have already anticipated the need for broader spectral coverage and broader sky coverage, including POLARBEAR-2, discussed in Chapter 3.4, Advanced ACTPol [46], SPT3G [84], and CLASS [85]. These experiments will rely on the rapid improvements in array sensitivity from scaling up pixel count in order to map much larger fractions of the sky to the same level of sensitivity as the current generation of experiments mapped the small patches that generated the initial B-mode results. There has also been much development work in designing broader bandwidth instruments, including multichroic pixels, to gain additional spectral channels. The experiments must have high enough resolution to measure

the gravitational lensing signal at small scales, both to fully characterize it as well as to use this information to de-lens the inflationary B-mode signal.

4.3 The Simons Array

The Simons Array is the POLARBEAR collaboration's next-generation CMB instrument, which is an expansion of the POLARBEAR site to three telescopes. By leveraging our existing designs for a relatively compact telescope and the POLARBEAR-2 receiver with a large dichroic array (described in Chapter 3.4), the Simons Array will rapidly increase our sensitivity. The two additional telescopes are under construction now for delivery at the end of 2015. These telescopes will be identical to the Huan Tran Telescope except for minor design changes. POLARBEAR-2 will deploy onto the first of these new telescopes, and an identical copy of POLARBEAR-2 will deploy onto the second telescope soon afterwards. These two receivers will have dichroic focal planes observing at 90 and 150 GHz. Once these two telescopes and receivers have begun observations, POLARBEAR-1 will be decommissioned and replaced with a new receiver, similar to POLARBEAR-2, but with a multi-chroic focal plane with a higher frequency band to measure dust polarization. This receiver is under development now. Making sensitive polarization maps at higher frequencies where dust dominates is important for understanding the spectral signature of foregrounds across the sky. The Simons Array has access to over 80% of the sky from its mid-latitude site, with a minimum observing elevation of 30 degrees. The baseline plan is to survey 65% of the sky, based on a survey area that includes the regions of the sky with the least galactic contamination. The Simons Array spectral information will be combined with external data sets like Planck and C-BASS to separate and remove foregrounds from the CMB signal.

4.4 Future Outlook

While the next generation of CMB instruments, which are preparing to deploy in the next few years, will make important steps in charactering the B-mode lensing signal, there still could be a long search ahead for the faint inflationary B-mode signal. The following generation is expected to reach the ultimate limit of ground-based instrumentation. This hypothetical experiment, called "CMB-Stage 4", is in the initial planning stages now. It has been described in white papers[86, 87], and has been recommended by Congress for DOE funding. The community's goal for CMB-S4 is to fully characterize the gravitational lensing signal, tightly constraining the sum of the neutrino masses, and also do as deep of a search as possible from the ground for the inflationary signal. This will require hundreds of thousands of detectors, with broad spectral coverage, observing at least 50% of the sky at a resolution of 3 arcminutes.

While the sensitivity of a ground-based instrument can be improved by scaling up detector count, there are still hard limits to the frequency bands accessible from the ground, which are defined by the atmospheric transmission bands. Fully characterizing a complex foreground signal to measure an extremely faint inflationary B-mode signal could require more spectral information that is only available to a space-based instrument. Characterizing the CMB on the largest scales is also extremely difficult from the ground, and satellites have scan strategy and stability benefits that can result in stable, long scans of the sky with very low $1/f$ noise. There is also interesting physics in re-examining potential spectral distortions in the frequency spectrum of the CMB[88], last measured by FIRAS[8], which could only be done from space. There are preliminary proposals for a CMB B-mode satellite that would be a joint mission with JAXA and NASA, called LiteBIRD, as well as a spectral characterization satellite, PIXIE, among other potential space-based missions that are in the discussion phase.

4.5 Acknowledgements

Figure 4.1 was provided by Yuji Chinone.

References

[1] Penzias, A. A. and Wilson, R. W., "A Measurement of Excess Antenna Temperature at 4080 Mc/s.," *ApJ* **142**, 419–421 (July 1965).

[2] Hubble, E., "A relation between distance and radial velocity among extragalactic nebulae," *Proceedings of the National Academy of Sciences* **15**(3), 168–173 (1929).

[3] Dicke, R. H., Peebles, P. J. E., Roll, P. G., and Wilkinson, D. T., "Cosmic Black-Body Radiation.," *ApJ* **142**, 414–419 (July 1965).

[4] Alpher, R. A., Bethe, H., and Gamow, G., "The origin of chemical elements," *Phys. Rev.* **73**, 803–804 (Apr 1948).

[5] Riess, A. G., Filippenko, A. V., Challis, P., Clocchiatti, A., Diercks, A., Garnavich, P. M., Gilliland, R. L., Hogan, C. J., Jha, S., Kirshner, R. P., Leibundgut, B., Phillips, M. M., Reiss, D., Schmidt, B. P., Schommer, R. A., Smith, R. C., Spyromilio, J., Stubbs, C., Suntzeff, N. B., and Tonry, J., "Observational Evidence from Supernovae for an Accelerating Universe and a Cosmological Constant," *AJ* **116**, 1009–1038 (Sept. 1998).

[6] Eisenstein, D. J., Zehavi, I., Hogg, D. W., Scoccimarro, R., Blanton, M. R., Nichol, R. C., Scranton, R., Seo, H.-J., Tegmark, M., Zheng, Z., Anderson, S. F., Annis, J., Bahcall, N., Brinkmann, J., Burles, S., Castander, F. J., Connolly, A., Csabai, I., Doi, M., Fukugita, M., Frieman, J. A., Glazebrook, K., Gunn, J. E., Hendry, J. S., Hennessy, G., Ivezić, Z., Kent, S., Knapp, G. R., Lin, H., Loh, Y.-S., Lupton, R. H., Margon, B., McKay, T. A., Meiksin, A., Munn, J. A., Pope, A., Richmond, M. W., Schlegel, D., Schneider, D. P., Shimasaku, K., Stoughton, C., Strauss, M. A., SubbaRao, M., Szalay, A. S., Szapudi, I., Tucker, D. L., Yanny, B., and York, D. G., "Detection of the Baryon Acoustic Peak in the Large-Scale Correlation Function of SDSS Luminous Red Galaxies," *ApJ* **633**, 560–574 (Nov. 2005).

[7] Spergel, D. N., Bean, R., DorÃľ, O., Nolta, M. R., Bennett, C. L., Dunkley, J., Hinshaw, G., Jarosik, N., Komatsu, E., Page, L., Peiris, H. V., Verde, L., Halpern, M., Hill, R. S., Kogut, A., Limon, M., Meyer, S. S., Odegard, N.,

Tucker, G. S., Weiland, J. L., Wollack, E., and Wright, E. L., "Three-year wilkinson microwave anisotropy probe (wmap) observations: Implications for cosmology," *The Astrophysical Journal Supplement Series* **170**(2), 377 (2007).

[8] Mather, J. C., Cheng, E. S., Cottingham, D. A., Eplee, Jr., R. E., Fixsen, D. J., Hewagama, T., Isaacman, R. B., Jensen, K. A., Meyer, S. S., Noerdlinger, P. D., Read, S. M., Rosen, L. P., Shafer, R. A., Wright, E. L., Bennett, C. L., Boggess, N. W., Hauser, M. G., Kelsall, T., Moseley, Jr., S. H., Silverberg, R. F., Smoot, G. F., Weiss, R., and Wilkinson, D. T., "Measurement of the cosmic microwave background spectrum by the COBE FIRAS instrument," *ApJ* **420**, 439–444 (Jan. 1994).

[9] Ryden, B., [*Introduction to Cosmology*], Addison-Wesley (2003).

[10] Planck Collaboration, Ade, P. A. R., Aghanim, N., Arnaud, M., Ashdown, M., Aumont, J., Baccigalupi, C., Banday, A. J., Barreiro, R. B., Bartlett, J. G., and et al., "Planck 2015 results. XIII. Cosmological parameters," *ArXiv e-prints* (Feb. 2015).

[11] Guth, A. H., "Inflationary universe: A possible solution to the horizon and flatness problems," *Phys. Rev. D* **23**, 347–356 (Jan 1981).

[12] Spergel, D. N., "The dark side of cosmology: Dark matter and dark energy," *Science* **347**(6226), 1100–1102 (2015).

[13] Hu, W. and Dodelson, S., "Cosmic Microwave Background Anisotropies," *ARA&A* **40**, 171–216 (2002).

[14] Lewis, A., Challinor, A., and Lasenby, A., "Efficient computation of CMB anisotropies in closed FRW models," *Astrophys. J.* **538**, 473–476 (2000).

[15] Planck Collaboration, Ade, P. A. R., Aghanim, N., Arnaud, M., Ashdown, M., Aumont, J., Baccigalupi, C., Banday, A. J., Barreiro, R. B., Bartlett, J. G., and et al., "Planck 2015 results. XV. Gravitational lensing," *ArXiv e-prints* (Feb. 2015).

[16] Arnold, K., Stebor, N., Ade, P. A. R., Akiba, Y., Anthony, A. E., Atlas, M., Barron, D., Bender, A., Boettger, D., Borrill, J., Chapman, S., Chinone, Y., Cukierman, A., Dobbs, M., Elleflot, T., Errard, J., Fabbian, G., Feng, C., Gilbert, A., Goeckner-Wald, N., Halverson, N. W., Hasegawa, M., Hattori, K., Hazumi, M., Holzapfel, W. L., Hori, Y., Inoue, Y., Jaehnig, G. C., Jaffe, A. H., Katayama, N., Keating, B., Kermish, Z., Keskitalo, R., Kisner, T., Le Jeune, M., Lee, A. T., Leitch, E. M., Linder, E., Matsuda, F., Matsumura, T., Meng, X., Miller, N. J., Morii, H., Myers, M. J., Navaroli, M., Nishino, H., Okamura, T., Paar, H., Peloton, J., Poletti, D., Raum, C., Rebeiz, G., Reichardt, C. L., Richards, P. L., Ross, C., Rotermund, K. M., Schenck, D. E.,

Sherwin, B. D., Shirley, I., Sholl, M., Siritanasak, P., Smecher, G., Steinbach, B., Stompor, R., Suzuki, A., Suzuki, J., Takada, S., Takakura, S., Tomaru, T., Wilson, B., Yadav, A., and Zahn, O., "The Simons Array: expanding POLARBEAR to three multi-chroic telescopes," in [*Society of Photo-Optical Instrumentation Engineers (SPIE) Conference Series*], *Society of Photo-Optical Instrumentation Engineers (SPIE) Conference Series* **9153**, 1 (Aug. 2014).

[17] Pardo, J., Cernicharo, J., and Serabyn, E., "Atmospheric transmission at microwaves (atm): an improved model for millimeter/submillimeter applications," *Antennas and Propagation, IEEE Transactions on* **49**, 1683–1694 (Dec 2001).

[18] Samtleben, D., Staggs, S., and Winstein, B., "The Cosmic Microwave Background for Pedestrians: A Review for Particle and Nuclear Physicists," *Annual Review of Nuclear and Particle Science* **57**, 245–283 (Nov. 2007).

[19] Fosalba, P., Lazarian, A., Prunet, S., and Tauber, J. A., "Statistical Properties of Galactic Starlight Polarization," *ApJ* **564**, 762–772 (Jan. 2002).

[20] Planck Collaboration, Ade, P. A. R., Aghanim, N., Alina, D., Alves, M. I. R., Armitage-Caplan, C., Arnaud, M., Arzoumanian, D., Ashdown, M., Atrio-Barandela, F., and et al., "Planck intermediate results. XIX. An overview of the polarized thermal emission from Galactic dust," *A&A* **576**, A104 (Apr. 2015).

[21] Wiebe, D. S. and Watson, W. D., "Irregular magnetic fields and the far-infrared polarimetry of dust emission from interstellar clouds," *The Astrophysical Journal* **615**(1), 300 (2004).

[22] Dunkley, J., Spergel, D. N., Komatsu, E., Hinshaw, G., Larson, D., Nolta, M. R., Odegard, N., Page, L., Bennett, C. L., Gold, B., Hill, R. S., Jarosik, N., Weiland, J. L., Halpern, M., Kogut, A., Limon, M., Meyer, S. S., Tucker, G. S., Wollack, E., and Wright, E. L., "Five-year wilkinson microwave anisotropy probe (wmap) observations: Bayesian estimation of cosmic microwave background polarization maps," *ApJ* **701**(2), 1804 (2009).

[23] Bennett, C. L., Hill, R. S., Hinshaw, G., Nolta, M. R., Odegard, N., Page, L., Spergel, D. N., Weiland, J. L., Wright, E. L., Halpern, M., Jarosik, N., Kogut, A., Limon, M., Meyer, S. S., Tucker, G. S., and Wollack, E., "First-year wilkinson microwave anisotropy probe (wmap) observations: Foreground emission," *The Astrophysical Journal Supplement Series* **148**(1), 97 (2003).

[24] Planck Collaboration, Adam, R., Ade, P. A. R., Aghanim, N., Alves, M. I. R., Arnaud, M., Ashdown, M., Aumont, J., Baccigalupi, C., Banday, A. J., and et al., "Planck 2015 results. X. Diffuse component separation: Foreground

maps," *ArXiv e-prints* (Feb. 2015).

[25] Pietranera, L., Buehler, S. A., Calisse, P. G., Emde, C., Hayton, D., Oommen John, V., Maffei, B., Piccirillo, L., Pisano, G., Savini, G., and Sreerekha, T. R., "Observing cosmic microwave background polarization through ice," *Monthly Notices of the Royal Astronomical Society* **376**(2), 645–650 (2007).

[26] Irwin, K. and Hilton, G., "Transition-edge sensors," in [*Cryogenic Particle Detection*], Enss, C., ed., *Topics in Applied Physics* **99**, 63–150, Springer Berlin Heidelberg (2005).

[27] Richards, P. L., "Bolometers for infrared and millimeter waves," *Journal of Applied Physics* **76**, 1–24 (July 1994).

[28] Lanting, T., *Multiplexed Readout of Superconducting Bolometers for Cosmological Observations*, PhD thesis, UC Berkeley (2006).

[29] Arnold, K., *Design and Deployment of the Polarbear Cosmic Microwave Background Polarization Experiment*, PhD thesis, UC Berkeley (2010).

[30] Mather, J. C., "Bolometer noise: nonequilibrium theory," *Appl. Opt.* **21**, 1125–1129 (Mar 1982).

[31] Braginski, A. I. and Clarke, J., eds., [*The SQUID Handbook*], Wiley-VCH Verlag GmbH Co. KGaA (2005).

[32] Dobbs, M. A., Lueker, M., Aird, K. A., Bender, A. N., Benson, B. A., Bleem, L. E., Carlstrom, J. E., Chang, C. L., Cho, H.-M., Clarke, J., Crawford, T. M., Crites, A. T., Flanigan, D. I., de Haan, T., George, E. M., Halverson, N. W., Holzapfel, W. L., Hrubes, J. D., Johnson, B. R., Joseph, J., Keisler, R., Kennedy, J., Kermish, Z., Lanting, T. M., Lee, A. T., Leitch, E. M., Luong-Van, D., McMahon, J. J., Mehl, J., Meyer, S. S., Montroy, T. E., Padin, S., Plagge, T., Pryke, C., Richards, P. L., Ruhl, J. E., Schaffer, K. K., Schwan, D., Shirokoff, E., Spieler, H. G., Staniszewski, Z., Stark, A. A., Vanderlinde, K., Vieira, J. D., Vu, C., Westbrook, B., and Williamson, R., "Frequency multiplexed superconducting quantum interference device readout of large bolometer arrays for cosmic microwave background measurements," *Rev. Sci. Instrum.* **83**(7), 073113 (2012).

[33] Drung, D., Hinnrichs, C., and Barthelmess, H.-J., "Low-noise ultra-high-speed dc squid readout electronics," *Superconductor Science and Technology* **19**(5), S235 (2006).

[34] Radebaugh, R., "Pulse tube cryocoolers for cooling infrared sensors," *Proc. SPIE* **4130**, 363–379 (2000).

[35] Radebaugh, R., "Development of the pulse tube refrigerator as an efficient and reliable cryocooler," *Proc. Institute of Refrigeration* (1999).

[36] Lienerth, C., Thummes, G., and Heiden, C., "Progress in low noise cooling performance of a pulse-tube cooler for ht-squid operation," *Applied Superconductivity, IEEE Transactions on* **11**, 812–815 (Mar 2001).

[37] Rijpma, A., Bangma, M., Reincke, H., de Vries, E., Holland, H., ter Brake, H., and Rogalla, H., "Interference characterization of cryocoolers for a high-tc squid-based fetal heart monitor," in [*Cryocoolers 11*], Ross, R.G., J., ed., 793–802, Springer US (2002).

[38] Hohmann, R., Lienerth, C., Zhang, Y., Bousack, H., Thummes, G., and Heiden, C., "Comparison of low noise cooling performance of a joule-thomson cooler and a pulse-tube cooler using a ht squid," *Applied Superconductivity, IEEE Transactions on* **9**, 3688–3691 (June 1999).

[39] Kermish, Z. D., Ade, P., Anthony, A., Arnold, K., Barron, D., Boettger, D., Borrill, J., Chapman, S., Chinone, Y., Dobbs, M. A., Errard, J., Fabbian, G., Flanigan, D., Fuller, G., Ghribi, A., Grainger, W., Halverson, N., Hasegawa, M., Hattori, K., Hazumi, M., Holzapfel, W. L., Howard, J., Hyland, P., Jaffe, A., Keating, B., Kisner, T., Lee, A. T., Le Jeune, M., Linder, E., Lungu, M., Matsuda, F., Matsumura, T., Meng, X., Miller, N. J., Morii, H., Moyerman, S., Myers, M. J., Nishino, H., Paar, H., Quealy, E., Reichardt, C. L., Richards, P. L., Ross, C., Shimizu, A., Shimon, M., Shimmin, C., Sholl, M., Siritanasak, P., Spieler, H., Stebor, N., Steinbach, B., Stompor, R., Suzuki, A., Tomaru, T., Tucker, C., and Zahn, O., "The POLARBEAR experiment," *Proc. SPIE* **8452**, 84521C–84521C–15 (2012).

[40] Ruhl, J., Ade, P. A. R., Carlstrom, J. E., Cho, H.-M., Crawford, T., Dobbs, M., Greer, C. H., Halverson, N. w., Holzapfel, W. L., Lanting, T. M., Lee, A. T., Leitch, E. M., Leong, J., Lu, W., Lueker, M., Mehl, J., Meyer, S. S., Mohr, J. J., Padin, S., Plagge, T., Pryke, C., Runyan, M. C., Schwan, D., Sharp, M. K., Spieler, H., Staniszewski, Z., and Stark, A. A., "The south pole telescope," *Proc. SPIE* **5498**, 11–29 (2004).

[41] Arnold, K., Ade, P. A. R., Anthony, A. E., Aubin, F., Boettger, D., Borrill, J., Cantalupo, C., Dobbs, M. A., Errard, J., Flanigan, D., Ghribi, A., Halverson, N., Hazumi, M., Holzapfel, W. L., Howard, J., Hyland, P., Jaffe, A., Keating, B., Kisner, T., Kermish, Z., Lee, A. T., Linder, E., Lungu, M., Matsumura, T., Miller, N., Meng, X., Myers, M., Nishino, H., O'Brient, R., O'Dea, D., Paar, H., Reichardt, C., Schanning, I., Shimizu, A., Shimmin, C., Shimon, M., Spieler, H., Steinbach, B., Stompor, R., Suzuki, A., Tomaru, T., Tran, H. T., Tucker, C., Quealy, E., Richards, P. L., and Zahn, O., "The POLARBEAR CMB polarization experiment," *Proc. SPIE* **7741**, 77411E–77411E–11 (2010).

[42] Runyan, M. and Jones, W., "Thermal conductivity of thermally-isolating polymeric and composite structural support materials between 0.3 and 4xa0;k," *Cryogenics* **48**(9âĂŞ10), 448 – 454 (2008).

[43] SchÃűne, S., MÃijck, M., Thummes, G., and Heiden, C., "Investigation of the response of superconducting quantum interference devices to temperature variation," *Review of Scientific Instruments* **68**(1), 85–88 (1997).

[44] Chijioke, A. and Lawall, J., "Vibration spectrum of a pulse-tube cryostat from 1xa0;hz to 20xa0;khz," *Cryogenics* **50**(4), 266 – 270 (2010).

[45] BICEP2 Collaboration, Ade, P. A. R., Aikin, R. W., Barkats, D., Benton, S. J., Bischoff, C. A., Bock, J. J., Brevik, J. A., Buder, I., Bullock, E., Dowell, C. D., Duband, L., Filippini, J. P., Fliescher, S., Golwala, S. R., Halpern, M., Hasselfield, M., Hildebrandt, S. R., Hilton, G. C., Irwin, K. D., Karkare, K. S., Kaufman, J. P., Keating, B. G., Kernasovskiy, S. A., Kovac, J. M., Kuo, C. L., Leitch, E. M., Lueker, M., Netterfield, C. B., Nguyen, H. T., O'Brient, R., Ogburn, IV, R. W., Orlando, A., Pryke, C., Richter, S., Schwarz, R., Sheehy, C. D., Staniszewski, Z. K., Sudiwala, R. V., Teply, G. P., Tolan, J. E., Turner, A. D., Vieregg, A. G., Wong, C. L., and Yoon, K. W., "BICEP2 III: Instrumental Systematics," *ArXiv e-prints* (Feb. 2015).

[46] Niemack, M. and ACTPol Collaboration, "ACTPol: A New Instrument to Measure CMB Polarization with the Atacama Cosmology Telescope," in [*American Astronomical Society Meeting Abstracts #221*], *American Astronomical Society Meeting Abstracts* **221**, 105.04 (Jan. 2013).

[47] Hanany, S., Jaffe, a. H., and Scannapieco, E., "The Effect of the Detector Response Time on Bolometric Cosmic Microwave Background Anisotropy Experiments," **000**(April), 9 (1998).

[48] de Haan, T., Smecher, G., and Dobbs, M., "Improved performance of tes bolometers using digital feedback," *Proc. SPIE* **8452**, 84520E–84520E–10 (2012).

[49] Bender, A. N., Cliche, J.-F., de Haan, T., Dobbs, M. A., Gilbert, A. J., Montgomery, J., Rowlands, N., Smecher, G. M., Smith, K., and Wilson, A., "Digital frequency domain multiplexing readout electronics for the next generation of millimeter telescopes," (2014).

[50] Errard, J., Ade, P. A. R., Akiba, Y., Arnold, K., Atlas, M., Baccigalupi, C., Barron, D., Boettger, D., Borrill, J., Chapman, S., Chinone, Y., Cukierman, A., Delabrouille, J., Dobbs, M., Ducout, A., Elleflot, T., Fabbian, G., Feng, C., Feeney, S., Gilbert, A., Goeckner-Wald, N., Halverson, N. W., Hasegawa, M., Hattori, K., Hazumi, M., Hill, C., Holzapfel, W. L., Hori, Y., Inoue, Y.,

Jaehnig, G. C., Jaffe, A. H., Jeong, O., Katayama, N., Kaufman, J., Keating, B., Kermish, Z., Keskitalo, R., Kisner, T., Le Jeune, M., Lee, A. T., Leitch, E. M., Leon, D., Linder, E., Matsuda, F., Matsumura, T., Miller, N. J., Myers, M. J., Navaroli, M., Nishino, H., Okamura, T., Paar, H., Peloton, J., Poletti, D., Puglisi, G., Rebeiz, G., Reichardt, C. L., Richards, P. L., Ross, C., Rotermund, K. M., Schenck, D. E., Sherwin, B. D., Siritanasak, P., Smecher, G., Stebor, N., Steinbach, B., Stompor, R., Suzuki, A., Tajima, O., Takakura, S., Tikhomirov, A., Tomaru, T., Whitehorn, N., Wilson, B., Yadav, A., and Zahn, O., "Atmospheric contamination for CMB ground-based observations," *ArXiv e-prints* (Jan. 2015).

[51] Zmuidzinas, J., "Thermal noise and correlations in photon detection," *Appl. Opt.* **42**, 4989–5008 (Sep 2003).

[52] Arnold, K., Ade, P. A. R., Anthony, A. E., Barron, D., Boettger, D., Borrill, J., Chapman, S., Chinone, Y., Dobbs, M. A., Errard, J., Fabbian, G., Flanigan, D., Fuller, G., Ghribi, A., Grainger, W., Halverson, N., Hasegawa, M., Hattori, K., Hazumi, M., Holzapfel, W. L., Howard, J., Hyland, P., Jaffe, A., Keating, B., Kermish, Z., Kisner, T., Le Jeune, M., Lee, A. T., Linder, E., Lungu, M., Matsuda, F., Matsumura, T., Miller, N. J., Meng, X., Morii, H., Moyerman, S., Myers, M. J., Nishino, H., Paar, H., Quealy, E., Reichardt, C., Richards, P. L., Ross, C., Shimizu, A., Shimmin, C., Shimon, M., Sholl, M., Siritanasak, P., Speiler, H., Stebor, N., Steinbach, B., Stompor, R., Suzuki, A., Tomaru, T., Tucker, C., and Zahn, O., "The bolometric focal plane array of the POLARBEAR CMB experiment," *Proc. SPIE* **8452**, 84521D–84521D–12 (2012).

[53] Barron, D., Ade, P., Anthony, A., Arnold, K., Boettger, D., Borrill, J., Chapman, S., Chinone, Y., Dobbs, M., Edwards, J., Errard, J., Fabbian, G., Flanigan, D., Fuller, G., Ghribi, A., Grainger, W., Halverson, N., Hasegawa, M., Hattori, K., Hazumi, M., Holzapfel, W., Howard, J., Hyland, P., Jaehnig, G., Jaffe, A., Keating, B., Kermish, Z., Keskitalo, R., Kisner, T., Lee, A. T., Le Jeune, M., Linder, E., Lungu, M., Matsuda, F., Matsumura, T., Meng, X., Miller, N. J., Morii, H., Moyerman, S., Myers, M., Nishino, H., Paar, H., Peloton, J., Quealy, E., Rebeiz, G., Reichardt, C. L., Richards, P. L., Ross, C., Shimizu, A., Shimmin, C., Shimon, M., Sholl, M., Siritanasak, P., Spieler, H., Stebor, N., Steinbach, B., Stompor, R., Suzuki, A., Tomaru, T., Tucker, C., Yadav, A., and Zahn, O., "The POLARBEAR Cosmic Microwave Background Polarization Experiment," *Journal of Low Temperature Physics* **176**, 726–732 (Sept. 2014).

[54] Ade, P. A. R., Akiba, Y., Anthony, A. E., Arnold, K., Atlas, M., Barron, D., Boettger, D., Borrill, J., Chapman, S., Chinone, Y., Dobbs, M., Elleflot, T., Errard, J., Fabbian, G., Feng, C., Flanigan, D., Gilbert, A., Grainger,

W., Halverson, N. W., Hasegawa, M., Hattori, K., Hazumi, M., Holzapfel, W. L., Hori, Y., Howard, J., Hyland, P., Inoue, Y., Jaehnig, G. C., Jaffe, A., Keating, B., Kermish, Z., Keskitalo, R., Kisner, T., Le Jeune, M., Lee, A. T., Linder, E., Leitch, E. M., Lungu, M., Matsuda, F., Matsumura, T., Meng, X., Miller, N. J., Morii, H., Moyerman, S., Myers, M. J., Navaroli, M., Nishino, H., Paar, H., Peloton, J., Quealy, E., Rebeiz, G., Reichardt, C. L., Richards, P. L., Ross, C., Schanning, I., Schenck, D. E., Sherwin, B., Shimizu, A., Shimmin, C., Shimon, M., Siritanasak, P., Smecher, G., Spieler, H., Stebor, N., Steinbach, B., Stompor, R., Suzuki, A., Takakura, S., Tomaru, T., Wilson, B., Yadav, A., and Zahn, O., "Measurement of the cosmic microwave background polarization lensing power spectrum with the polarbear experiment," *Phys. Rev. Lett.* **113**, 021301 (Jul 2014).

[55] Ade, P. A. R., Akiba, Y., Anthony, A. E., Arnold, K., Atlas, M., Barron, D., Boettger, D., Borrill, J., Borys, C., Chapman, S., Chinone, Y., Dobbs, M., Elleflot, T., Errard, J., Fabbian, G., Feng, C., Flanigan, D., Gilbert, A., Grainger, W., Halverson, N. W., Hasegawa, M., Hattori, K., Hazumi, M., Holzapfel, W. L., Hori, Y., Howard, J., Hyland, P., Inoue, Y., Jaehnig, G. C., Jaffe, A., Keating, B., Kermish, Z., Keskitalo, R., Kisner, T., Le Jeune, M., Lee, A. T., Leitch, E. M., Linder, E., Lungu, M., Matsuda, F., Matsumura, T., Meng, X., Miller, N. J., Morii, H., Moyerman, S., Myers, M. J., Navaroli, M., Nishino, H., Paar, H., Peloton, J., Poletti, D., Quealy, E., Rebeiz, G., Reichardt, C. L., Richards, P. L., Ross, C., Rotermund, K., Schanning, I., Schenck, D. E., Sherwin, B. D., Shimizu, A., Shimmin, C., Shimon, M., Siritanasak, P., Smecher, G., Spieler, H., Stebor, N., Steinbach, B., Stompor, R., Suzuki, A., Takakura, S., Tikhomirov, A., Tomaru, T., Wilson, B., Yadav, A., and Zahn, O., "Evidence for gravitational lensing of the cosmic microwave background polarization from cross-correlation with the cosmic infrared background," *Phys. Rev. Lett.* **112**, 131302 (Apr 2014).

[56] Ade, T. P. C. P. A. R., Akiba, Y., Anthony, A. E., Arnold, K., Atlas, M., Barron, D., Boettger, D., Borrill, J., Chapman, S., Chinone, Y., Dobbs, M., Elleflot, T., Errard, J., Fabbian, G., Feng, C., Flanigan, D., Gilbert, A., Grainger, W., Halverson, N. W., Hasegawa, M., Hattori, K., Hazumi, M., Holzapfel, W. L., Hori, Y., Howard, J., Hyland, P., Inoue, Y., Jaehnig, G. C., Jaffe, A. H., Keating, B., Kermish, Z., Keskitalo, R., Kisner, T., Jeune, M. L., Lee, A. T., Leitch, E. M., Linder, E., Lungu, M., Matsuda, F., Matsumura, T., Meng, X., Miller, N. J., Morii, H., Moyerman, S., Myers, M. J., Navaroli, M., Nishino, H., Orlando, A., Paar, H., Peloton, J., Poletti, D., Quealy, E., Rebeiz, G., Reichardt, C. L., Richards, P. L., Ross, C., Schanning, I., Schenck, D. E., Sherwin, B. D., Shimizu, A., Shimmin, C., Shimon, M., Siritanasak, P., Smecher, G., Spieler, H., Stebor, N., Steinbach, B., Stompor, R., Suzuki, A., Takakura, S., Tomaru, T., Wilson, B., Yadav, A., and Zahn, O., "A measure-

ment of the cosmic microwave background b-mode polarization power spectrum at sub-degree scales with polarbear," *The Astrophysical Journal* **794**(2), 171 (2014).

[57] Seljak, U., "Measuring Polarization in the Cosmic Microwave Background," *ApJ* **482**, 6 (June 1997).

[58] Chiang, H. C., Ade, P. A. R., Barkats, D., Battle, J. O., Bierman, E. M., Bock, J. J., Dowell, C. D., Duband, L., Hivon, E. F., Holzapfel, W. L., Hristov, V. V., Jones, W. C., Keating, B. G., Kovac, J. M., Kuo, C. L., Lange, A. E., Leitch, E. M., Mason, P. V., Matsumura, T., Nguyen, H. T., Ponthieu, N., Pryke, C., Richter, S., Rocha, G., Sheehy, C., Takahashi, Y. D., Tolan, J. E., and Yoon, K. W., "Measurement of cosmic microwave background polarization power spectra from two years of bicep data," *ApJ* **711**(2), 1123 (2010).

[59] Hanson, D., Hoover, S., Crites, A., Ade, P. A. R., Aird, K. A., Austermann, J. E., Beall, J. A., Bender, A. N., Benson, B. A., Bleem, L. E., Bock, J. J., Carlstrom, J. E., Chang, C. L., Chiang, H. C., Cho, H.-M., Conley, A., Crawford, T. M., de Haan, T., Dobbs, M. A., Everett, W., Gallicchio, J., Gao, J., George, E. M., Halverson, N. W., Harrington, N., Henning, J. W., Hilton, G. C., Holder, G. P., Holzapfel, W. L., Hrubes, J. D., Huang, N., Hubmayr, J., Irwin, K. D., Keisler, R., Knox, L., Lee, A. T., Leitch, E., Li, D., Liang, C., Luong-Van, D., Marsden, G., McMahon, J. J., Mehl, J., Meyer, S. S., Mocanu, L., Montroy, T. E., Natoli, T., Nibarger, J. P., Novosad, V., Padin, S., Pryke, C., Reichardt, C. L., Ruhl, J. E., Saliwanchik, B. R., Sayre, J. T., Schaffer, K. K., Schulz, B., Smecher, G., Stark, A. A., Story, K. T., Tucker, C., Vanderlinde, K., Vieira, J. D., Viero, M. P., Wang, G., Yefremenko, V., Zahn, O., and Zemcov, M., "Detection of B-Mode Polarization in the Cosmic Microwave Background with Data from the South Pole Telescope," *Phys. Rev. Lett.* **111**, 141301 (Oct. 2013).

[60] Keisler, R., Hoover, S., Harrington, N., Henning, J. W., Ade, P. A. R., Aird, K. A., Austermann, J. E., Beall, J. A., Bender, A. N., Benson, B. A., Bleem, L. E., Carlstrom, J. E., Chang, C. L., Chiang, H. C., Cho, H., Citron, R., Crawford, T. M., Crites, A. T., de Haan, T., Dobbs, M. A., Everett, W., Gallicchio, J., Gao, J., George, E. M., Gilbert, A., Halverson, N. W., Hanson, D., Hilton, G. C., Holder, G. P., Holzapfel, W. L., Hou, Z., Hrubes, J. D., Huang, N., Hubmayr, J., Irwin, K. D., Knox, L., Lee, A. T., Leitch, E. M., Li, D., Luong-Van, D., Marrone, D. P., McMahon, J. J., Mehl, J., Meyer, S. S., Mocanu, L., Natoli, T., Nibarger, J. P., Novosad, V., Padin, S., Pryke, C., Reichardt, C. L., Ruhl, J. E., Saliwanchik, B. R., Sayre, J. T., Schaffer, K. K., Shirokoff, E., Smecher, G., Stark, A. A., Story, K. T., Tucker, C., Vanderlinde, K., Vieira, J. D., Wang, G., Whitehorn, N., Yefremenko, V., and Zahn, O., "Measurements of Sub-degree B-mode Polarization in the Cosmic Microwave

Background from 100 Square Degrees of SPTpol Data," *ArXiv e-prints* (Mar. 2015).

[61] BICEP2/Keck and Planck Collaborations, Ade, P. A. R., Aghanim, N., Ahmed, Z., Aikin, R. W., Alexander, K. D., Arnaud, M., Aumont, J., Baccigalupi, C., Banday, A. J., and et al., "Joint Analysis of BICEP2/Keck Array and Planck Data," *Physical Review Letters* **114**, 101301 (Mar. 2015).

[62] Myers, M., Arnold, K., Ade, P., Engargiola, G., Holzapfel, W., Lee, A., Meng, X., OâĂŹBrient, R., Richards, P., Spieler, H., and Tran, H., "Antenna-coupled bolometer arrays for measurement ofÂătheÂăcosmic microwave backgroundÂăpolarization," *Journal of Low Temperature Physics* **151**(1-2), 464–470 (2008).

[63] Tran, H., Lee, A., Hanany, S., Milligan, M., and Renbarger, T., "Comparison of the crossed and the gregorian mizuguchi-dragone for wide-field millimeter-wave astronomy," *Appl. Opt.* **47**(2), 103–109 (2008).

[64] Lee, A. T., Tran, H., Ade, P., Arnold, K., Borrill, J., Dobbs, M. A., Errard, J., Halverson, N., Holzapfel, W. L., Howard, J., Jaffe, A., Keating, B., Kermish, Z., Linder, E., Miller, N., Myers, M., Niarchou, A., Paar, H., Reichardt, C., Spieler, H., Steinbach, B., Stompor, R., Tucker, C., Quealy, E., Richards, P. L., and Zahn, O., "POLARBEAR: Ultra-high Energy Physics with Measurements of CMB Polarization," in [*American Institute of Physics Conference Series*], Kodama, H. and Ioka, K., eds., *American Institute of Physics Conference Series* **1040**, 66–77 (Aug. 2008).

[65] Filipovic, D. *IEEE Trans. on Micr. Theory and Tech.* **41**(10) (1993).

[66] Aumont, J., Conversi, L., Thum, C., Wiesemeyer, H., Falgarone, E., Macías-Pérez, J. F., Piacentini, F., Pointecouteau, E., Ponthieu, N., Puget, J. L., Rosset, C., Tauber, J. A., and Tristram, M., "Measurement of the Crab nebula polarization at 90 GHz as a calibrator for CMB experiments," *A&A* **514**, A70 (May 2010).

[67] Smith, K. M., Zahn, O., and Doré, O., "Detection of gravitational lensing in the cosmic microwave background," *Phys. Rev. D* **76**, 043510 (Aug 2007).

[68] Hirata, C. M., Ho, S., Padmanabhan, N., Seljak, U., and Bahcall, N. A., "Correlation of CMB with large-scale structure. II. Weak lensing," *Phys. Rev. D* **78**, 043520 (Aug. 2008).

[69] Feng, C., Aslanyan, G., Manohar, A. V., Keating, B., Paar, H. P., and Zahn, O., "Measuring gravitational lensing of the cosmic microwave background using cross correlation with large scale structure," *Phys. Rev. D* **86**, 063519 (Sep 2012).

[70] Sherwin, B. D., Das, S., Hajian, A., Addison, G., Bond, J. R., Crichton, D., Devlin, M. J., Dunkley, J., Gralla, M. B., Halpern, M., Hill, J. C., Hincks, A. D., Hughes, J. P., Huffenberger, K., Hlozek, R., Kosowsky, A., Louis, T., Marriage, T. A., Marsden, D., Menanteau, F., Moodley, K., Niemack, M. D., Page, L. A., Reese, E. D., Sehgal, N., Sievers, J., Sifón, C., Spergel, D. N., Staggs, S. T., Switzer, E. R., and Wollack, E., "The atacama cosmology telescope: Cross-correlation of cosmic microwave background lensing and quasars," *Phys. Rev. D* **86**, 083006 (Oct 2012).

[71] Holder, G. P., Viero, M. P., Zahn, O., Aird, K. A., Benson, B. A., Bhattacharya, S., Bleem, L. E., Bock, J., Brodwin, M., Carlstrom, J. E., Chang, C. L., Cho, H.-M., Conley, A., Crawford, T. M., Crites, A. T., de Haan, T., Dobbs, M. A., Dudley, J., George, E. M., Halverson, N. W., Holzapfel, W. L., Hoover, S., Hou, Z., Hrubes, J., Keisler, R., Knox, L., Lee, A. T., Leitch, E. M., Lueker, M., Luong-Van, D., Marsden, G., Marrone, D., McMahon, J. J., Mehl, J., Meyer, S. S., Millea, M., Mohr, J. J., Montroy, T. E., Padin, S., Plagge, T., Pryke, C., Reichardt, C. L., Ruhl, J. E., Sayre, J. T., Schaffer, K. K., Schulz, B., Shaw, L., Shirokoff, E., Spieler, H. G., Staniszewski, Z., Stark, A. A., Story, K. T., van Engelen, A., Vanderlinde, K., Vieira, J. D., Williamson, R., and Zemcov, M., "A cosmic microwave background lensing mass map and its correlation with the cosmic infrared background," *The Astrophysical Journal Letters* **771**(1), L16 (2013).

[72] Hazumi, M., Ade, P., Akiba, Y., Anthony, A., Arnold, K., Atlas, M., Barron, D., Bender, A., Boettger, D., Borrill, J., Chapman, S., Chinone, Y., Cukierman, A., Dobbs, M., Elleflot, T., Errard, J., Fabbian, G., Feng, C., Gilbert, A., Goeckner-Wald, N., Halverson, N., Hasegawa, M., Hattori, K., Holzapfel, W., Hori, Y., Inoue, Y., Jaehnig, G., Jaffe, A., Katayama, N., Keating, B., Kermish, Z., Keskitalo, R., Kisner, T., Jeune, M. L., Lee, A., Leitch, E., Linder, E., Matsuda, F., Matsumura, T., Meng, X., Miller, N., Morii, H., Myers, M., Navaroli, M., Nishino, H., Okamura, T., Paar, H., Peloton, J., Poletti, D., Raum, C., Rebeiz, G., Reichardt, C., Richards, P., Ross, C., Rotermund, K., Schenck, D., Sherwin, B., Shirley, I., Sholl, M., Siritanasak, P., Smecher, G., Stebor, N., Steinbach, B., Stompor, R., Suzuki, A., Suzuki, J., Takada, S., Takakura, S., Tomaru, T., Wilson, B., Yadav, A., and Zahn, O., "POLARBEAR-2: a new instrument for CMB polarization measurements with the Simons Array," *Proc. SPIE* **9153**(9153-52) (2014).

[73] Huber, M. E., Neil, P. A., Benson, R. G., Burns, D. A., Corey, A. F., Flynn, C. S., Kitaygorodskaya, Y., Massihzadeh, O., Martinis, J. M., and Hilton, G. C. *IEEE Trans. Appl. .Supercon* **11(2)**(4048) (2001).

[74] Hattori, K., Arnold, K., Barron, D., Dobbs, M., de Haan, T., Harrington, N., Hasegawa, M., Hazumi, M., Holzapfel, W. L., Keating, B., Lee, A. T.,

Morii, H., Myers, M. J., Smecher, G., Suzuki, A., and Tomaru, T., "Adaptation of frequency-domain readout for transition edge sensor bolometers for the polarbear-2 cosmic microwave background experiment," *Nuclear Instruments and Methods in Physics Research Section A: Accelerators, Spectrometers, Detectors and Associated Equipment* **732**(0), 299 – 302 (2013). Vienna Conference on Instrumentation 2013.

[75] Van Sciver, S., "Low-temperature materials properties," in [*Helium Cryogenics*], *International Cryogenics Monograph Series*, 17–58, Springer New York (2012).

[76] Bychkov, Y., Herzog, R., and Khukhareva, I., "Thermal conductivity and electrical resistivity of nbîŮÿti alloys at low temperatures," *Cryogenics* **21**(12), 741 – 745 (1981).

[77] Olson, J., "Thermal conductivity of some common cryostat materials between 0.05 and 2 k," *Cryogenics* **33**(7), 729 – 731 (1993).

[78] Woodcraft, A. L., Ventura, G., Martelli, V., and Holland, W. S., "Thermal conductance at millikelvin temperatures of woven ribbon cable with phosphor-bronze clad superconducting wires," *Cryogenics* **50**(8), 465 – 468 (2010).

[79] Hemachalam, K., King, C., Zeitlin, B., and Scanlan, R., "Fabrication and characterization of fine filaments of nbti in a copper matrix," in [*Advances in Cryogenic Engineering Materials*], Reed, R. and Clark, A., eds., *Advances in Cryogenic Engineering Materials* **32**, 731–738, Springer US (1986).

[80] Ade, P. A. R., Aikin, R. W., Barkats, D., Benton, S. J., Bischoff, C. A., Bock, J. J., Brevik, J. A., Buder, I., Bullock, E., Dowell, C. D., Duband, L., Filippini, J. P., Fliescher, S., Golwala, S. R., Halpern, M., Hasselfield, M., Hildebrandt, S. R., Hilton, G. C., Hristov, V. V., Irwin, K. D., Karkare, K. S., Kaufman, J. P., Keating, B. G., Kernasovskiy, S. A., Kovac, J. M., Kuo, C. L., Leitch, E. M., Lueker, M., Mason, P., Netterfield, C. B., Nguyen, H. T., O'Brient, R., Ogburn, R. W., Orlando, A., Pryke, C., Reintsema, C. D., Richter, S., Schwarz, R., Sheehy, C. D., Staniszewski, Z. K., Sudiwala, R. V., Teply, G. P., Tolan, J. E., Turner, A. D., Vieregg, A. G., Wong, C. L., and Yoon, K. W., "Detection of *b*-mode polarization at degree angular scales by bicep2," *Phys. Rev. Lett.* **112**, 241101 (Jun 2014).

[81] Planck Collaboration, Adam, R., Ade, P. A. R., Aghanim, N., Arnaud, M., Aumont, J., Baccigalupi, C., Banday, A. J., Barreiro, R. B., Bartlett, J. G., and et al., "Planck intermediate results. XXX. The angular power spectrum of polarized dust emission at intermediate and high Galactic latitudes," *ArXiv e-prints* (Sept. 2014).

[82] Naess, S., Hasselfield, M., McMahon, J., Niemack, M. D., Addison, G. E., Ade, P. A. R., Allison, R., Amiri, M., Battaglia, N., Beall, J. A., de Bernardis, F., Bond, J. R., Britton, J., Calabrese, E., Cho, H.-m., Coughlin, K., Crichton, D., Das, S., Datta, R., Devlin, M. J., Dicker, S. R., Dunkley, J., Dünner, R., Fowler, J. W., Fox, A. E., Gallardo, P., Grace, E., Gralla, M., Hajian, A., Halpern, M., Henderson, S., Hill, J. C., Hilton, G. C., Hilton, M., Hincks, A. D., Hlozek, R., Ho, P., Hubmayr, J., Huffenberger, K. M., Hughes, J. P., Infante, L., Irwin, K., Jackson, R., Muya Kasanda, S., Klein, J., Koopman, B., Kosowsky, A., Li, D., Louis, T., Lungu, M., Madhavacheril, M., Marriage, T. A., Maurin, L., Menanteau, F., Moodley, K., Munson, C., Newburgh, L., Nibarger, J., Nolta, M. R., Page, L. A., Pappas, C., Partridge, B., Rojas, F., Schmitt, B. L., Sehgal, N., Sherwin, B. D., Sievers, J., Simon, S., Spergel, D. N., Staggs, S. T., Switzer, E. R., Thornton, R., Trac, H., Tucker, C., Uehara, M., Van Engelen, A., Ward, J. T., and Wollack, E. J., "The Atacama Cosmology Telescope: CMB polarization at 200 l 9000," **10**, 7 (Oct. 2014).

[83] Delabrouille, J., Betoule, M., Melin, J.-B., Miville-Deschênes, M.-A., Gonzalez-Nuevo, J., Le Jeune, M., Castex, G., de Zotti, G., Basak, S., Ashdown, M., Aumont, J., Baccigalupi, C., Banday, A. J., Bernard, J.-P., Bouchet, F. R., Clements, D. L., da Silva, A., Dickinson, C., Dodu, F., Dolag, K., Elsner, F., Fauvet, L., Faÿ, G., Giardino, G., Leach, S., Lesgourgues, J., Liguori, M., Macías-Pérez, J. F., Massardi, M., Matarrese, S., Mazzotta, P., Montier, L., Mottet, S., Paladini, R., Partridge, B., Piffaretti, R., Prezeau, G., Prunet, S., Ricciardi, S., Roman, M., Schaefer, B., and Toffolatti, L., "The pre-launch Planck Sky Model: a model of sky emission at submillimetre to centimetre wavelengths," *A&A* **553**, A96 (May 2013).

[84] Benson, B. A., Ade, P. A. R., Ahmed, Z., Allen, S. W., Arnold, K., Austermann, J. E., Bender, A. N., Bleem, L. E., Carlstrom, J. E., Chang, C. L., Cho, H. M., Cliche, J. F., Crawford, T. M., Cukierman, A., de Haan, T., Dobbs, M. A., Dutcher, D., Everett, W., Gilbert, A., Halverson, N. W., Hanson, D., Harrington, N. L., Hattori, K., Henning, J. W., Hilton, G. C., Holder, G. P., Holzapfel, W. L., Irwin, K. D., Keisler, R., Knox, L., Kubik, D., Kuo, C. L., Lee, A. T., Leitch, E. M., Li, D., McDonald, M., Meyer, S. S., Montgomery, J., Myers, M., Natoli, T., Nguyen, H., Novosad, V., Padin, S., Pan, Z., Pearson, J., Reichardt, C., Ruhl, J. E., Saliwanchik, B. R., Simard, G., Smecher, G., Sayre, J. T., Shirokoff, E., Stark, A. A., Story, K., Suzuki, A., Thompson, K. L., Tucker, C., Vanderlinde, K., Vieira, J. D., Vikhlinin, A., Wang, G., Yefremenko, V., and Yoon, K. W., "SPT-3G: a next-generation cosmic microwave background polarization experiment on the South Pole telescope," in [*Society of Photo-Optical Instrumentation Engineers (SPIE) Conference Series*], *Society of Photo-Optical Instrumentation Engineers (SPIE) Conference Series* **9153**, 1 (July 2014).

[85] Essinger-Hileman, T., Ali, A., Amiri, M., Appel, J. W., Araujo, D., Bennett, C. L., Boone, F., Chan, M., Cho, H.-M., Chuss, D. T., Colazo, F., Crowe, E., Denis, K., Dünner, R., Eimer, J., Gothe, D., Halpern, M., Harrington, K., Hilton, G. C., Hinshaw, G. F., Huang, C., Irwin, K., Jones, G., Karakla, J., Kogut, A. J., Larson, D., Limon, M., Lowry, L., Marriage, T., Mehrle, N., Miller, A. D., Miller, N., Moseley, S. H., Novak, G., Reintsema, C., Rostem, K., Stevenson, T., Towner, D., U-Yen, K., Wagner, E., Watts, D., Wollack, E. J., Xu, Z., and Zeng, L., "CLASS: the cosmology large angular scale surveyor," in [*Society of Photo-Optical Instrumentation Engineers (SPIE) Conference Series*], *Society of Photo-Optical Instrumentation Engineers (SPIE) Conference Series* **9153**, 1 (July 2014).

[86] Abazajian, K. N., Arnold, K., Austermann, J., Benson, B. A., Bischoff, C., Bock, J., Bond, J. R., Borrill, J., Calabrese, E., Carlstrom, J. E., Carvalho, C. S., Chang, C. L., Chiang, H. C., Church, S., Cooray, A., Crawford, T. M., Dawson, K. S., Das, S., Devlin, M. J., Dobbs, M., Dodelson, S., Dore, O., Dunkley, J., Errard, J., Fraisse, A., Gallicchio, J., Halverson, N. W., Hanany, S., Hildebrandt, S. R., Hincks, A., Hlozek, R., Holder, G., Holzapfel, W. L., Honscheid, K., Hu, W., Hubmayr, J., Irwin, K., Jones, W. C., Kamionkowski, M., Keating, B., Keisler, R., Knox, L., Komatsu, E., Kovac, J., Kuo, C.-L., Lawrence, C., Lee, A. T., Leitch, E., Linder, E., Lubin, P., McMahon, J., Miller, A., Newburgh, L., Niemack, M. D., Nguyen, H., Nguyen, H. T., Page, L., Pryke, C., Reichardt, C. L., Ruhl, J. E., Sehgal, N., Seljak, U., Sievers, J., Silverstein, E., Slosar, A., Smith, K. M., Spergel, D., Staggs, S. T., Stark, A., Stompor, R., Vieregg, A. G., Wang, G., Watson, S., Wollack, E. J., Wu, W. L. K., Yoon, K. W., and Zahn, O., "Neutrino Physics from the Cosmic Microwave Background and Large Scale Structure," *ArXiv e-prints* (Sept. 2013).

[87] Abazajian, K. N., Arnold, K., Austermann, J., Benson, B. A., Bischoff, C., Bock, J., Bond, J. R., Borrill, J., Buder, I., Burke, D. L., Calabrese, E., Carlstrom, J. E., Carvalho, C. S., Chang, C. L., Chiang, H. C., Church, S., Cooray, A., Crawford, T. M., Crill, B. P., Dawson, K. S., Das, S., Devlin, M. J., Dobbs, M., Dodelson, S., Doré, O., Dunkley, J., Feng, J. L., Fraisse, A., Gallicchio, J., Giddings, S. B., Green, D., Halverson, N. W., Hanany, S., Hanson, D., Hildebrandt, S. R., Hincks, A., Hlozek, R., Holder, G., Holzapfel, W. L., Honscheid, K., Horowitz, G., Hu, W., Hubmayr, J., Irwin, K., Jackson, M., Jones, W. C., Kallosh, R., Kamionkowski, M., Keating, B., Keisler, R., Kinney, W., Knox, L., Komatsu, E., Kovac, J., Kuo, C.-L., Kusaka, A., Lawrence, C., Lee, A. T., Leitch, E., Linde, A., Linder, E., Lubin, P., Maldacena, J., Martinec, E., McMahon, J., Miller, A., Mukhanov, V., Newburgh, L., Niemack, M. D., Nguyen, H., Nguyen, H. T., Page, L., Pryke, C., Reichardt, C. L., Ruhl, J. E., Sehgal, N., Seljak, U., Senatore, L., Sievers, J.,

Silverstein, E., Slosar, A., Smith, K. M., Spergel, D., Staggs, S. T., Stark, A., Stompor, R., Vieregg, A. G., Wang, G., Watson, S., Wollack, E. J., Wu, W. L. K., Yoon, K. W., Zahn, O., and Zaldarriaga, M., "Inflation Physics from the Cosmic Microwave Background and Large Scale Structure," *ArXiv e-prints* (Sept. 2013).

[88] Chluba, J., "Science with CMB spectral distortions," *ArXiv e-prints* (May 2014).